Chem Soc Rev

RSC Publishing

REVIEW ARTICLE

View Article Online
View Journal | View Issue

Published on 30 April 2013. Downloaded by University of Tennessee at Knoxville on 10/06/2016 20:55:54.

Cite this: *Chem. Soc. Rev.*, 2013, **42**, 5907

An overview of the magnetoresistance phenomenon in molecular systems

Hongbo Gu,[ab] Xi Zhang,[ac] Huige Wei,[a] Yudong Huang,[b] Suying Wei*[d] and Zhanhu Guo*[a]

Received 23rd February 2013

DOI: 10.1039/c3cs60074b

www.rsc.org/csr

In this review, the classification of magnetoresistance effects, the electrical conduction mechanisms without and with magnetic field, and the spintronics are briefly summarized. The magnetoresistance effect in the molecular systems including small organic molecules, carbon nanotubes, graphene, conductive polymers and their nanocomposites is critically reviewed. The four normally used models are elaborated to disclose the mechanisms of organic magnetoresistance (OMAR) in the organic systems. The most current applications of these molecular systems are also summarized. These molecular systems are envisioned to create next-generation spintronic and electronic devices for flexible applications.

1. Introduction

Magnetoresistance (MR) is a phenomenon that reflects the resistance change of a material when an external magnetic field is applied to it.[1,2] Generally, the MR effect can be categorized into five distinct types including ordinary magnetoresistance (OMR), anisotropic magnetoresistance (AMR), giant magnetoresistance (GMR), tunneling magnetoresistance (TMR) and colossal magnetoresistance (CMR). Recently in the literature, it was reported that the MR effect can also be observed in the carbon nanostructural materials (such as carbon nanotubes and graphene),[3–5] organic molecules,[6,7] conjugated polymers and their nanocomposites,[8,9] and nanoparticles in the insulating polymers.[10] The MR effect observed in the organic materials without any magnetic materials is called organic magnetoresistance (OMAR).[11–14]

[a] *Integrated Composites Lab (ICL), Dan F. Smith Department of Chemical Engineering, Lamar University, Beaumont, TX 77710, USA. E-mail: zhanhu.guo@lamar.edu; Fax: +1 409-880-2197; Tel: +1 409-880-7654*
[b] *School of Chemical Engineering and Technology, Harbin Institute of Technology, Harbin 150001, Heilongjiang, China*
[c] *Department of Chemistry and Physics, Lamar University, Beaumont, TX 77710, USA*
[d] *Department of Chemistry and Biochemistry, Lamar University, Beaumont, TX 77710, USA. E-mail: suying.wei@lamar.edu; Fax: +1 409-880-8270; Tel: +1 409-880-7976*

Hongbo Gu

Hongbo Gu is currently a joint Chemical Engineering PhD student at Harbin Institute of Technology and Lamar University, sponsored by China Scholarship Council (CSC). Miss Gu obtained a BS degree in Polymer Science and Technology at Harbin Institute of Technology (2008). She was selected to receive a Student Participation Fellowship from the 2012 NSF-CMMI Research and Innovation Conference. Her research interests focus on the Giant Magnetoresistance (GMR) sensors and multifunctional polymer nanocomposites especially for the magnetic and conductive materials.

Xi Zhang

Xi Zhang, currently a PhD student in Dan F. Smith Department of Chemical Engineering at Lamar University, obtained a master's degree from Department of Mechanical and Automotive Engineering, South China University of Technology (2010) and a BS degree in Polymer Science and Technology from South China University of Technology (2006). Her research interests include polymer nanocomposites, especially the conductive nanocomposites.

Published on 30 April 2013. Downloaded by University of Tennessee at Knoxville on 10/06/2016 20:55:54.

The interest in the MR effect is growing due to its wide range of applications in the magnetic recording system over the last few decades.[15–17] Especially, the MR effect has made a great impact on the computer memory and storage technology.[18] From the first used magnetic core memory in the mid-1950s up to now, the magnetic memory in computers has improved more than five orders of magnitude in density.[19,20] Meanwhile, the magnetoresistance-based sensor systems have also shown the promising platform technology for the biosensing and biochip systems.[21–24] Moreover, a new technology ''spintronics'', which is also called spin electronics[25] or magnetoelectronics,[26–28] has emerged in the last few years, which is a condensed-matter physics area focused on the investigation of properties of electron spin to improve the efficiency of the electronic devices and to enrich them with new functionalities.[29] More recently, since the Nobel Prize in Physics was awarded to Drs Fert and Grunberg in 2007 for their discovery of the GMR phenomenon,[30,31] it has attracted more attention to seek new technologies and materials. However, there are still many challenges in this field. For example, can the structural design make the MR devices more sensitive and store more information by an applied external magnetic field? What kind of structural materials can be potentially used for MR sensors? Can the emerged organic spintronics replace the traditional semiconductors? Is the MR signal strong enough for the organic materials to be used in the MR devices? The understanding of the electrical transport mechanism and the MR phenomenon in different materials is extremely important for the new structural MR materials design.

Though there are several comprehensive reviews on the metallic MR phenomena,[32–37] in which most of the reported results have been summarized, reviews focusing on the molecular systems, especially on the conjugated polymers and their nanocomposites,

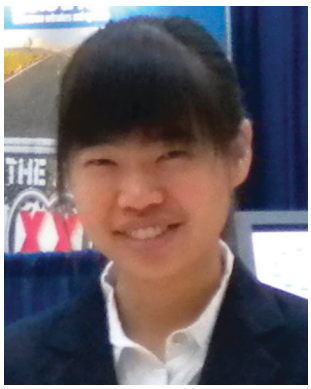

Huige Wei

Miss Huige Wei, currently a candidate PhD student in Dan F. Smith Department of Chemical Engineering at Lamar University, obtained MS (2011) and BE (2009) degrees from the Department of Chemical Engineering and Technology at Harbin Institute of Technology, Harbin, China. Her research interests focus on multifunctional polymer nanocomposites for electrochromic and energy storage applications.

Yudong Huang

Dr Yudong Huang, currently a Professor and Dean of School of Chemical Engineering and Technology at Harbin Institute of Technology in China, obtained a PhD degree in Composite Materials from Harbin Institute of Technology (1993) and a BS in Polymer Material Engineering from Harbin Institute of Technology (1988). His research focuses on the fiber reinforced polymer composites and surface treatment of fibers, and fabrication of high performance organic fibers.

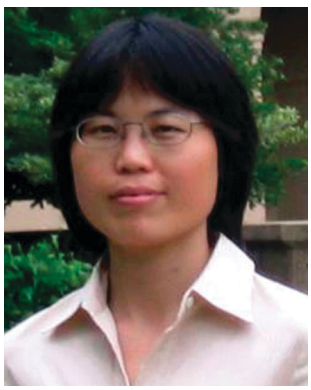

Suying Wei

Dr Suying Wei, currently an Assistant Professor in the Department of Chemistry and Biochemistry at Lamar University, obtained a PhD degree in chemistry from Louisiana State University (2006), an MS in applied chemistry from Beijing University of Chemical Technology (2000) and a BS in chemical engineering from Shandong University of Science and Technology (1996). Her research interests include multifunctional composites especially those used in biomedical applications. Her expertise is in analytical, materials and surface chemistry. She was awarded the NSF summer institute fellowship, the Pfizer graduate fellowship and the Robinson award for excellent research in analytical science during previous professional development.

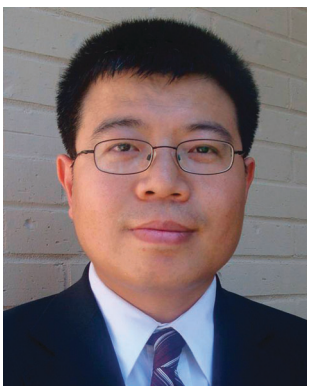

Zhanhu Guo

Dr Zhanhu Guo, currently an Assistant Professor in Dan F. Smith Department of Chemical Engineering at Lamar University, obtained a PhD degree in Chemical Engineering from Louisiana State University (2005) and received three-year (2005–2008) postdoctoral training in Mechanical and Aerospace Engineering Department at University of California Los Angeles. Dr Guo directs the Integrated Composites Laboratory and chairs the Composite Division of American Institute of Chemical Engineers (AIChE, 2010–2011). His current research focuses on fundamental science behind multifunctional light-weight nanocomposites especially with polymer and carbon as the hosting matrix for electronic devices and environmental remediation applications.

This journal is © The Royal Society of Chemistry 2013

Published on 30 April 2013. Downloaded by University of Tennessee at Knoxville on 10/06/2016 20:55:54.

have been rarely reported. In this review, the major focus is on classifications of the MR effects, electrical conduction mechanisms in the materials without and with magnetic field, and the specific MR applications in spintronics. Due to limited space, only the MR effects in the molecular systems such as small organic molecules including tris(8-hydroxyquinolinato)aluminum (Alq_3) and rubrene, graphene, carbon nanotubes, conductive polymers and polymer nanocomposites are critically reviewed. The mechanisms of OMAR effects with the four typically adopted models in these systems are discussed. The potential applications of these molecular systems have been described as well as the perspectives in the fields.

2. Classifications of magnetoresistance

2.1 Ordinary magnetoresistance (OMR)

The ordinary magnetoresistance (OMR) is often found in the non-magnetic metals and is due to the electrons deviating from the electric field direction by the Lorentz force, which increases the resistivity with increasing magnetic field.[38,39] The OMR effect is very small in low fields, although the effect could become much larger in high fields.[40] In the classical OMR theory, OMR is always positive and proportional to the quadratic magnetic field when the multiplication of the cyclotron frequency (ω_c, the frequency of an electron moving perpendicular to the direction of a magnetic field H with a constant magnitude and direction; $\omega_c = eH/2\pi m_e$, where e is the electron charge and m_e is the mass of an electron) and the relaxation time τ of the materials is smaller than that in small magnetic fields , *i.e.* $\omega_c\tau \ll 1$, or for the stoichiometric semiconductors, where the concentration of electrons n equals to that of the holes p. OMR is expressed as eqn (1) and (2):[41]

$$\mathrm{MR} \propto H^2 \ (\omega_c\tau \ll 1) \quad (1)$$

$$\mathrm{MR} \propto \mathrm{const} \ (\omega_c\tau \gg 1), n \neq p \quad (2)$$

Generally, the OMR is strongly dependent on the measured temperatures and becomes larger at lower temperature due to the decreased thermal phonon scattering.[42] Recently, the OMR effect has been observed in the three-dimensional nanoporous gold (Au),[42] single crystalline bismuth (Bi) nanowires fabricated using the stress-induced method[43] and electrodeposition,[44] and α-Mn thin film (α phase Mn is stable at room temperature, and it has a body-centered-cubic (bcc) structure).[45] Interestingly, Cimpoiasu *et al.*[46] have investigated the H dependent OMR behavior of the mechanically stretched bulk sheets of carbon nanotubes (CNTs), and showed that the OMR was also related to the stretching direction and the direction of the applied H (they called it ''angular magnetoresistance'').

2.2 Anisotropic magnetoresistance (AMR)

The first anisotropic magnetoresistance (AMR) in ferromagnetic (FM) Ni and Fe metals was reported by William Thomson in 1856.[47] The AMR effect is defined as the difference between $\rho_\parallel$ (the resistivity when the magnetic moment M is parallel to the electrical current $\hat{\imath}$) and $\rho_\perp$ (the resistivity when M is transverse to $\hat{\imath}$), which is expressed as $\Delta\rho = \rho_\parallel - \rho_\perp$.[48] The normalized $\Delta\rho/\rho_{av}$ is called AMR, where $\rho_{av} \equiv (1/3)\rho_\parallel + (2/3)\rho_\perp$.[48] Owing to the AMR effect, the electric field is given using a vector form in eqn (3):[48]

$$E = \rho_\perp j + \alpha(j\cdot\alpha)(\rho_\parallel - \rho_\perp) + \rho_H\alpha \times j \quad (3)$$

where α is the unit vector in the direction of magnetic moment M of the single domain sample and j is the current density. From eqn (3), an angle θ between M and j is introduced and described in eqn (4):

$$\rho(\theta) = \rho_\perp \sin^2\theta + \rho_\parallel \cos^2\theta \ \text{ or } \ \rho(\theta) = \rho_\perp + \Delta\rho\cos^2\theta \quad (4)$$

$\cos\theta$ is the average over a large number of randomly oriented crystallites.[49]

The AMR effect is often observed in a number of thin films of FM metals and alloys of Fe, Co and Ni.[50,51] At room temperature, the anisotropic resistance in alloys of Ni–Fe and Ni–Co can be greater than 5%.[48] It depends on the orientation of magnetic moments with respect to the direction of electric current, arising from the spin–orbit coupling and d band splitting.[52] The schematic of the AMR effect is demonstrated in Fig. 1. If M (magnetic moment) is oriented transverse to i and the spin–orbits are parallel to i, a small cross-section for scattering resulted, causing a low resistance state, Fig. 1(a); if M is parallel to i and the spin–orbits are orientated perpendicular to i, a large cross-section for scattering is attained, leading to a high resistance state, Fig. 1(b).

Later on, the AMR effect in the epitaxial Fe (110) films,[49] two-dimensional holes of GaAs,[53] (Ga, Mn)As films,[54] single Ni and Co nanowires,[55] and single-crystal $HoNi_2B_2C$ has been reported.[56] Recently, the AMR effect was observed to be enhanced by using Al_2O_3 encapsulation[57] and in nanometer-scale FM contacts at low temperature.[58] This AMR effect has been used in current transducers and sensors to measure the Earth's magnetic field (electronic compass), AMR-magnetic random access memory (MRAM) devices[59] and a magnetic field detector for digital recording and magnetic bubbles.[48]

2.3 Giant magnetoresistance (GMR)

GMR is a quantum mechanical effect, which was first observed in a multilayered thin-film structural material composed of a couple of FM Fe layers separated by a non-magnetic Cr layer in 1988.[30] GMR was defined as the ratio of $(R_{AP} - R_P)/R_P$, where R_P and R_{AP} are the resistances of the materials for parallel and antiparallel alignments of two magnetic electrodes,[60] depending on the magnetization state of the materials under an applied

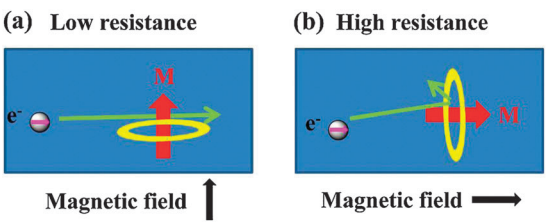

Fig. 1 Schematic of the AMR effect: (a) M is transverse to i and (b) M is parallel to i.

Published on 30 April 2013. Downloaded by University of Tennessee at Knoxville on 10/06/2016 20:55:54.

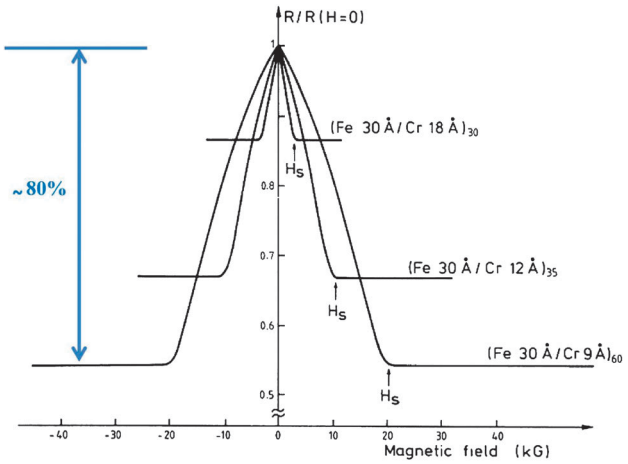

Fig. 2 GMR effect observed in the multilayers of Fe–Cr superlattices. Reprinted with permission from the American Physical Society.[30]

magnetic field. In these antiferromagnetically coupled multilayers of Fe–Cr superlattices, a GMR value of up to 80% was observed at 4.2 K and decreased with increasing thickness of Cr layers, Fig. 2.[30] This effect was subsequently reported in many other multilayered structures, consisting of FM and antiferromagnetic (AFM) or non-magnetic metals.[61–65]

The GMR effect has also been observed in the granular system containing small magnetic entities dispersed in the paramagnetic or non-magnetic matrix such as Co in Cu or Fe in Ag,[17,66–70] carbon based systems (such as carbon nanotubes and graphene), organic materials,[14,71,72] and spin-valve sandwich structures.[73] The spin-valve is a GMR based device. These structural materials consist of two FM layers (alloys of Fe, Co and Ni) separated by a non-magnetic metal (Cu, Ag and Au), Fig. 3.[32] In these structures, one of the two FM layers is called the "pinned layer", in which the magnetization is relatively insensitive to the moderate magnetic field.[74] The other FM layer is called the "free layer", in which the magnetization could be changed by applying a relatively small magnetic field. The MR of the spin-valve structure is obtained by changing the magnetization of two FM layers from parallel to antiparallel.[32] The pinned magnetic layer is often connected to an AFM layer and the interface between these two layers could help to resist the changes due to the magnetization of the pinned FM layer.[32] Since the magnetization of the pinned layer pins along one orientation, the rotation of the free layer magnetization "opens" (in parallel configuration) or "closes" (in antiparallel configuration) the flow of electrons, behaving as a sort of valve, which is the origin of the spin-valve device.[75]

The GMR effect is used to change the relative orientation of magnetization in adjacent magnetic metal layers and the thickness of the films must be less than the mean free path of electrons. In the metallic multilayer GMR systems, the electrical transport properties are based on three parameters: (1) the spin-dependent scattering within the layers, (2) the spin-dependent scattering at the interface between the layers, and (3) the resistivity that depends on the magnetization orientation in the magnetic layers.[76,77] Generally, the commonly used transition FM metals are Fe, Co and Ni since the 3d bands of these metals are split by the exchange energy (approximate 1–2 eV), giving two markedly different bands, *i.e.*, spin-up (with a spin parallel to the magnetization) and spin-down (with a spin antiparallel to the magnetization) electrons at the Fermi level.[31,78,79] The electrons in a magnetic material can give different resistances and mean free paths due to the difference in density of states at the Fermi level ($N(E_F)$) of these two spins, which leads to different scattering rates when an external magnetic field is applied.[78] The $N(E_F)$ often makes the spin-up (majority spin) and spin-down (minority spin) electrons nearly identical in the normal metals, however, in the FM metals, the shift of $N(E_F)$ results in the unequal filling of bands, which is the source of the net magnetic moment for the materials and causes different properties of spin-up and spin-down electrons such as number, character and mobility, Fig. 4.[26] The difference in the electrical conductivity between the spin-up and spin-down electrons causes a spin-polarized electric current[32] (spin polarization means nonequilibrium spin population[80]). Particularly, it has been estimated that the mean free path of the spin-up electrons may be five times longer than that of the spin-down ones. Typically, the spin-up electrons have the lower scattering rate[81,82] than the spin-down ones.[83] When the magnetic layers are aligned parallel, the current is mostly carried by spin-up electrons,[84] which can easily pass through the entire material and experience a weak scattering process, leading to a lower resistance state.[75,84,85] However, when the magnetic layers are anti-parallel, both spin-up and spin-down electrons scatter stronger at different parts of the materials and the probability of

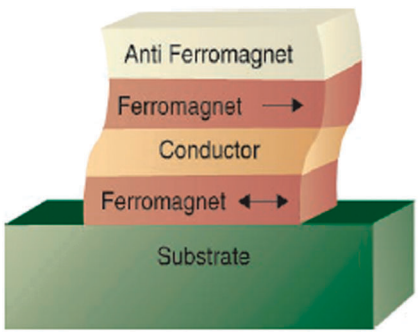

Fig. 3 Spin valve structure. Reprinted with permission from the American Association for the Advancement of Science (AAAS).[32]

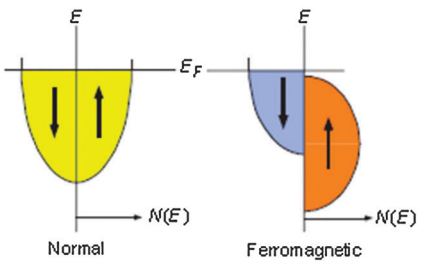

Fig. 4 Schematic diagrams of the density of states in the normal metal and the FM metal (in which the majority spin states (spin-up electrons) are completely filled). E, electron energy; E_F, energy at the Fermi level and $N(E_F)$, density of states at the Fermi level. Reprinted with permission from the American Association for the Advancement of Science (AAAS).[26]

This journal is © The Royal Society of Chemistry 2013

Published on 30 April 2013. Downloaded by University of Tennessee at Knoxville on 10/06/2016 20:55:54.

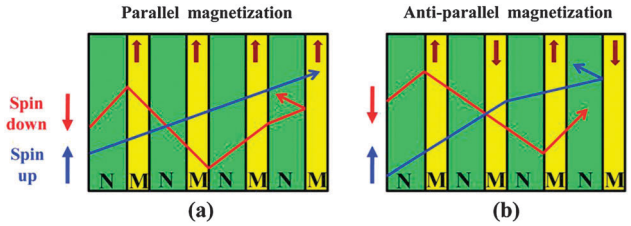

Fig. 5 Spin-dependent scattering of conduction electrons in a multilayer GMR material with (a) parallel (low resistance) and (b) anti-parallel magnetization (high resistance), N represents non-magnetic layers and M represents magnetic layers.[59,87]

scattering is equal for both classes of electrons, leading to an overall higher resistance.[75,86] The heuristic model regarding the spin-dependent scattering of conduction electrons (polarized electric current[79]) in a metallic multilayer GMR system with a parallel and anti-parallel magnetization introduced by White[59,87] is shown in Fig. 5. In the granular metallic system, the electron transport properties are confirmed to be dominated by the interfacial spin-dependent scattering for the GMR effect.[88]

Since its first discovery, the GMR materials have been widely used in many areas[15,89] including rotation speed sensing in automotive systems,[90] angular position sensing,[91] magnetic recording and writing heads (hard disc drivers),[92,93] magnetocardiography sensors,[94] drug delivery,[95] biosensors[96–98] and biochips[99–101] for biological detection,[21,102–104] commercial off the shelf (COTS) for aerospace missions,[105] magnetic field sensors[90,106–110] and MRAM.[91,111]

2.4 Tunneling magnetoresistance (TMR)

The tunneling magnetoresistance (TMR) normally takes place in a magnetic tunnel junction (MTJ), which is composed of two ferromagnets (electrodes) separated by a thin insulating layer (a tunnel barrier) and the resistance is different for the parallel and antiparallel magnetic configurations of these two electrodes.[18] The electrons travel from one FM layer to another FM layer by the tunnel effect, a process in which the spin has been conserved, Fig. 6.[75] In this tunneling process, the electrons find the free states to tunnel under the parallel magnetization (top of Fig. 6) more easily than under the antiparallel magnetization (bottom of Fig. 6) when the electron states on each side of the barrier are spin-polarized.[75] The TMR effect is also defined as $(R_{AP} - R_P)/R_P$, where R_P and R_{AP} are the resistance in the parallel and antiparallel states, respectively. The TMR effect was first demonstrated in the tunneling between two FM films (Fe–Ge–Co tunnel junction system) by Julliere in 1975.[112] A TMR value of around 14% was obtained at low voltage and 4.2 K. Later, a room temperature TMR value of 18% was obtained in the Fe–Al_2O_3–Fe junction system[113] and of 11.8% was obtained in the CoFe–Al_2O_3–Co thin film tunnel junction system,[114] which is great progress in the development of the room temperature TMR effect. The TMR effect was also observed in the Fe–MgO–Fe (which is up to ~220% at room temperature),[60,115,116] Fe–MgO–FeCo(001) single-crystal epitaxial junctions,[117] Co–MgO–Co,[118] CoFeB–MgO–CoFeB

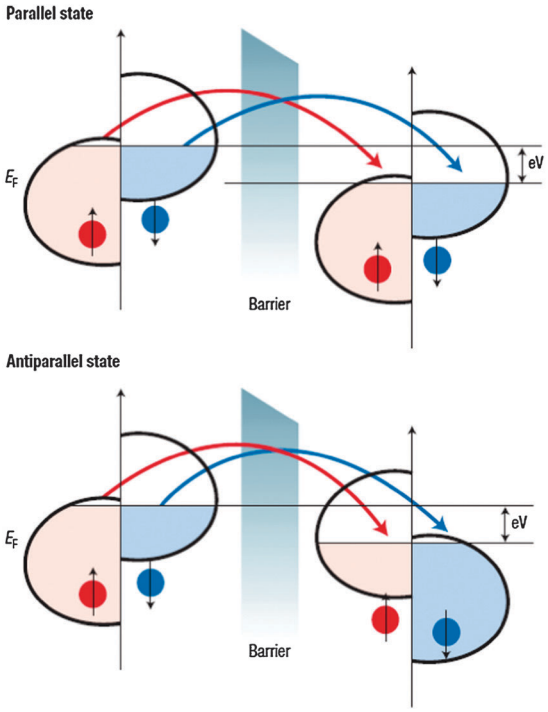

Fig. 6 Schematic of magnetization in the TMR effect related to the $N(E_F)$. Reprinted with permission from the Nature Publishing Group.[75]

(which is 604% at room temperature),[119] carbon nanotube based MTJ systems[120] and organic semiconductor barrier MTJ systems.[121–123]

The TMR effect depends on the magnetization orientation and is related to the spin polarization of tunneling electrons across the insulating barriers,[124] which is determined by the spin dependent $N(E_F)$ of each of the FM electrodes.[112,116,125] Julliere proposed a phenomenological model, in which the TMR arised from the spin dependent electron tunneling.[112] In the MTJ systems, there are two FM electrodes, which are indexed as electrode 1 and electrode 2. The spin polarization P_α (α is 1 or 2) of these two FM electrodes can be calculated from the spin dependent $N(E_F)$ by eqn (5):[112,125,126]

$$P_\alpha = \frac{N_{\alpha\uparrow}(E_F) - N_{\alpha\downarrow}(E_F)}{N_{\alpha\uparrow}(E_F) + N_{\alpha\downarrow}(E_F)} \quad (5)$$

where $N_{\alpha\uparrow}(E_F)$ and $N_{\alpha\downarrow}(E_F)$ are the $N(E_F)$ of the electrode for spin up (majority-spin) and spin down (minority-spin) bands. Thus, TMR could be expressed as eqn (6):[112,125]

$$\mathrm{TMR} = \frac{2P_1P_2}{1 - P_1P_2} \quad (6)$$

The limitation of the TMR is defined by the electrode material used; normally the electrode is a FM metal. However, when the electrode is a non-magnetic metal, $P = 0$; when the $N(E_F)$ of the electrodes is 100% spin-polarized, $|P| = 1$. The spin polarization of a FM material at low temperature could be measured directly using ferromagnet–Al–O–superconductor tunneling junctions.[124] The measured spin polarization of 3d FM metal and alloys based on the Fe, Co and Ni is always

Published on 30 April 2013. Downloaded by University of Tennessee at Knoxville on 10/06/2016 20:55:54.

positive and usually within the range 0–0.6 at low temperature below 4.2 K.[127] The TMR value estimated from eqn (6) agreed well with what was observed experimentally in MTJs.[125] The TMR effect was reviewed by Yuasa and Djayaprawira.[125] To obtain a significant high TMR value, the electrode material should use special materials, called ''half-metallic'' ferromagnets including CrO_2,[128] Fe_3O_4,[129] lanthanum strontium manganite ($La_{0.67}Sr_{0.33}MnO_3$, LSMO).[130] Half-metallic ferromagnets were first introduced by Groot *et al.*[131] In these materials, with the coexistence of metallic nature for one electron spin and insulating nature for the other, the $N(E_F)$ is completely polarized and the conductivity is dominated by the metallic electron spin charge carriers,[132] in other words, 100% spin polarized.[133] Therefore, according to eqn (6), these half-metallic ferromagnets give $|P| = 1$, which means that the TMR value will be up to infinity.

The TMR effect could be used in the programmable logic devices,[134,135] magnetic sensors, read heads of hard disc drives[136] and promising high-performance solid-state MRAM technology, in which the MTJ serves as both storage devices and storage sensing devices.[18,116,137]

2.5 Colossal magnetoresistance (CMR)

The colossal magnetoresistance (CMR) is an extremely large resistivity change by orders of magnitude in the manganite perovskites $T_{1-x}D_xMnO_3$ (where T is a trivalent lanthanide (La) cation, D is a divalent cation like Ca, Sr or Ba)[138] by applying an external magnetic field.[139,140] However, for $LaMnO_3$ and $CaMnO_3$ ($SrMnO_3$ or $BaMnO_3$), the ground state is AFM and the spin interaction is through the superexchange interaction when the metal–oxygen–metal bond angle is close to 180°.[138] However, after being doped with a donor (acceptor) impurity at sufficient doping degrees (such as $x \approx 0.2$–0.4), the donor electrons become delocalized and the materials become highly conductive.[141] The ground state will become FM following the paramagnetic-to-FM transition. In the 1990s, Helmolt *et al.*[142] and Jin *et al.*[143] made great progress in the CMR effect. Helmolt *et al.*[142] observed a more than 60% of CMR in thin magnetic films of $La_{0.67}Ca_{0.33}MnO_3$ and Jin *et al.*[143] obtained 127 000% CMR value at around 77 K and 1300% CMR value at room temperature in the epitaxial films of $La_{0.67}Ca_{0.33}MnO_3$. Since then, lots of research have started focusing on the CMR behaviors of the doped manganite perovskite structure materials.[144–148] The resistivity of the epitaxial films of $La_{0.67}Ca_{0.33}MnO_3$ grown on $LaAlO_3$ substrates using laser ablation and suitable heat treatment underwent a low temperature transition from insulating to metallic and the CMR effect was observed in the metallic regime.

The mechanism of CMR is still not well understood. However, some researchers believed that the observed CMR is associated with the interplay between electron–phonon coupling[149] and FM-to-paramagnetic phase transition.[150] Actually, the pure AFM behavior could only be observed in $LaMnO_3$ and $CaMnO_3$ ($SrMnO_3$ or $BaMnO_3$). Nonetheless, the doping process caused the electron spins in the materials and induced both the ferromagnetism and conduction. The conduction occurs by the hopping through the interchange of valence states of two different valent Mn ions from $Mn^{3+}Mn^{4+}$ to $Mn^{4+}Mn^{3+}$.[151] The application of the magnetic field is likely to increase the alignment of the electron spins and conductivity. The fluctuating spin configuration and electron–electron interaction induced localization have also been considered to produce the CMR effect.[151] Recently, the CMR has also been reported in the ZnO–$La_{0.7}Sr_{0.3}MnO_3$ heterostructure,[152] polycrystalline La_2CoMnO_6,[153] ultraclean and high density two-dimensional GaAs quantum well system,[154] $Nd_{2/3}Sr_{1/3}MnO_3$ ultrathin films grown on charge-ordered $Nd_{1/2}Ca_{1/2}MnO_3$ manganite[155] and sodium chromium oxide with a mixed-valence state ($NaCr_2O_4$).[156] The CMR effect renders these materials potential applications in the magnetic recording[150] and magnetic devices.[157]

2.6 Organic magnetoresistance (OMAR)

Even though the GMR effect was first observed in the metallic multilayers, achieving coherent spin transport (how spins move in metals and semiconductors) over distances at the nanometer scale has proved to be difficult in the normal metals or semiconductors.[158] This challenge has invoked the development of new materials, in which both efficient spin injection (which utilizes the strong, short-range quantum mechanical exchange interaction of the injected spin polarized electrons from the atoms in the FM layers) and transport could be achieved. Therefore, the carbon based materials (such as carbon nanotubes and graphene) and organic semiconductors (OSCs),[6] as a class of promising electronic materials, have attracted considerable attention over the last few decades[4,72,159–162] and have shown applications in large area electronics, flexible, transparent and low-cost electronics[163–165] due to their light-weight, easy processing, low-cost substrates, chemical stability and biocompatible capability[166–168] compared to traditional metal matrix composites in the last decade. Recently, they have also been considered by physical and chemical scientists as new spin transport materials[72,169–172] since elemental carbon has weak spin–orbit coupling (the strength of the spin–orbit interaction is proportional to Z^4, Z is the atomic number of the element[173]) and hyperfine interaction, which permit long spin relaxation lifetime (which is also called longitudinal or spin-lattice time.[80] The range of this time is from 10^{-6} to 10^{-3} s,[174,175] which is several orders of magnitude longer than that in most inorganic materials (10^{-9}–10^{-12} s)[176]). Carbon-based materials and OSCs are very promising platforms for spin electronic devices.[177] Especially, the π-conjugated OSCs are a class of electronic materials that have attracted intensive attention owing to the processing and performance advantages over the conventional brittle semiconductors and their easy usage as spin transport layers between two FM electrodes.[178,179] The π-conjugated OSCs are categorized into two types depending on their molecular weights, *i.e.*, small molecules and polymers. The π-electrons are delocalized in their π-conjugated chemical structures with a relatively small energy gap ranging from about 1.5 to 3.5 eV[178] (for example, rubrene with ~2.3 eV and Alq_3 with ~2.8 eV[180]) between the completely filled valence band

 This journal is © The Royal Society of Chemistry 2013

Published on 30 April 2013. Downloaded by University of Tennessee at Knoxville on 10/06/2016 20:55:54.

(the highest occupied molecular orbital, or HOMO) and the empty conduction band (the lowest unoccupied molecular orbital, LUMO) levels, which leads to their semiconducting properties. Numerous studies on the GMR effect have been reported using OSCs such as Alq_3,[181–184] rubrene,[185] conductive polymers[186,187] and polymer nanocomposites (PNCs).[8] The GMR is realized to be very complicated in these systems since the resistance depends on the parameters including orientation of the magnetic field,[188] layers,[189] temperature,[190,191] frequency,[192] particle size,[187] and composition concentration.[193] The TMR effect has also been reported in the OSCs.[121,174,194–196]

Generally, the OMAR effect in OSCs could be achieved using two approaches. One is to inject spins from FM electrodes (spin-polarized) into the OSCs, such as organic spin-valve structure, in which the organic spacer is used to replace the nonmagnetic spacer. This has been the common structure of the OMAR device so far. Obviously, the performance of these devices depends on the properties of the organic spacer and FM electrodes as well as the properties of the interface between them.[176] The other is to apply a magnetic field directly to the OSCs. In this method, there is no FM electrode being used. This method is under development right now. Francis *et al.*[197] used poly(9,9-dioctylfluorenyl-2,7-diyl) (PFO) organic thin film as the spacer sandwiched between the top contact (either Al, Ca (covered by a capping layer of Al), or Au) and the bottom electrode (consisting of indium-tin-oxide (ITO) covered glass, poly(3,4-ethylenedioxythiophene)/poly(styrenesulfonate) (PEDOT/PSS) spin-coated on top of ITO, or Au evaporated on a glass slide). A room temperature MR of up to 10% was observed in this device at a field of 10 mT.

In the OMAR system, the electrical transport is definitely different from other MR systems, but the spin is still an important property in the electrical transport of the OSCs. Within the OSCs, the charges move through the molecule and cause the polarization of the surrounding lattice due to their Coulomb interactions with the nucleus. The combination of the charge and its accompanying polarization as a quasi-particle is called a polaron,[198] which has the spin of the electron or the hole ($S = 1/2$, $m_s = \pm 1/2$; S is the spin angular momentum and m_s is the spin quantum number) and can either be positively (such as a hole polaron) or negatively charged (such as an electron polaron). The two-like charged polarons (with two positive or two negative charges) could combine together to form the bipolarons[199] and the two-oppositely charged polarons form the excitons. As bipolarons and excitons consist of two charges, there are four spin states in both bipolarons and excitons with three triplet states ($S = 1$, $m_s = +1, 0, -1$) and one singlet state ($S = 0$, $m_s = 0$).[200] The bipolarons, which coexist on the same single molecular sites due to the Coulomb repulsion between charges, could significantly reduce the formation energy (U) of bipolarons because of their sharing of the lattice polarization by placing two charges on the same molecular sites. Thus, bipolarons are always spin singlet due to the presence of large exchange energy between two charges and due to the confinement of the triplet pair of charges to a single molecular site.[201] The excitons are the excited state formed from the electrons and holes, and located at the same molecular sites. The exciton binding energy, which is the difference between the transport gap (E_t) (the difference between the HOMO and LUMO) and the optical gap (E_{opt}), ranges from 0.4 to 1.4 eV due to the formation of excitons.[202] The excited triplet and singlet excitons have very different properties. The energy levels of the excitons and the exciton transitions are depicted in Fig. 7. The transition from the excited singlet state (S_e) to the ground state (G_s, which has the singlet configuration) (the rate constant is k_{SG}) is quantum mechanically allowed since the spin is conserved. Thus, these transitions are fast (1–10 ns) and efficient and cause the fluorescence.[203] The transition from the excited triplet state (T_e) to G_s (the rate constant is k_{TG}) is much slower than the k_{SG} process due to the unallowed transition from the excited triplet state to the singlet ground state according to the spin selection rule (which described that the spin is directional and has the odd parity. The transition in which only states with the total spin quantum number are the same is spin allowed[204]). Therefore, the triplet excitons could live longer in the device (100 μs–10 s) than the singlet excitons.[203] Another transition called ''intersystem crossing (ISC)'' between the S_e state and the T_e state with a rate constant of k_{ISC} is possible to achieve since the spin–orbit coupling weakens the spin selection rules.[205] The transition from T_e to S_e is thermally activated since the T_e state is lower than the S_e state. Thus, the triplet excitons are very important for the electrical transport in the OSCs owing to their long lifetime in the device. The triplet excitons quenching or triplet excitons charge scattering will decrease the mobility, leading to a reduced current.[206] The change in MR is confirmed as a result of the change in the triplet concentration in the OSCs.[207] Desai *et al.*[208] also found that the MR only occurs when there is light emission from the organic light-emitting diode (OLED) device consisting of ITO/*N*,*N*′-diphenyl-*N*,*N*′-bis(3-methylphenyl)-(1,1′-biphenyl)-4,4′-diamine/Alq_3/cathode, which suggests that the MR is related to the formation of the excitons and caused by the trapping of free carriers by triplets.

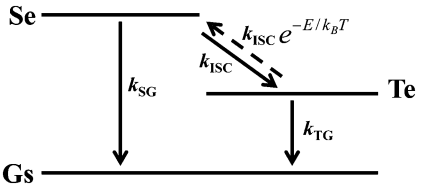

Fig. 7 The transitions between the excited singlet state (S_e), the triplet state (T_e) and the ground state (G_s).

3. Electrical transport phenomena in materials

3.1 Electrical transport phenomenon in materials without magnetic field

Generally, there are three means for electrical conduction through a material: the flow of free conduction electrons in the metals; the flow of ions in ionic liquids or electrolytes; and the

Published on 30 April 2013. Downloaded by University of Tennessee at Knoxville on 10/06/2016 20:55:54.

polarization in which ions (or electrolytes) or electrons move only a short distance under an electric field and then stop (polaronic transport).[209] In the solid state physics, the electronic band structure is normally introduced to categorize the materials into a conductor, a semiconductor and an insulator. The band gap, also called the energy gap, is the energy range between the valence band and the conduction band. The conduction band is the electron energy range for the electrons to move freely within the atomic lattice of the materials, which is called "delocalized electrons" and is the first unfilled energy level at absolute zero temperature (LUMO for molecules). The valence band is the highest energy range and the last filled energy level (HOMO for molecules), in which the electrons present at absolute zero temperature. In the conductor, such as metals, the conduction depends on the free moving electrons since the conduction band overlaps with the valence band, in which there is no band gap. In the semiconductor, such as silicon and germanium, the electrons need to jump over the energy gap to the conduction band with the help of energy (such as light, heat and electric field) because of the presence of a small band gap and the Fermi level of the semiconductor is in the middle of the band gap. The electronic band structure is shown in Fig. 8. However, for the insulator, the conduction band is much higher than the valence band, so that the electrons cannot overcome the band gap to delocalize. The change in the electronic band structure makes the semiconductor conductive. There are many parameters that change the band structure and the Fermi level of the semiconductor, such as dopant concentrations, impurities and temperature.[210] The semiconductor–metal transition could be observed in the heavily doped silicon.[211] In the semiconductor, both the electrons in the conduction band and the holes in the valence band (resulted after electrons are excited to the conduction band) contribute to the electrical conductivity.[212]

In the carbon-based materials, such as graphene and carbon nanotubes, the electronic band structure influences the charge transport.[214] Graphene is a single atomic layer of graphitic carbon densely packed into a two-dimensional (2D) hexagonal structure with the honeycomb lattice,[215] which can be wrapped up into zero-dimensional (0D) fullerene, rolled into one-dimensional (1D) nanotubes or stacked into three-dimensional (3D) graphite.[216] In the electronic properties of graphene,

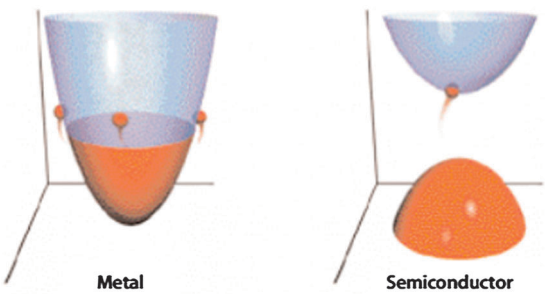

Fig. 8 The electronic band structures of metals and classical inorganic semiconductors (orange represents the valence band and the blue is for the conduction band).[213]

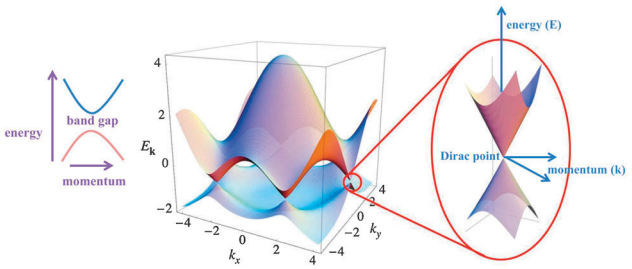

Fig. 9 Electronic band structure of the graphene honeycomb lattice. Reprinted with permission from the American Physical Society.[217]

the σ bands are formed by three of the four valence electrons (sp^2 hybridization) and the fourth single electron of the carbon atom occupies a $2p_z$ orbital to form the π(LUMO) and π*(HOMO) band with neighbors for the delocalization.[214] The valence band and the conduction band of graphene meet at a point, called the Dirac point, Fig. 9. The hybridized electrons with the periodic field of the hexagonal crystal lattice form Dirac fermions, which is expressed as a cone-like energy band.[217] This unique band structure makes the electrons move ballistically within graphene, leading to a higher electrical current than the normal semiconductors, even at room temperature. Graphene nanoribbons are strips of graphene, which are obtained by cutting a graphene sheet along a certain direction.[214] Thus, the edge of the graphene ribbon could be "armchair-like" or "zigzag-like" depending on the cutting direction.[218] The charge transport in the graphene nanoribbons has also been reported to be affected by the edge doping, impurities and functional groups.[219,220] The edge doping is more complex depending on the dopant position, ribbon width and symmetry.[221,222] Martins *et al.*[223] found that the doping with boron atoms can suppress the conduction band near the Fermi level to increase the conductivity. The added boron atoms can behave as scattering centers for the spin up (down) electronic transport within the graphene nanoribbon. Cervantes-Sodi *et al.*[224] observed that the chemical functionalization can break spin degeneracy (the two or more quantum states with the same energy level). This could lead to a spin-selective half-semiconductivity (in which the valence band and the conduction band are at the same spin channel), or spin-polarized half-semiconductivity (in which the valence band and the conduction band belong to the opposite spin channels), or semiconductor–metal-transition.

Carbon nanotubes (CNTs), derived from the layer of graphite ("graphene sheets") and formed by rolling a piece of graphene to create a seamless cylinder, Fig. 10A,[225,226] are one of the most widely studied molecular electronics[225,227,228] due to their unique electronic structure, electrical properties and quantum effects.[229–231] There are two types of carbon nanotubes including single-walled carbon nanotubes (SWNTs) and multi-walled carbon nanotubes (MWNTs).[232] SWNTs only have one-atom-thick layer of graphite (also called graphene), whereas MWNTs consist of multiple rolled layers of graphene.[233] Particularly, the diameter and the helicity (which could be represented by an axial vector,[234] *i.e.* chirality)

 This journal is © The Royal Society of Chemistry 2013

Published on 30 April 2013. Downloaded by University of Tennessee at Knoxville on 10/06/2016 20:55:54.

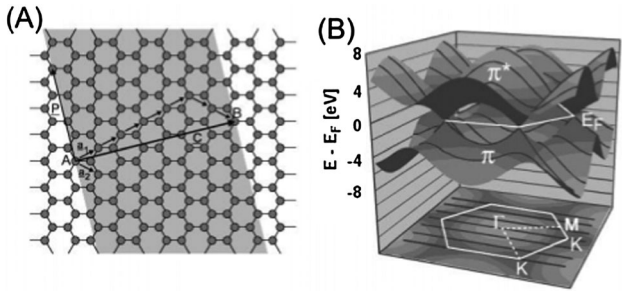

Fig. 10 (A) Generation of carbon nanotubes by folding a graphene sheet; (B) band structure (top) and the first Brillouin zone (bottom) of the graphene sheet. Reprinted with permission from American Chemical Society.[225]

of carbon atoms in the nanotube shell could be used to determine whether the CNTs are metallic or semiconducting.[214,235] After folding a graphene sheet, Fig. 10A, the CNTs could be characterized by the chirality vector (C, *i.e.* geometry) $C = na_1 + ma_2 \equiv (n, m)$,[236] where a_1 and a_2 are the unit vectors of the hexagonal lattice shown in Fig. 10A. And the obtained $C = 5a_1 + 2a_2 \equiv (5, 2)$ indicates that this folding CNT can be expressed as (5, 2).[225] The band structure and first Brillouin zone of graphene are shown in Fig. 10B. In this band structure, the valence band (π) and the conduction band (π^*) meet at each of the six points (*i.e.* k-point) at Fermi energy, the top of Fig. 10B. In the k-space (2D or 3D Fourier transform measured in the magnetic resonance image), bottom of Fig. 10B, the electrons behave as a semiconductor in the Γ–M direction, while in the Γ–K direction and other five directions, the electrons could move freely and behave as a metal.[225] The SWNTs have different band gaps depending on their diameters. The smallest-diameter SWNTs have the highest band gap and the band gap decreases with increasing diameter. The diameter dependent properties make SWNTs behave as a metal (zero band gap) or as a silicon semiconductor.[213] The MWNTs have more complex behaviors since each layer in the tube has a different geometry.[213]

The charge transport relying on the change in the electronic band structure is also called bandlike transport. For the OSCs, the mechanism of charge transport is still controversial in the literature, however, it could be classified into two models according to the type of OSCs.[237] For the single crystals of small molecules like tetracene, pentacene and rubrene with the chemical structures shown in Fig. 11, several researchers have reported that the bandlike transport behavior (*i.e.* band structure conduction), in which the field-effect mobility increases with decreasing temperature due to the increased scattering of charge carriers on phonons (thermally induced crystal deformation),[237,238] still plays an important role.[237,239] However, in the disordered OSCs, particularly, in the polycrystalline or amorphous π-conjugated polymer systems, the weak intermolecular van der Waals forces lead to a relatively narrow bandwidth, stronger electron lattice interactions and the formation of more polarons.[240] As the temperature increases, the electron–phonon coupling results in an enhanced polaron mass and decreased bandwidth, which may ultimately lead to the localization of charge carriers. Thus, the charge transport occurs by the phonon-assisted tunneling or hopping and is strongly temperature dependent.[241] In this hopping mechanism, the field-effect mobility increases with increasing temperature because of the increased thermal activation.[237] Due to the energetic disorder originating from the disordered structure,[242] the band structure cannot be used in these disordered OSCs. The electronic states of the molecules in OSCs are subject to random energetic variations arising from the factors including variations in conjugation length, rotations and kinking of the polymer chains, van der Waals interactions with neighboring conjugated molecules, impurities,[243] dipole moments of the neighboring dopant molecules and dipole moments of the molecules of the polymer matrix (dipole is a pair of electric charges with equal magnitude but opposite sign).[244] The energetic disorder is that the bands in the density of states (DOS) corresponding to the HOMO and LUMO states behave as a tail of low-energy states extending far into the normal energy gap, Fig. 12. The energetic disorder could be approximated using the Gaussian disorder model (GDM) as formulated by Bässler.[245] In this model, the symbol σ is used to represent the width of the energetic disorder; the activation energy of the mobility is expressed as $(2\sigma/3)^2/k_BT$, where k_B is Boltzmann's constant, T is the absolute temperature, μ_0 is the

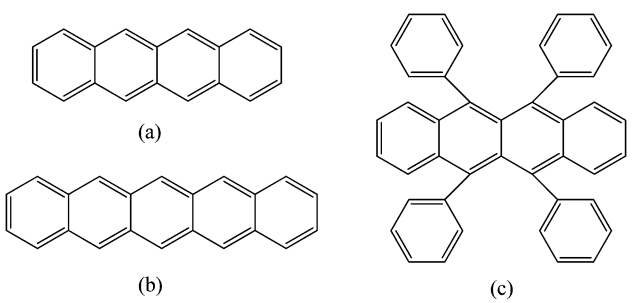

Fig. 11 Chemical structures of (a) tetracene, (b) pentacene, and (c) rubrene.

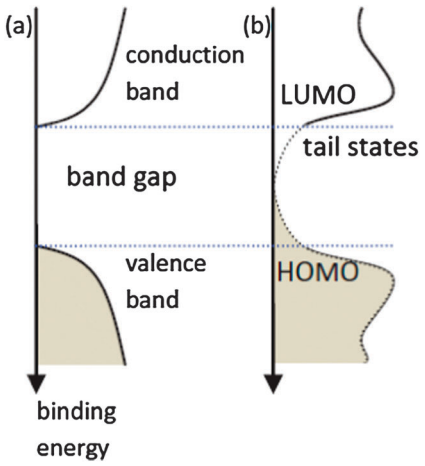

Fig. 12 Schematic of density of states (DOS) for (a) the classical crystalline inorganic semiconductor and (b) disordered OSCs showing the tail states extending into the band gap. Reprinted with permission from the American Physical Society.[243]

Published on 30 April 2013. Downloaded by University of Tennessee at Knoxville on 10/06/2016 20:55:54.

mobility extrapolated to the zero electric field. Thus, the carrier mobility μ could be described by eqn (7):[246]

$$\mu = \mu_0 \exp\left[-(2\sigma/3k_BT)^2\right] \times \exp\left\{C\left[(\sigma/k_BT)^2 - \Sigma^2\right]\sqrt{E}\right\} \quad (7)$$

where C and Σ are constants. The GDM describes the transport as a biased random walk among the dopant molecules with Gaussian-distributed random site energies. According to the GDM, the energetic disorder could be Gaussian distributions with a characteristic energy width of $\sigma \sim 0.1$ to 0.2 eV.[247,248]

The energetic disorder causes the charges to be localized on the molecular sites and the mechanism for charges moving from one localized site to another is associated with the "hopping", which is called "variable range hopping (VRH)". In the disordered material systems with localized states in the band gap, the conductivity is often described as Mott's law for the VRH. In Mott's law, the conduction caused by the phonon-assisted tunneling (hopping, dependent on the thermal energy, k_BT)[249] between electronic localized states centered at different positions can be expressed as eqn (8):[250]

$$\sigma = \sigma_0 \exp\left[-\left(\frac{T_0}{T}\right)^{1/(n+1)}\right],\ n = 1, 2, 3 \quad (8)$$

where the pre-exponential factor σ_0 is a constant, which represents the conductivity at an infinite low temperature limit, T is the Kelvin temperature, T_0 is the hopping barrier, which stands for the characteristic Mott temperature, and is expressed as eqn (9):[251]

$$T_0 = 24/[\pi k_B N(E_F) a_0^3] \quad (9)$$

where a_0 (nm) is the localization length of the localized wave function, k_B is Boltzmann constant and the $N(E_F)$ is the density of states at the Fermi level. The n value of 3, 2, and 1 in eqn (8) represents three-, two-, and one-dimensional systems, respectively. Since the hopping transport is the main contribution to the electrical transport in the OSCs, the mobility of charge carriers (including electrons and holes) in the OSCs is several orders of magnitude lower than that in the inorganic semiconductors. For example, the charge carrier mobility in the amorphous OSCs is in the range of $\sim 10^{-6}$ to 10^{-2} cm^2 V s^{-1} and for the high purity crystals of rubrene, the charge carrier mobility is about 10 cm^2 V s^{-1}. However, the mobility of the high purity silicon crystals is almost 10^3 cm^2 V s^{-1}.[176]

3.2 Electrical transport in materials under a magnetic field

Electrons have charges and spins, which have been considered separately recently.[252] In the classical electronics, the charges move by the electric fields to transmit information and are stored in a capacitor unit. These moving charges form the electrical current in the electronic devices. However, since the discovery of GMR in 1988, the spin current has replaced the charge current in the electronics under a magnetic field.[75] The spin transport (current) has different types in different materials. In the FM metals, the spin dependent conduction arises from their typical electronic band structure, Fig. 4. The spin splitting between the energy bands of spin-up and spin-down electrons renders the electrons in different states at the Fermi level and exhibits different conduction properties for carrying the electrical spin current. These differences lead to the formation of spin polarized currents, which contribute to the electrical transport of the FM metals under the magnetic fields.[253] Recently, the spin transport in the semiconductors has gained much more attention since it could combine the potential of semiconductors (current could be controlled by gate, coupling with optics, *etc.*) with the potential of magnetic materials (current could be controlled by spin manipulation, nonvolatility, *etc.*).[254] The spin polarized current flows through a lateral channel between a spin-polarized source and a drain in the semiconductors. However, the injection of spin-polarized current from magnetic metals into semiconductors has a problem, which is called "conductivity mismatch". This could be solved by the introduction of tunnel junction at the interface of magnetic metals and semiconductors.[255,256] The spin-polarized current in semiconductors could also be induced by the spin–orbit effects (also called the spin Hall effect (SHE)),[257,258] in which spin–orbit interaction deflects the currents of spin up and spin down channels in the opposite transverse directions, inducing a transverse spin current.[254] The spin transport in the CNTs is ballistic,[259] which means that the length of the conductor is smaller than the electronic mean free path (in ballistic transport, there is no dissipated energy in the conductor).[234] In the OSCs, such as rubrene, the spin transport arises from the spin polarized tunneling (hopping) through the weakly-coupled and localized molecular levels.[260] The electrical conductions under the magnetic field in different MR devices, such as OMR, AMR, *etc.* have been discussed in Section 2.

4. Spintronics

The GMR effect is considered as the birth of spintronics.[30,31,261] Spintronics is an emerging technology (where it is not the electron charge but the electron spin that carries information) and is associated with both intrinsic spin of electrons[262] and their magnetic moment in a solid-state system.[80] Spintronics utilizes the electronic spin degree of freedom (which is intrinsically a quantum-mechanical phenomenon,[263] indicating that the electrons are free to occupy different spin states at the electronic states with the same energy or nearly the same energy) in the solid-state systems for information storage and logic operations, which could decrease the power consumption, increase the data processing speed and enhance the integration densities compared to the conventional semiconductor devices.[75,80,264] Therefore, the technical issues including efficient spin injection, spin transport, control and manipulation, detection of spin polarization and spin-polarized current are very important for the successful incorporation of spins into the existing semiconductor technology since the injection and detection of spin-polarized current in a semiconducting material could combine magnetic storage of information with electronic readout in a single semiconductor device.[265] The Hanle effect, which was first used for optical detection of

 This journal is © The Royal Society of Chemistry 2013

Published on 30 April 2013. Downloaded by University of Tennessee at Knoxville on 10/06/2016 20:55:54.

nuclear polarization, has been widely used to assess the spin injection in the semiconductor spintronics.[266–268] The Hanle effect experiment involves the induced injected-spin precession by applying an external magnetic field when these injected spins traverse from the injector to the collector across the device.[269] However, this effect has not been detected inside the OSCs, and whether the Hanle effect could be detected in an organic system with the incoherent hopping transport of carriers is still under debate, indicating that spin injection in these organic junction systems is not clear so far.[176] The understanding of the interaction between the electron spin and its solid-state environments is the goal of the spintronics for making useful devices.[80] The spin relaxation (how spins are created and disappeared) and spin transport are the fundamental studies in the spintronics.[270] Recently, there have been many *ab initio* calculations based on the first principles, such as the two-spin current model (which was introduced by Mott[271]),[272] density functional theory (DFT, which was derived by Hohenberg, Kohn and Sham[273–276]), non-equilibrium Green's function (NEGF),[277,278] and non-equilibrium Green's function-density functional theory (NEGF-DFT),[279] for studying the spin transport properties and electronic structure of Fe–Cr multilayers,[272,275] GaAs doped with Mn,[276] graphene,[279] carbon nanotubes,[280,281] organic molecules such as pentacene[277] and Alq_3.[282] The understanding of the spin transport within the materials from theoretical point of view is important for the deeper understanding of the transport mechanism and will be helpful for designing new types of spintronic devices.[283] Even though many spintronic applications are based on the GMR effect, the observation of TMR has gained much more attention in the MTJs for its applications in spintronic devices.[284,285] To seek desirable materials for spintronic device applications, the highly spin polarized materials would provide a large MR effect, such as half-metallic ferromagnets. More details about the fundamentals of spintronics have been reviewed by Žutić and coauthors.[80]

5. GMR effects in molecular systems

5.1 Tris(8-hydroxyquinolinato)aluminum (Alq_3)-based systems

Tris(8-hydroxyquinolinato)aluminum (Alq_3, $C_{27}H_{18}N_3O_3Al$) with its chemical structure shown in Fig. 13 has served as OSC spacers in organic GMR systems[286,287] due to its chemical flexibility and optoelectronic properties.[195] Alq_3 is most commonly used in organic light-emitting diodes (OLEDs) with green emission[288] because it can be easily deposited as thin films and integrated with a variety of metallic electrodes.[7,121,179,181] It has been reported that the interface between FM electrodes and nonmagnetic substances in the GMR devices controls their performance[80] and the spin injection will be blocked at the interface because of the mismatched conductivity.[289] This is also a problem for spin injection from FM electrodes into OSCs because the OSCs have rather low conductivity compared to metals. Thus, in the OSC-based GMR devices, the half-metallic LSMO is often used for the FM electrode to solve this problem since it shows almost 100% spin polarization.[130] Xiong *et al.*[7] fabricated an organic spin-valve device, which consisted of a bottom LSMO electrode and a top FM Co electrode[290,291] sandwiched with a thick layered vacuum-evaporated Alq_3 spacer (between 130 and 250 nm), Fig. 14a. Under a sweeping external magnetic field, the device with a 130 nm thick organic layer exhibited a negative GMR of up to 40% at 11 K, but was almost reduced to zero when the temperature was increased to 300 K. The GMR in this sandwich system was strongly dependent on the temperature, bias voltage and Alq_3 spacer thickness, Fig. 14b.

Vinzelberg *et al.*[292] investigated the GMR effects in an organic spin valve system, consisting of Alq_3 as a spacer and a FM Co top layer with a LSMO-based electrode. The electron transport behavior in the LSMO–Alq_3–Co system was studied. The TEM microstructure shows a smooth interface between Alq_3 on the nanometer scale and Co, and there is no indication for enhanced roughness, Fig. 15a.

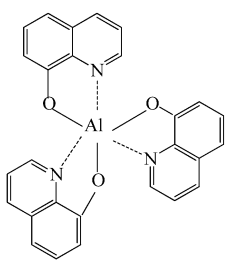

Fig. 13 The molecular structure of Alq_3.

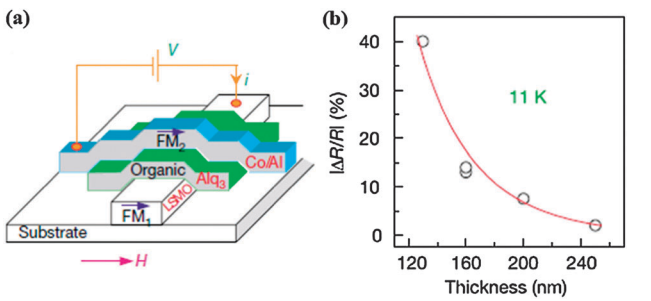

Fig. 14 (a) Schematic structure of the typical device; (b) GMR values of LSMO–Alq_3–Co devices with different thicknesses. Reprinted with permission from the Nature Publishing Group.[7]

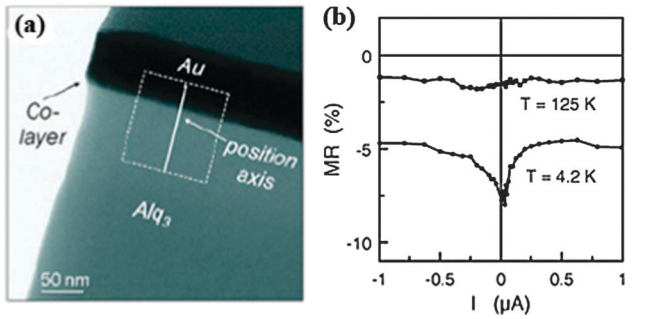

Fig. 15 (a) TEM on the Alq_3/Co/Au interface; (b) MR values for the device at different temperatures. Reprinted with permission from the American Institute of Physics.[292]

Published on 30 April 2013. Downloaded by University of Tennessee at Knoxville on 10/06/2016 20:55:54.

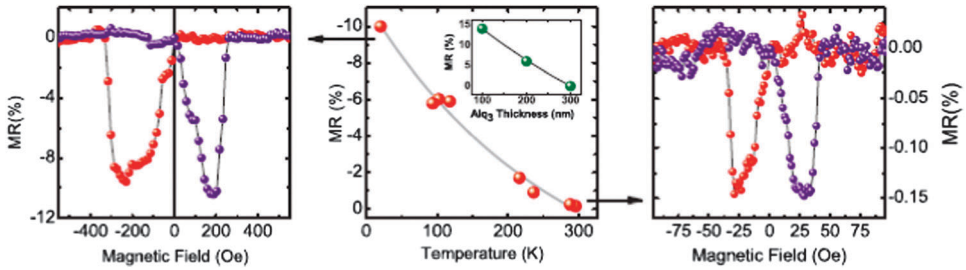

Fig. 16 Observed MR in the LSMO–Alq_3–Al_2O_3–Co spin-valve system. The voltage dependent MR is slightly asymmetric for this device. Reprinted with permission from the American Physical Society.[181]

The obtained negative MR was observed to be temperature and bias voltage dependent without any systematic dependence on the Alq_3 layer thickness and device area, Fig. 15b.

Dediu *et al.*[179,293] investigated the electronic structure of the interfaces among Alq_3, Co and LSMO, and the band alignment of the LSMO–Alq_3–Co system using photoelectron spectroscopy. The chemical interaction was found between Alq_3 molecules and Co atoms with Co penetrating into the Alq_3 layer upon vapor deposition of Co atoms. This observation is very important for understanding the spin-valve behavior. An inorganic thin Al_2O_3 tunnel barrier was further introduced to improve the top interface (Alq_3/Co) and to limit the penetration of the Co atoms into the organic underlayer.[181] This has solved the ubiquitous problem of so-called "ill-defined layers" caused by the diffusion and penetration of metal atoms into the organic layer and the possible reaction between metal atoms and organic molecules.[7] The negative GMR was detected in the LSMO–Alq_3–Al_2O_3–Co spin-valve system at 20 K and the small MR effect (spin transport) was observed at room temperature, Fig. 16.

Adding an insulating barrier layer such as Al_2O_3 can solve the "ill-defined" organic space layer as mentioned above, however, it is unfavorable for understanding the spin dependent transport mechanism in the organic spin valve by introducing an additional new insulating barrier layer. To solve this problem, Sun *et al.*[294] deposited magnetic nanodots instead of isolated magnetic atoms on the top of the organic layer to minimize the negative effects of the "ill-defined" organic layer without adding the additional insulating barrier layer. Fig. 17 shows the schematic diagram of the new and conventional spin valve device. They used a buffer layer assisted growth (BLAG) to form the top magnetic electrode in a vertical organic spin valve of Co–Alq_3–LSMO, Fig. 17a. The obvious short circuit area was formed in the conventional spin valve device due to the diffusion of Co atoms, Fig. 17b. Compared to the conventional spin valve device, several layers of Co nanodots (average nanodot volume $\sim$ 3.3 nm^3) were formed, Fig. 17c, which efficiently minimized the diffusion problem with a sharper interface, and a GMR value of up to 300% was observed. The mechanism of a large GMR value without any complicated issues was investigated by analyzing the current density–voltage (*I*–*V*) characteristics.

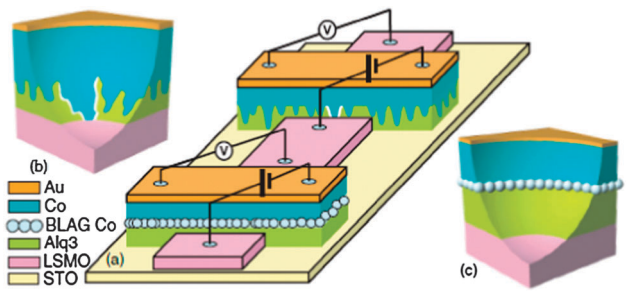

Fig. 17 Schematic diagrams of (a) a BLAG spin valve and a conventional spin valve, (b) formed short circuit area (sketched by a solid white line) due to the diffusion of Co atoms and (c) formed BLAG device with several layers of Co nanodots. Reprinted with permission from the American Physical Society.[294]

Pramanik *et al.*[295] fabricated an organic nanowire spin valve structure with 50 nm diameter consisting of three layers, being Co, Alq_3 and FM Ni in a porous alumina membrane containing a well-ordered hexagonal close-packed arrangement of 50 nm pores. An extremely long spin relaxation time (between a few milliseconds and a second) in this organic nanowire spin valve was reported together with a relative temperature independence of up to 100 K. The spin relaxation mechanisms in the organic Alq_3 have been explored by the Elliot–Yafet (E–Y) mechanism,[296] which was suggested to be dominant due to the large surface-to-volume ratio and reduced carrier mobility. This E–Y mechanism originates from the fact that, in the presence of spin–orbit coupling, the exact Bloch state (or called the Bloch wave, which is the wavefunction of a particle (usually, electron) placed in a periodic potential) is a superposition of spin eigenstates (Bloch states[297]) instead of an individual spin eigenstate, which induces a finite probability of spin-flip (*i.e.* the momentum exchange between the spin-up and spin down electrons, mainly from electron–magnon scattering, which increases with increasing temperature and equalizes partly the spin up and spin down currents at room temperature[253]) when the spatial part of the electron wave function experiences a transition through scattering even if the involved interaction is spin independent.[298] This nanowire spin valve can serve as a platform for spintronics, particularly, opto-spintronic devices such as spin-enhanced OLEDs,[299] which require a long spin relaxation time aiming to exceed the radiation recombination lifetime of excitons in order to increase the efficiency.

5.2 Rubrene systems

Rubrene (5,6,11,12-tetraphenylnaphthacene, $C_{42}H_{28}$) is a conjugated molecular semiconductor that intrinsically transports

 This journal is © The Royal Society of Chemistry 2013

Published on 30 April 2013. Downloaded by University of Tennessee at Knoxville on 10/06/2016 20:55:54.

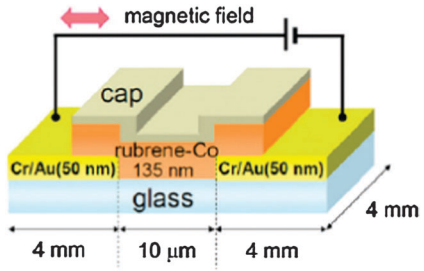

Fig. 18 Schematic structure of the rubrene–Co nanocomposite device. Reprinted with permission from Elsevier.[303]

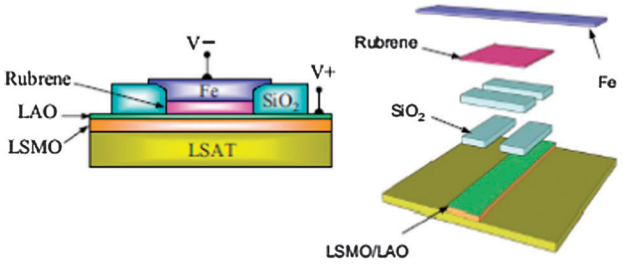

Fig. 20 Schematic of the device structure and the steps of layer deposition. Reprinted with permission from the American Physical Society.[185]

p-type polaronic carriers with high charge-carrier mobility ($\sim$20 cm^2 V^{-1} s^{-1}).[260,300–302] The chemical structure of rubrene is shown in Fig. 11c. Shiraishi *et al.*[303] fabricated the rubrene–Co nanocomposite spin device, which is sandwiched between Cr–Au non-magnetic electrodes, Fig. 18. The very large GMR of 78% was obtained at 4.2 K and only 0.1% of MR was observed at room temperature. The obtained GMR effect is temperature and bias dependent, Fig. 19, which arose from the magnetization of Co and the spin polarization at the rubrene–Co interface. This report disclosed a new function of the rubrene based electronic devices by introducing the spin degree of freedom. They have further studied the enhancement of MR in the rubrene–Co nanocomposite spin devices and the detailed mechanism for this MR enhancement was reported.[304] Briefly, with a narrowed gap length between the electrodes in the rubrene–Co nanocomposites, both the effective electric field between the junctions of the Co nanoparticles and the Coulomb-blockade effect increased (that is, the electrostatic energy for a very small grain will increase by $e^2/2C$ if the electron jumps to this grain, in which e is the electron charge and C is the capacitance of the grain. The electron will not be able to jump further between the grains if the charging energy is not able to be overcome by bias voltage (V) or thermal energy, k_BT, k_B is Boltzmann's constant[305]). This enhanced MR is attributed to the higher-order co-tunneling effect in the Coulomb gap of the rubrene–Co nanocomposite spin device, which was never considered in the conventional theoretical models such as the T–M model (an abbreviation derived from the names of Takahashi and Maekawa[305]).

Yoo *et al.*[185] reported the spin valve devices using LSMO (anode), Fe (cathode) and rubrene (organic spacer). The thin layer (1.2 nm) of $LaAlO_3$ (LAO) was used to improve the interfacial quality between LSMO and rubrene, Fig. 20. The GMR in the

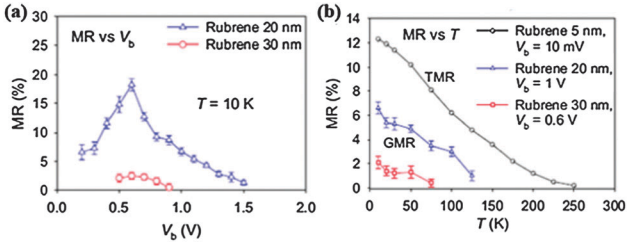

Fig. 21 (a) MR *vs.* V_b plot for 20 and 30 nm rubrene devices at 10 K. (b) Comparison of temperature dependent MR between TMR (5 nm rubrene device) and GMR (20 and 30 nm rubrene devices). Reprinted with permission from the American Physical Society.[185]

20 nm rubrene devices at low bias and low temperature was reported to be extremely high (about 20%) due to the negligible carrier injection, Fig. 21a, while the MR was absent in the thicker rubrene layer because the channel distance was longer than the length scale, over which the traveling electron spin memorizes the initial direction (known as spin diffusion length, λ_s, which is an important measure to achieve the efficient spin injection[306]) in an amorphous rubrene layer when the viable device current was still measurable as long as high bias was applied. The temperature dependent MR, Fig. 21b, revealed that MR decreased with increasing temperature and disappeared at temperatures above 150 K for the 20 nm rubrene device due to the hopping transport and thermionic emission (also called the field enhancement effect, heat induced charge carrier flow from a surface or over a potential-energy barrier because the thermal energy given to the carrier overcomes the binding potential[307]). The GMR effect in the LSMO–rubrene–Fe spin valve device, Fig. 22, was further investigated.[308] The thermionic field emission at the interface of the metal and rubrene was used to describe the carrier injection in this device.

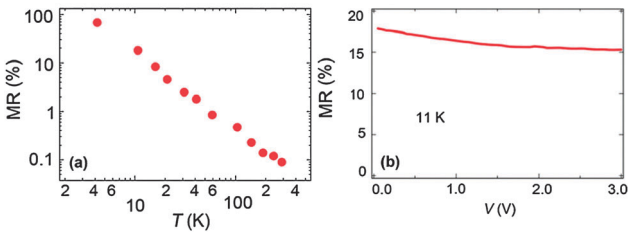

Fig. 19 (a) Temperature dependent MR, and (b) bias voltage dependent MR of the rubrene–Co nanocomposites at H = 20 kOe, T = 11 K. Reprinted with permission from Elsevier.[303]

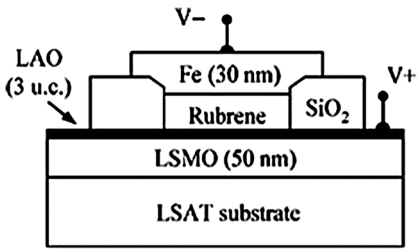

Fig. 22 Schematic of the LSMO–rubrene–Fe spin valve device structure. Reprinted with permission from Elsevier.[308]

Published on 30 April 2013. Downloaded by University of Tennessee at Knoxville on 10/06/2016 20:55:54.

Both empirical and theoretical models as described by eqn (10) and (12), respectively, were used to analyze the carrier injection. During the thermionic field emission, the electrons emitted from thermionic energy converters are rapidly accelerated under the field, and the transit time from the emitter to the electron collector is reduced, consequently reducing the space charge effects.[309] Thermionic field emission takes place at a lower energy and is promising for spin injection–detection.[310] At very low temperatures, both dominating currents from the thermionic field emission and phonon-assisted hopping in HOMO–LUMO levels at the interfaces will introduce strong temperature-dependent device current, which can reflect thermal activation.[185] The observed GMR effect in the 20 nm rubrene spin valve devices arose from the injection and transport of spin-polarized carriers through the OSC rubrene layer.

Eqn (10) is an empirical formula for the thermionic field emission and describes the carrier injection across the barrier for a metal–semiconductor junction:[311]

$$I = I_s \exp\left(\frac{eV}{\alpha k_B T}\right)\left[1 - \exp\left(-\frac{eV}{k_B T}\right)\right], \quad (10)$$

$$I_s = \sigma A^* T^2 \exp\left(-\frac{e\phi}{k_B T}\right) \quad (11)$$

where I is the current, I_s is the saturation current, V is the voltage, k_B is Boltzmann's constant, α is the parameter that addresses the deviation from ideal thermionic emission ($\alpha = 1$), ϕ is the effective barrier height, A^* is the Richardson constant ($A^* = 4\pi m k_B^2 e/h^3$, m and e are the mass and charge of an electron, and h is Planck's constant), and σ is the junction area.

Eqn (12), a theoretical model to describe the carrier injection at the metal/semiconductor interface,[312] defines the value of the phonon assisted tunneling rate of electrons from the deep center to the conduction band under an electric field:

$$W_T = \frac{eE}{(8m^*\varepsilon_T)^{1/2}}\left[\left(1+\gamma^2\right)^{1/2} - \gamma\right]^{1/2}\left[1+\gamma^2\right]^{-1/4} \times \exp\left\{-\frac{4}{3}\frac{(2m^*)^{1/2}}{eE\hbar}\varepsilon_T^{3/2}\left[\left(1+\gamma^2\right)^{1/2} - \gamma\right]^2\left[\left(1+\gamma^2\right)^{1/2} + \frac{1}{2}\gamma\right]\right\} \quad (12)$$

where

$$\gamma = \frac{(2m^*)^{1/2}\Gamma^2}{8\varepsilon\hbar E\varepsilon_T^{1/2}} \quad (13)$$

W_T is the tunneling rate, ε_T is the energetic depth of the center, e is the electron charge, m^* is the electron effective mass value, $E = V_b/d$ is the applied electric field, $\Gamma^2 = 8a(\hbar\omega)^2(2n+1)$ is the width of the defect states broadened by the interaction with optical phonons, $n = 1/[\exp(\hbar\omega/k_B T) - 1]$, and a is the electron–phonon interaction constant ($a = \Gamma_0^2/8(\hbar\omega)^2$), $\hbar\omega$ is a phonon energy.

5.3 Graphene systems

Graphene has attracted considerable attention due to its high electronic mobility,[313] small spin–orbit coupling,[314] gate tunability and long spin lifetime potential.[315–319] Currently, many studies focus on the spin transport in graphene with single-layer or multilayer structures.[320–328] For example, Kawakami *et al.*[321] have reported the MR behaviors of the quasi-two dimensional mesoscopic graphite (MG) spin valves composed of MG flakes with FM electrodes. In this system, an ultrathin magnesium oxide (MgO) was inserted at the FM/MG interface as a tunnel barrier and the spin valve effect was observed with a MR value of up to 12% at 7 K. However, the MR disappeared in the device without MgO, indicating the importance of spin-dependent interfacial resistance for spin injection into MG.[256]

Zhang *et al.*[329] have reported the GMR effect in the zigzag graphene nanoribbon (which is a narrow strip of graphene, width <100 nm[226]) sample, where two sides were deposited with two FM strips, using Landauer–Büttiker formalism combined with the NEGF method, Fig. 23. After obtaining the spin dependent current and conductance, an energy band gap was created around the Dirac point (E_0, which is set zero as the energy zero point) for the antiparallel configuration by magnetization. And no band gap existed for the parallel configuration, indicating that the GMR can be produced when the Fermi energy E_F is located in the gap region. This opened a new possibility of generating GMR in the zigzag graphene nanoribbon.

Rojas *et al.*[3] have studied an ultrasmall and chemically simple MR device based on a zigzag graphene ribbon joining two metallic graphene electrodes, Fig. 24A, using a well-established methodology extended to account for electron–electron interactions in a Hubbard model (which is an approximate model of electron interaction in narrow energy bands to describe the transition between conducting and insulating systems[330]). MR of each device is defined by eqn (14):

$$\begin{aligned} MR &= [(R_{AFM} - R_{FM})/(R_{AFM} + R_{FM})] \times 100 \\ &= [(G_{FM} - G_{AFM})/(G_{FM} + G_{AFM})] \times 100 \end{aligned} \quad (14)$$

where $R = 1/G$ is the resistance, $G = (e^2/\hbar)T(E_F)$ is the conductance calculated with the Landauer formula,[331] e is the charge of an electron, $\hbar$ is reduced Planck's constant, E_F is the Fermi energy and T is the transmission coefficient at E_F.[332] The transmission

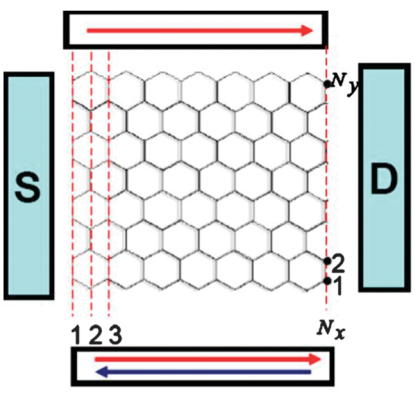

Fig. 23 Schematic of the device: two FM stripes are placed on the top and bottom sides of the zigzag graphene nanoribbon and the source (S) and drain (D) leads are coupled to the graphene ribbon in the x direction. Reprinted with permission from the American Physical Society.[329]

This journal is © The Royal Society of Chemistry 2013

Published on 30 April 2013. Downloaded by University of Tennessee at Knoxville on 10/06/2016 20:55:54.

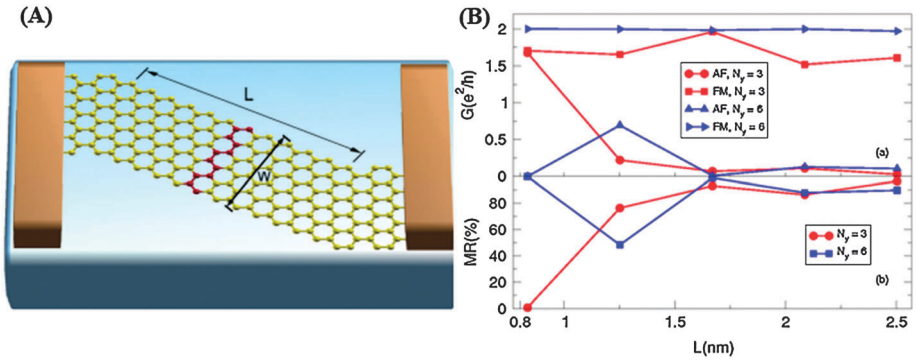

Fig. 24 (A) Atomic structure of the zigzag ribbon with length N_x = 12 and width N_y = 6 attached to semi-infinite electrodes. The unit cell of a zigzag ribbon is highlighted. (B) (a) Conductance and (b) MR at the Fermi energy as a function of ribbon length for two ribbon widths. Reprinted with permission from the American Physical Society.[3]

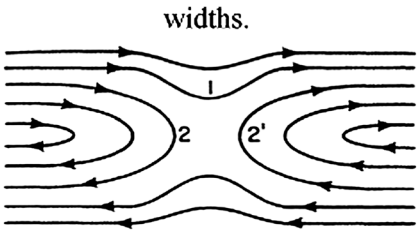

Fig. 25 Images of equipotential contours in the vicinity of a barrier. Reprinted with permission from the American Physical Society.[332]

coefficient is a quantum mechanical concept to describe the behavior of wave incident on a barrier.[333] The electron can transmit across a barrier either by a semiclassical path (trajectory 1 in Fig. 25) or by tunneling through the saddle point (from trajectory 2 to 2′ in Fig. 25).[332] The transmission coefficient must be quantum mechanically calculated by including both possibilities.[332] Based on these demonstrations, the MR was plotted as a function of the ribbon length for ribbons of width N_y = 6 and N_y = 3, (N_y is the width of the graphene ribbon), Fig. 24B, and the proposed device featuring that 100% GMR can be achieved, Fig. 24B-b.

Lu *et al.*[334] have theoretically explored the GMR properties of the functionalized graphene as a high performance 2-D spintronic device using first principles calculations. Five different functionalized graphenes including graphene functionalized with F (F–graphene), O (O–graphene), or OH (OH–graphene) on only one side and graphene functionalized with H on one side and with F (F–graphene–H) or O (O–graphene–H) on the other side were considered. Each functionalized graphene has both chair- and boat-conformations. The magnetism of the functionalized graphenes was studied for different functionalized graphenes. The ferromagnetically coupled and antiferromagnetically coupled states of chair-like functionalized graphene are shown in Fig. 26A. The MR is calculated from eqn (15):

$$\mathrm{MR} = (I_{\mathrm{FM}} - I_{\mathrm{AFM}})/I_{\mathrm{AFM}} \quad (15)$$

where I_{FM} and I_{AFM} represent the current density of the FM and AFM solution, respectively, and the curves of total current (I) of the FM and AFM solutions as a function of V_{bias} of the chair-like F–graphene model are shown in Fig. 26B-a. The obtained MR value is shown in Fig. 26B-b. The resulting maximum room-temperature GMR was up to 2200%, which is one order of magnitude larger than the available experimental values. This investigation makes functionalized graphene a promising material for high performance 2-D spintronic devices.

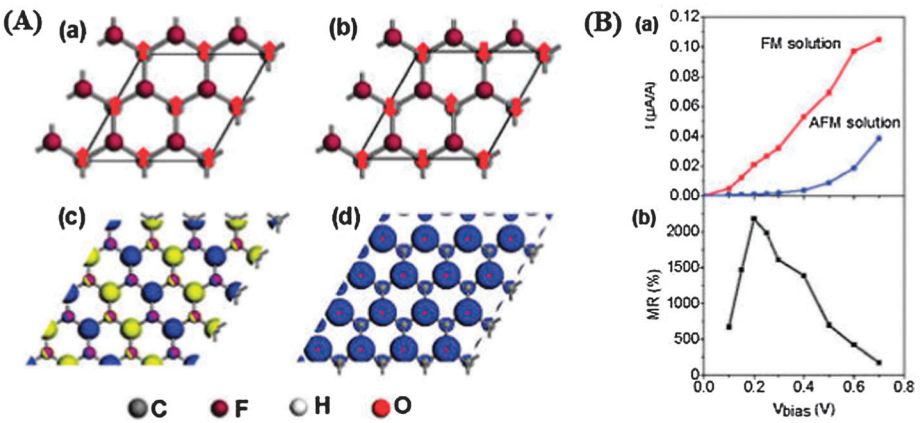

Fig. 26 (A) (a) FM and (b) AFM configurations of the chair-like functionalized graphenes, (c) the AFM chair-like F–graphene, and (d) the FM chair-like O–graphene–H; (B) (a) *I*–*V* bias curve, (b) bias dependent MR. Reprinted with permission from American Chemical Society.[334]

Published on 30 April 2013. Downloaded by University of Tennessee at Knoxville on 10/06/2016 20:55:54.

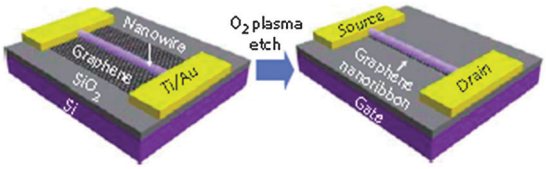

Fig. 27 Schematic graphene nanoribbon field-effect transistors. Reprinted with permission from the Nature Publishing Group.[335]

Bai *et al.*[335] have fabricated the graphene nanoribbon field effect transistors (FETs) using SiO_2 nanowires as physical etching masks without artificially engineered FM electrodes, Fig. 27. A near 100% negative MR with an increased conductance at 1.6 K and nearly 56% negative MR at room temperature were reported, which was attributed to the reduction of quantum confinement through the formation of cyclotron orbits and the delocalization effect under the perpendicular magnetic field.[336–338] With an easy control of the negative MR by the gate voltage and source–drain bias, Fig. 28, these graphene nanoribbon devices have potential applications in the fields of magnetic sensors and magneto-electronic devices.

Candini *et al.*[339] have developed a novel hybrid spintronic nanodevice made by the integration of a graphene nanoconstriction decorated with ternium(III)bis(phthalocyanine) ($TbPc_2$) single molecule magnets. Fig. 29a and b show the schematic of the $TbPc_2$ single molecule magnets and a hybrid spintronic nanodevice, respectively. They used $TbPc_2$ as the molecular magnetic gate to obtain a magnetoconductivity signal of 20% without the FM electrode. Since the scheme of this hybrid nanodevice could be controlled by the backgate voltage V_{bg} and the applied magnetic field, which independently operates on graphene and on the $TbPc_2$ magnetic molecule, respectively, this graphene hybrid nanodevice could be used as field-effect transistors because the on–off conductance could be switched by the backgate voltage V_{bg}. Meanwhile, this hybrid nanodevice behaves similarly to the conventional spin valves when V_{bg} is biased to a resonance conductance.

Generally, the quadratic MR with a small magnitude is observed in the conductor and saturates at a low field.[340] However, the large unsaturated linear magnetoresistance (LMR) is induced by creating the inhomogeneities in the materials.[340] Inhomogeneities create tails in both the conduction and valence bands and cause them to overlap.[341] In order to obtain a LMR, an approximately linear energy spectrum, carriers of very low effective mass and a zero bandgap should exist in the materials. Graphene is one of the perfect platforms for studying LMR due to its unique band structure with a naturally zero bandgap and unusual linearly dispersing electronic excitations.[217] Friedman *et al.*[340] have reported the first observation of LMR in multilayer epitaxial graphene grown in silicon carbide (SiC). The LMR persists in this graphene device from 2.2 K to room temperature (300 K) and is temperature dependent, Fig. 30. The proper control and maximization of graphene device inhomogeneity were claimed to yield an increased magnitude of these LMR effects. The Hall mobility (which is measured using the Hall effect[342] to see the carrier mobility in the semiconductor[343]) as a function of temperature is shown in the inset of Fig. 30B. The mobility decreases slightly with increasing temperature. In Fig. 30B, the inflection data change and the MR slightly increases with increasing temperature when $T > 100$ K probably due to the mobility changes.

The large unsaturated LMR has also been reported by Zhu *et al.*[344] The magnetotransport properties of the compressed

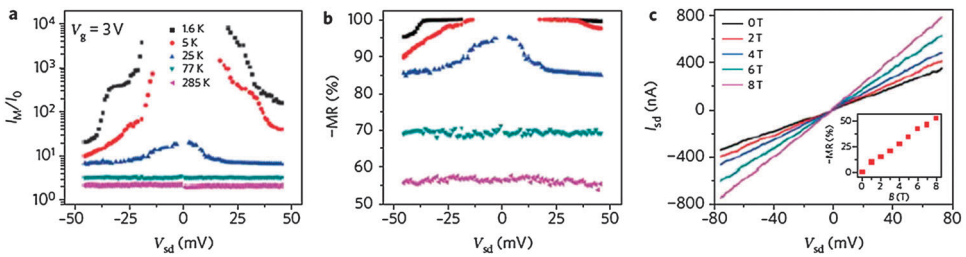

Fig. 28 Temperature dependent MR properties: (a) current ratio $I(8\ T)/I(0\ T)$ and (b) negative MR as a function of source–drain bias at different temperatures. (c) Room-temperature *I vs. V* at different applied magnetic fields. The inset shows the negative MR increasing nearly linearly with increasing the applied magnetic field. Reprinted with permission from the Nature Publishing Group.[335]

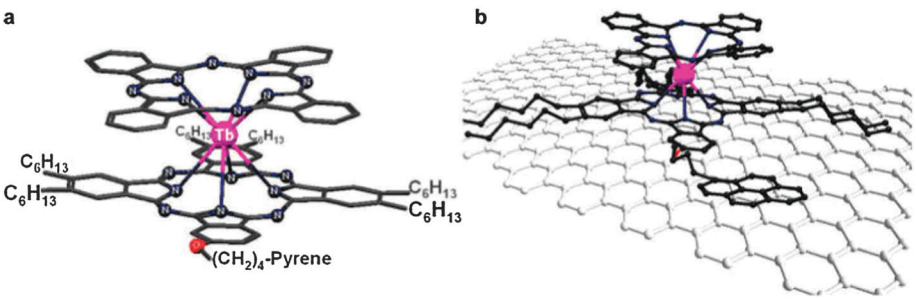

Fig. 29 (a) Schematic of the $TbPc_2$ single molecule magnets and (b) schematic of the nanodevice. Reprinted with permission from American Chemical Society.[339]

 This journal is © The Royal Society of Chemistry 2013

Published on 30 April 2013. Downloaded by University of Tennessee at Knoxville on 10/06/2016 20:55:54.

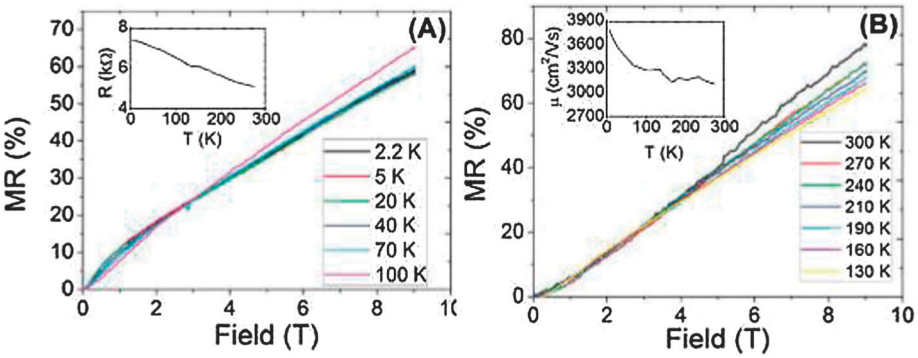

Fig. 30 LMR data in the multilayer epitaxial graphene device at (A) $T \leq 100$ K (the inset shows resistance *vs.* temperature) and (B) $T > 100$ K (the inset shows the Hall mobility *vs.* temperature). Reprinted with permission from American Chemical Society.[340]

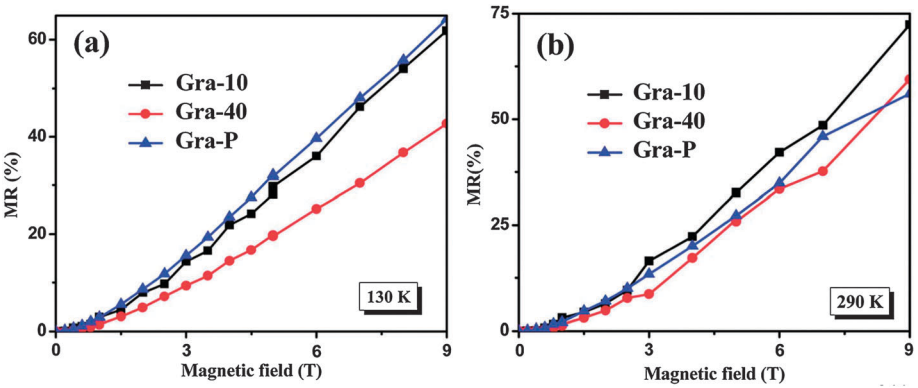

Fig. 31 The MR of Gra-10, Gra-40 and Gra-P at (a) 130 and (b) 290 K.[344]

disk-shaped graphenes with different sizes (N008-100-P-10, *XY*: 5–10 μm, *Z*: 50–100 nm; N008-100-P-40, *XY*: ≤44 μm, *Z*: 50–100 nm; N006-010-P, XY: ≤14 μm, Z: <40 nm, Gra-10, Gra-40 and Gra-P represent the three different graphenes) were investigated. These compressed graphene disks display size dependent behaviors and the MR at a magnetic field of 9 T was observed to vary from 42 to 64% at 130 K, Fig. 31a, and a relatively high value in the range of 56–72% at 290 K was observed, Fig. 31b. These unique MR behaviors may lead to new advanced materials to be applied as extremely linear motion sensors (magnetic sensors)[341] and ultra-high density memory storage.[345] The magnetic graphene nanocomposites (MGNCs) with surface-adhered magnetic nanoparticles, synthesized using a facile thermal-decomposition method,[346] also display classical LMR behavior with the MR values varying from 38 to 64% at 130 K, Fig. 32a, with a higher value of 46–72% at 290 K, Fig. 32b, under an applied magnetic field of 9 T. These MGNCs demonstrate size dependent MR and the MGNCs with small size graphene display a better MR performance at both 130 and 290 K due to the larger disorder of small size graphene

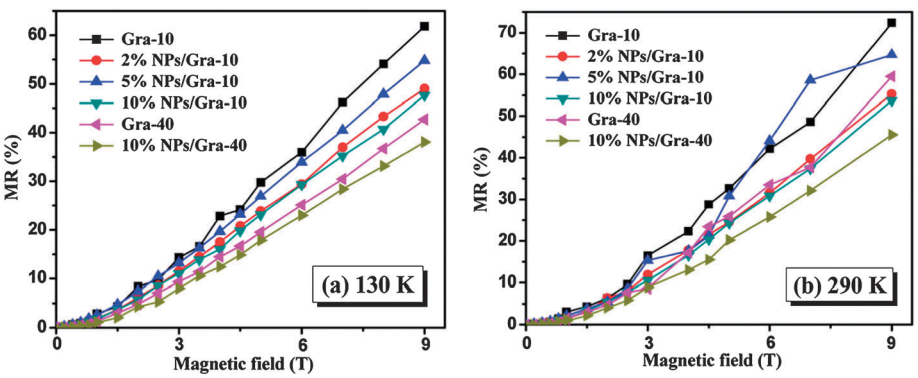

Fig. 32 The MR of graphenes and their nanocomposites at (a) 130 and (b) 290 K.[346]

Published on 30 April 2013. Downloaded by University of Tennessee at Knoxville on 10/06/2016 20:55:54.

and less quantum confinement through the formation of cyclotron orbits and the delocalization effect under the perpendicular magnetic field.[336,338]

Recently, the chemical modification of graphene has been more attractive in the development of graphene based electronics due to the improved properties including tunable band gap[347,348] and magnetic properties.[349] Hydrogenated graphene and graphene nanoribbons are mostly investigated for the spintronic device.[350,351] Matis *et al.*[351] have reported a detailed study on the GMR and quantum localization in plasma hydrogenated graphene. In this system, a negative GMR value of up to 28% in a perpendicular field of 2.5 T was observed at the charge neutral point (in which the density of states should hypothetically vanish for nondisordered and noninteracting electrons[352]) without saturation at 2.0 K and the GMR value was suppressed with the gate voltages accompanied by a transition from strong to weak localization up to carrier densities $n_e \approx 2.6 \times 10^{11}$ cm^{-2}.

5.4 Carbon nanotube systems

The first investigation of spin transport through CNTs was performed by Tsukagoshi *et al.*[353] in 1999 *via* the observation of a hysteretic MR with a maximum resistance change of 9% switching in FM Co contacted MWNTs. Since then, significant progress has been made to disclose the spin injection and transport,[354] enhancement of spin injection[281] and electric field controlled spin transport in CNTs.[355]

SWNTs are more attractive than MWNTs for spin transport studies due to the increased scattering lengths, well-defined electronic band structure, enhanced Coulombic interactions and the possibility of modifying the nanotube resistance with a capacitively coupled gate.[356] The spin transport in ferromagnetically contacted SWNTs has received increasing interests in the last decade.[356] For example, Nagabhirava *et al.*[356–359] have fabricated and characterized ferromagnetically contacted "short channel" individual SWNT devices, which showed clear hysteretic switching in the MR and provided strong evidence of spin transport in SWNTs, Fig. 33. By reducing the transport length separating the FM contacts to distances on the order of 10 nm, the MR between +15 and −10% was observed by varying the gate voltage.

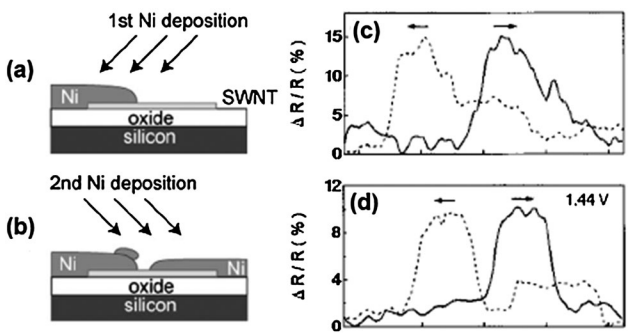

Fig. 33 Fabrication of a short-channel nanotube device: (a) and (b); and hysteretic switching for the MR (c) as a function of magnetic field and (d) for the gate bias of 1.44 V (the solid (dashed) line corresponds to the positive (negative) sweep direction). Reprinted with permission from American Institute of Physics.[356]

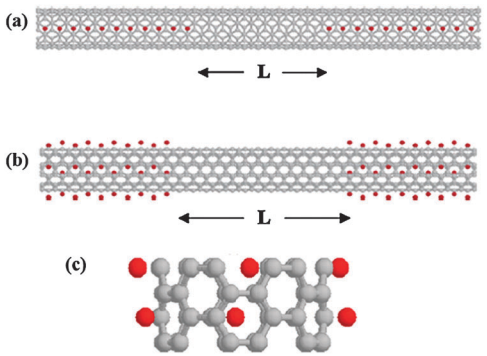

Fig. 34 Armchair carbon nanotubes in contact with FM electrodes: (a) Ni atoms encapsulated along the axis of a CNT, (b) Ni atoms located on the surface of a CNT, and (c) the unit cell of a (6,6) CNT with Ni atoms on the surface. Reproduced by permission of IOP Publishing.[360]

Athanasopoulos *et al.*[360] have reported the theoretical GMR results of SWNTs contacted with FM Ni electrodes. The model of their consideration is shown in Fig. 34. The L was the clean length of SWNTs and the Ni atoms were encapsulated along the axis or located on the surface of SWNTs. The presence of Ni atoms on the surface or axis of the CNT can induce a significant magnetic moment on the carbon atoms, which leads to a room temperature GMR value between 45 and 100% of the anti-aligned conductance.

Ohno *et al.*[361] have reported GMR in the SWNTs contacted with different FM sources and drain electrodes (Fe and Co, Fig. 35), which are different from the conventional CNT spin-valve structures, in which the FM metal electrodes are often the same. The large GMR value of 20% is obtained in the Co–SWNT–Fe system at 8 K, which is very close to 26% of the theoretical value predicted by eqn (16):

$$\mathrm{MR} = \Delta R/R_{ap} = (R_{ap} - R_p)/R_{ap} = 2P_1P_2/(1 + P_1P_2) \quad (16)$$

where R_{ap} and R_p are the resistance in the spin anti-parallel state and the parallel state, respectively, and P_1 and P_2 are conduction electron spin polarizations in the FM metal electrodes 1 and 2, respectively (the CNT spin-valve structures consist of FM metal electrode 1, CNT and FM electrode 2). The spin polarization of Co and Fe was 34 and 44%, respectively,[362] while only 2% MR value was observed for the Co–SWNT–Co system.

Meanwhile, the pressure induced MR transition in SWNTs was observed by Cai *et al.*[363] under the extreme conditions with a hydrostatic pressure of up to 10 GPa, a low temperature down

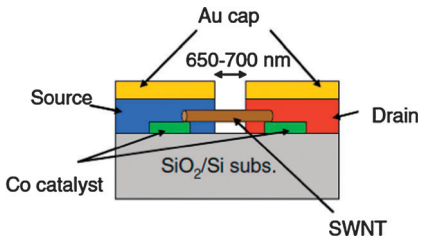

Fig. 35 Schematic illustration of the SWNT spin-valve structure; the combination of source and drain electrodes was Au/Au, Co/Co and Co/Fe. Reproduced by permission of IOP Publishing.[361]

This journal is © The Royal Society of Chemistry 2013

Published on 30 April 2013. Downloaded by University of Tennessee at Knoxville on 10/06/2016 20:55:54.

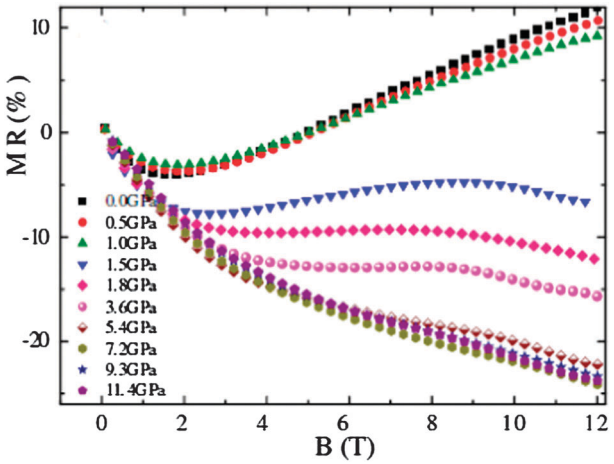

Fig. 36 The field dependent MR at different pressures; the curves from 1.5 to 3.5 GPa show the transition region. Reprinted with permission from the American Physical Society. Reprinted with permission from the American Physical Society.[363]

to 2 K and a high magnetic field of up to 12 T. The pressure induced MR transition from positive to negative in the high field regime was observed to occur from ~1.5 GPa, Fig. 36, which was correlated closely with the tube shape transitions. The measured magnetic field, temperature and pressure dependent MR values were consistent with the model of pressure-induced two-dimensional weak localization (2DWL) as described by eqn (17).[364] This model is possibly dominated by the *e*–*e* scattering between the tubes, which depends on the magnetic field and pressure through the tube shape distortions.

$$\Delta G(B,T) = G(B,T) - G(0,T) = \Gamma\left[\psi\left(\frac{1}{2}+\frac{1}{x}\right) + \ln(x)\right] \quad (17)$$

where ΔG represents magnetoconductance (MC) in the 2DWL model, ψ is the digamma function $\left(\psi(x) = \frac{\mathrm{d}}{\mathrm{d}x}\ln\Gamma(x) = \frac{\Gamma'(x)}{\Gamma(x)}\right)$, $x = B/B_\Phi$ and B_Φ is the 2DWL theory scaling parameter defined as $B_\Phi = \hbar/4eD\tau_\Phi = \hbar/4eL_\Phi{}^2$, where τ_Φ is the phase coherence time, e is the electron charge, $\hbar = h/2\pi$, h is Planck's constant and L_Φ is the phase coherence length related to the inelastic and spin–spin scattering processes.

Recently, Urdampilleta *et al.*[365] have demonstrated a non-magnetic supramolecular spin valve consisting of a SWNT contacted with non-magnetic electrodes and coupled through supramolecular interactions with bis-phthalocyaninato-terbium(III) complex ($TbPc_2$) single molecule magnets. Fig. 37 shows the supramolecular spin valve device. Fig. 37a depicts the molecular schematic of the single molecule magnets $TbPc_2$; the top of Fig. 37b shows the atomic force micrograph of the supramolecular spin valve, which shows that the SWNT lies on a SiO_2 surface supported by a back gate and is connected to the palladium source and drain electrodes. The Zeeman energy (potential energy of the magnetized object in an external magnetic field) released by the molecule during the magnetic moment reversal could modify the chemical potential of nanotubes. They have found that this novel supramolecular spin valve exhibited GMR of up to 300% by reversing the magnetic field at a temperature lower than 1 K.

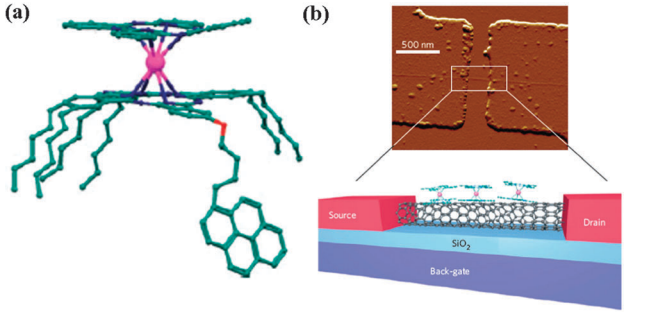

Fig. 37 Supramolecular spin-valve device (a) molecular schematic of the $TbPc_2$ quantum nanomagnet; (b) top: atomic force micrograph of the supramolecular spin valve; and bottom: scheme of the supramolecular spin-valve architecture. Reprinted with permission from the Nature Publishing Group.[365]

The innovation of this device gave the potential design of operable molecular spintronic devices projecting the implementation of new electrical functionalities, high integration depth and an alternative fabrication scheme to cost-intensive lithographic technologies.

There are still lots of research focusing on the GMR effects in MWNTs. For example, Lee *et al.*[366] have measured both the MR and differential conductance of MWNTs as a function of magnetic field. They found that the negative MR mainly originated from the change in density of the states near the Fermi level with the magnetic field rather than a quantum interference effect. Zhao *et al.*[367] have reported the largest spin-coherent transport effect, which was observed in the MWNTs contacted with FM Co pads, Fig. 38a. The MR in this system was found to be strongly bias dependent, increasing with decreasing junction bias, and achieved a maximum MR value of 30% at a junction bias current of 1 nA at 4.2 K, Fig. 38b. The spin transport was claimed to be dominated by the spin dependent tunneling processes at the Co/MWNT interfaces and affected by the local magnetization.

Krompiewski *et al.*[368] have studied the GMR effect in the MWNT system with ultra-small diameters consisting of a single MWNT sandwiched between two FM electrodes, Fig. 39. The GMR of the contacted MWNTs was found to be very sensitive to the interwall coupling strength and the inverse GMR was noticed when all the walls of MWNTs were well coupled to the electrodes. The negative or positive GMR value strongly

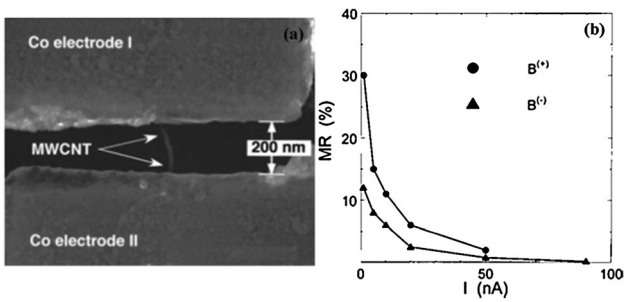

Fig. 38 (a) SEM microstructure of a Co-contacted MWCNT device. The two Co contacts (distance ~200 nm) cover the ends of the nanotube (diameter ~20 nm); (b) MR ratio *vs.* junction bias current for positive and negative magnetic field sweeping directions. Reprinted with permission from American Institute of Physics.[367]

Published on 30 April 2013. Downloaded by University of Tennessee at Knoxville on 10/06/2016 20:55:54.

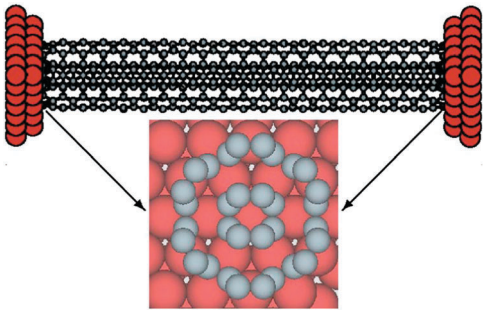

Fig. 39 View of the (2,2)@(6,6) CNTs sandwiched between two fcc(111) leads and details of the contact region. Reprinted with permission from the American Physical Society.[368]

depended on whether the MWNTs contacted the electrodes or not. If the inner nanotubes did not contact any one of the electrodes, the GMR value remained positive even for the relatively strong interwall interactions regardless of the outer nanotube length.

5.5 Conductive polymer and nanocomposite (PNC) systems

Spin transport works better in polymers than that in small molecules due to their conjugation over an extended chain compared with small molecules.[369] Therefore, more GMR studies have focused on the conductive polymer systems. Both positive and negative GMR effects have been observed in conductive polymers and their nanocomposites. Generally, the large and positive GMR is shown in the lower temperature range and decreases with increasing temperature, and sometimes the GMR may change from positive to negative. For instance, large GMR (80%) was obtained in PEDOT/PSS when temperature was below 4.2 K and the GMR was proportional to H^2 (H is the magnetic field strength) in weak magnetic field.[370] With increasing temperature, the value of GMR of polyaniline (PANI)–camphor sulfonic acid (CSA) and polypyrrole (PPy) doped with hexafluorophosphate (PF_6) displayed a transition from positive to negative within the H range from 2 to 8 T.[186] And as a function of H, the GMR will increase with increasing H, and the value of $\ln[R(H)/R(0)]$ is linear with H^2 and $H^{1/3}$ in the weak and the strong field, respectively.[191] The GMR can also be observed in the electrodeposited conductive polymer substrates. For example, Yan *et al.*[371] have described a simple method to prepare the GMR multilayers consisting of Co (2 nm), Cu (3 nm) and conductive PPy (substrate, thickness 5 μm) using the electrodeposition method. The GMR value of around 4% was observed at room temperature.

Long *et al.*[187] have studied the GMR of PANI and PPy nanotube/wire pellets and the single PANI nanotube/wire; a transition from small negative MR to large positive MR was observed in both cases. The positive GMR is associated with the electron hopping transportation and explained using the wave function model. It is suggested that the external magnetic field will contact the overlap of wave functions and cause the required average hopping length to extend, or the hopping length of the electron is decreased, thus the hopping probability of the electron will decrease causing an increased resistance.[370] The negative GMR is discussed with the quantum interference effect among possible hopping paths, in which the magnetic field creates a dephasing time (in which coherence between two quantum states in samples decays[372]) and GMR is proportional to $-H^x \cdot T^{-y}$, where x and y have a constant value with specific dimension VRH.[191] Interestingly, the single PANI nanotube was used to clarify the origin of the MR in the bulk pellet samples and it was observed that the MR in the single PANI nanotube (2.5% at 2 K) was much smaller than that of the PANI nanotube pellet (91% at 3 K). The evident MR transition from negative to positive was not observed in the single PANI nanotubes either. The huge difference between single PANI nanotube and PANI nanotube pellets is related to the interfibril contact in the network of pellets; the single nanotube has a larger hopping length than that of pellet samples, thus the wave-function shrinkage effect and quantum interference effect on single nanotubes are weaker than those on pellets.[187]

Majumdar *et al.*[369] have prepared a polymeric spin valve using LSMO as the bottom electrode and regioregular poly(3-hexylthiophene) (RRP3HT) as the nonmagnetic spacer capped with a Co top electrode. The polymeric material RRP3HT-based spin valve was found to show excellent MR (80%) at 5 K, Fig. 40a, and about 1.5% MR at room temperature, Fig. 40b. Hexamethyldisilazane (HMDS) and dichloro-methyl-octadecylsilane (ODTS) monolayers have been coated as an additional interface between LSMO and RRP3HT and a dramatic decrease in MR at 5 K (MR values were 20%, 0 for the devices containing HMDS and ODTS, respectively)

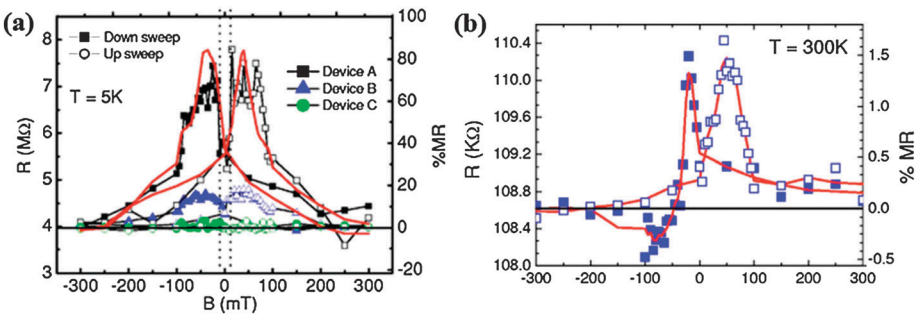

Fig. 40 (a) MR of three different devices at 5 K. Device A: RRP3HT on the top of LSMO; Device B: HMDS-RRP3HT; Device C: ODTS-RRP3HT. (b) MR of device A at 300 K. Reprinted with permission from American Institute of Physics.[369]

 This journal is © The Royal Society of Chemistry 2013

Published on 30 April 2013. Downloaded by University of Tennessee at Knoxville on 10/06/2016 20:55:54.

was observed. The results have indicated that the spin/charge was injected from the bottom LSMO electrode and transferred through the conjugated polymer spacer. The decreased MR arose from the destroyed spin injection by the monolayers (HMDS and ODTS).

Besides temperature and magnetic field strength, GMR can also be affected by other parameters. The GMR in the PNC systems also depends on the loading of fillers. For example, the GMR of the CNTs–PANI composites was negative in 10 K and decreased with increasing CNT loading, the reduction of GMR was associated with the long 1-D localization length of CNTs.[193] However, in the PANI–PMMA (poly(methyl methacrylate)) blends, the GMR was positive and had a larger value at lower PANI concentration.[373] Rakhimov *et al.*[374] have mechanochemically prepared PANI, polystyrene (PS), manganese(II)acetylacetonate ($Mn(Acac)_2$), lanthanum(III)chloride hexahydrate ($LaCl_3{\cdot}6H_2O$), praseodymium(III)chloride hexahydrate ($PrCl_3{\cdot}6H_2O$) and element sulfur (S) polymeric composites with a component ratio of $(LaCl_3{\cdot}6H_2O):(PrCl_3{\cdot}6H_2O):(Mn(Acac)_2):(PANI):(PS):(S)$ = 0.1 : 0.1 : 0.15 : 0.35 : 0.1 : 0.2, and the GMR value range was from 300 to 1800% within various times (0–250 s) at a magnetic field of 6000 Oe and ambient temperature. This GMR value was strongly dependent on the element S and was not observed in the composite material without element S. The S could cross-link with the aromatic chains of PS and PANI during mechanochemical treatment and the obtained composite material in the presence of manganese ions could provide a physical basis for the GMR effect. Gupta *et al.*[375] have synthesized the PANI nanotubes–LSMO composites using the two-step method (a pyrophoric reaction process to prepare LSMO and *in situ* chemical oxidative polymerization to synthesize PANI). A remarkable negative GMR (up to 73%) was obtained in the PANI nanotubes–LSMO composites at 77 K and H = 3 kG (kgauss, 10 kG = 1 T). The GMR value was found to increase with increasing percentage of LSMO nanoparticles in the composites and showed the temperature and magnetic field dependent properties. The observed GMR was attributed to two factors: one is the suppression of spin fluctuation $R_{INT}(H)$ (for the itinerant electrons,[376] the statistical fluctuation of the magnetic moment or spin density, instead of spin wave, is applicable) and the other one is the spin-polarized tunneling $R_{SPT}(H)$. Interestingly, they used eqn (18)–(20)[377] to separate the part of MR_{INT} and MR_{SPT} from the MR to see the main contribution to the temperature dependence; these equations describe the magnetic field dependent MR by taking into account the gradual slippage of domain walls (domain boundaries[378]) across the grain-boundary pinning centers at an applied magnetic field:

$$\mathrm{MR} = -A' \int_0^H f(k)\,\mathrm{d}k - JH - kH^3 \qquad (18)$$

$$f(k) = A\exp(-Bk^2) + Ck^2\exp(-Dk^2) \qquad (19)$$

$$\mathrm{MR_{SPT}} = -\int_0^H f(k)\,\mathrm{d}k \qquad (20)$$

where k represents the pinning strength (the minimum field needed to overcome a particular pinning barrier) of the domain boundaries pinned as the grain-boundary pinning centers in the zero magnetic field, A, B, C, D and J with A' absorbed in A and C are the fitting parameters at the measured temperature, $f(k)$ is the distribution of pinning strengths for the grain boundaries. After fitting the experimental results, it was found that the temperature dependent MR is mainly attributed to the spin-polarized tunneling because the separated MR_{SPT} part rapidly decreases with increasing temperature and exhibits the same trend with MR properties.

Recently, the GMR effect in other PANI PNCs has been reported.[8,9,379] For example, the PANI–Fe_3O_4 PNCs, PANI PNCs with different carbon nanostructures and PANI–$BaTiO_3$ PNCs have been fabricated using the surface initiated polymerization (SIP) method. In the PANI–Fe_3O_4 PNC system, 53 and 95% GMR were obtained, respectively, in pure PANI and its PNCs with a loading of 30 wt% Fe_3O_4 nanoparticles at room temperature, Fig. 41.[8]

In the PANI PNC system with different carbon nanostructures, the small negative MR (<1%) for all the samples was observed at 130 K, Fig. 42a and c, and significantly larger positive MR (15–30%) was observed at 290 K, Fig. 42b and d. The large difference in the MR behavior indicates different electron transport modes at 130 and 290 K, respectively. The quantum interference effect among many possible paths in the magnetic field was used to explain the negative MR at low temperature.[380] The higher GMR at room temperature was observed in the PANI PNCs with 5% loading of graphene than that in the PANI PNCs with the same loading of 1D filler (CNTs and carbon nanofibers (CNFs)) due to the π–π stacking-induced efficient electron transport at the PANI/graphene interface, Fig. 42d.[9] In the PANI–$BaTiO_3$ PNC system,[379] the highest GMR was observed in the PANI PNCs with a $BaTiO_3$ loading of 20.0 wt% prepared with physical mixture of PANI and $BaTiO_3$. The PANI coated $BaTiO_3$ PNCs had a lower GMR value even than pure PANI due to the introduction of $BaTiO_3$, which reduced the function of magnetic field on the contraction of the electronic wave function at impurity centers.

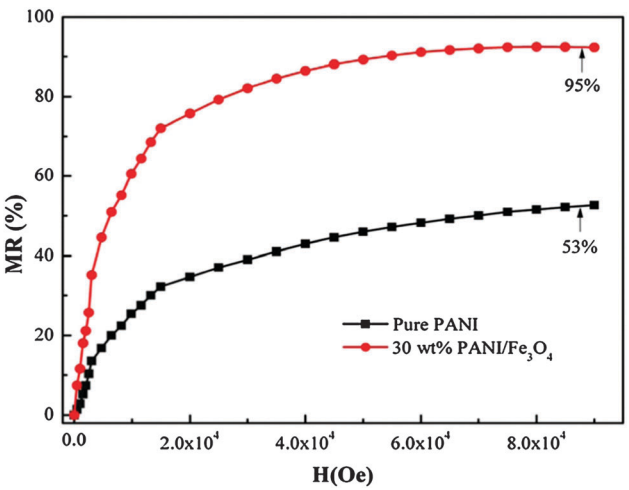

Fig. 41 MR of pure PANI and 30 wt% PANI–Fe_3O_4 nanocomposites at T = 290 K. Reprinted with permission from Elsevier.[8]

Published on 30 April 2013. Downloaded by University of Tennessee at Knoxville on 10/06/2016 20:55:54.

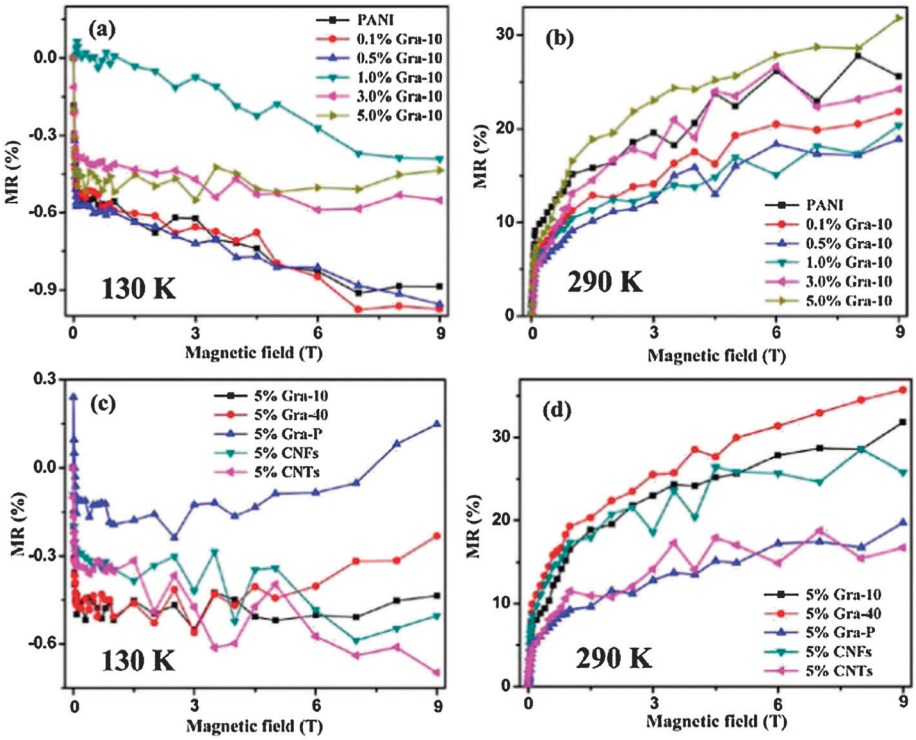

Fig. 42 MR behavior of pure PANI and its PNCs as a function of Gra-10 (graphene) loading at (a) 130 and (b) 290 K; MR behavior of the PNCs filled with 5% weight loading of different carbon nanostructures at (c) 130 and (d) 290 K. Reprinted from American Chemical Society.[9]

5.6 Other molecular systems

The GMR phenomenon has also been studied in other organic systems. For example, Schmaus *et al.*[381] have demonstrated the GMR across a single molecule, a nonmagnetic hydrogen phthalocyanine molecule, contacted by a FM tip of a scanning tunneling microscope. The measured GMR value reached up to 60%. Sugawara *et al.*[382] have reported a detailed description of the first molecule-based pπ–pπ spin-transportation coexisting system of conductivity and magnetism without inorganic magnetic ions, which is through the spin-polarized donor (ESBN) (structure shown in Fig. 43a), a diselena-analogue of the tetrathiafulvalene (TTF)-based carrying the functional group of nitronyl nitroxide (NN). They have described the electronic structure of the spin-polarized donor (ESBN). The coefficients of the singly occupied molecular orbital (SOMO) were localized on the NN group, while those of the HOMO were spreaded over the entire molecule, extending to the NN group. Thus, the sufficient exchange interactions between the π spins in the SOMO and the HOMO can be guaranteed due to the space-sharing nature. Under an exchange field from the π-localized spin in the SOMO, the π electrons in the HOMO become the down spin (β) and the electrons in the SOMO become up spin (α), Fig. 43b.

In addition, the ion-radical salt of a spin-polarized donor, $(ESBN)_2ClO_4$, was found to exhibit a negative GMR phenomenon of 70% at 2 K under a magnetic field of 9 T in spite of the absence of metal ions, Fig. 44. When a magnetic field was applied to the molecular system, most of the localized spins were believed to be aligned to suppress the scattering of electrons, causing the GMR effect.

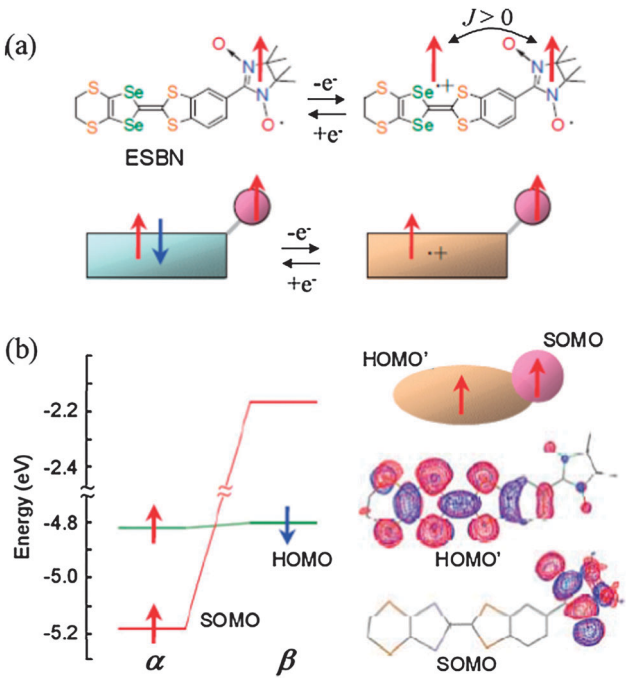

Fig. 43 Schematic of (a) the generation of ground-state triplet cation-diradical species of ESBN upon a one electron redox process at the donor moiety, and (b) the space sharing nature of HOMO′ and SOMO. HOMO′ is derived from one-electron oxidation of the HOMO. Reprinted with permission from American Institute of Physics.[382]

This journal is © The Royal Society of Chemistry 2013

Published on 30 April 2013. Downloaded by University of Tennessee at Knoxville on 10/06/2016 20:55:54.

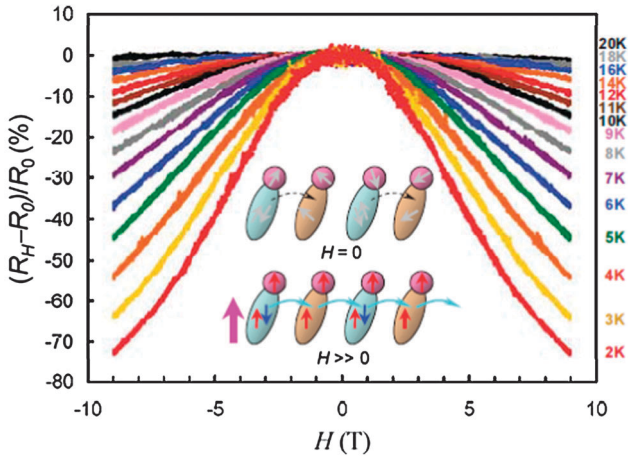

Fig. 44 Magnetic field dependent MR of $(ESBN)_2ClO_4$ at various temperatures at a bias voltage of 7 V. Reprinted with permission from American Institute of Physics.[382]

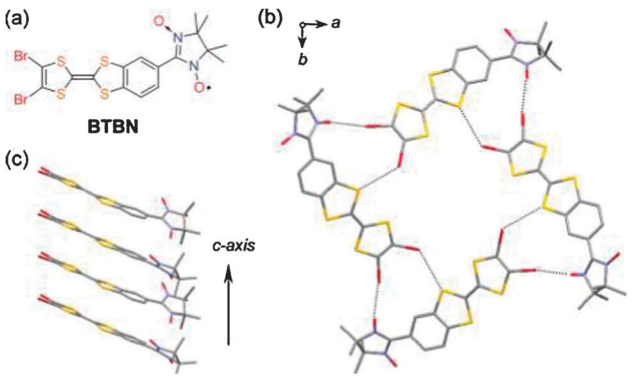

Fig. 45 Crystal structure of BTBN: (a) structural formula of BTBN; (b) molecular arrangement viewed along the *c* axis; and (c) columnar stack along the *c* axis. Reprinted with permission from American Chemical Society.[383]

Sugawara *et al.*[383] have also prepared another donor radical, consisting of a dibrominated benzo-TTF containing a nitronyl nitroxide (NN) group, 2-[2-(4,5-dibromo-[1,3]dithiol-2-ylidene)-1,3-benzodithiol-5-yl]4,4,5,5-tetramethylimidazoline-3-oxide-1-oxyl (BTBN), Fig. 45. The purpose of introducing two bromine atoms into the dithiole ring is to strengthen the intermolecular interactions within its crystal.[384,385] BTBN was found to be conductive upon hole injection from electrodes even at low temperatures. Meanwhile, BTBN was found to exhibit a negative GMR of 76% at 2 K under an applied magnetic field of 5 T.

Dediu *et al.*[6] have reported a strong MR of up to 30% in sexithienyl (T_6, a π-conjugated rigid-rod oligomer) with its structure shown in Fig. 46 under an applied magnetic field by

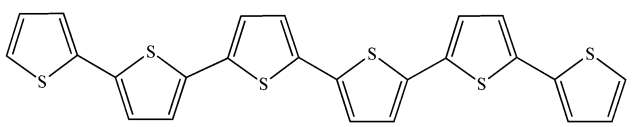

Fig. 46 The structure of T_6.

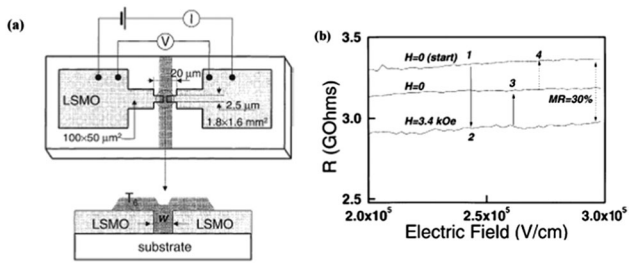

Fig. 47 (a) The schematic of the LSMO–T_6–LSMO spin-valve device and (b) the detected MR as a function of magnetic field. The thickness of LSMO film is 100 nm and T_6 film thickness is 100 nm. Reprinted with permission from Elsevier.[6]

using LSMO electrodes at room temperature, Fig. 47, which was recognized as the first communication on spin injection in OSCs. The spin diffusion length in T_6 is about 200 nm at room temperature. From the obtained results, the interface between LSMO and OSC was regarded as very different from the interface between the metal and the epitaxial inorganic semiconductor, where the chemical potential continuity of carriers played the strong selection rules on spin transfer.[289] The spin–orbit interaction and hyperfine interaction are thought to follow the very important spin-flip mechanism. The wave functions for the delocalized p-orbitals in a π-conjugated oligomer had zero amplitude on the nucleus sites, which minimizes the effect of hyperfine interaction. The spin scattering on thermal phonons was considered to be an important process for the spin-flip effect.[386]

Ikegami *et al.*[387] have prepared the planar-type sandwich structures composed of low-molecular weight OSCs including pentacene, Fig. 48a, and bis(1,2,5-thiadiazolo)-*p*-quinobis-(1,3-dithiole) (BTQBT), Fig. 48b, with LSMO electrodes. The schematic structure is shown in Fig. 48c. The pentacene-based device with a gap of 200 nm electrodes exhibited a MR value of about 6% at 5.3 K, Fig. 49a, while the BTQBT-based device with 200 nm gap electrodes exhibited a MR value of 8.8% and the same device with a gap spacing of 50 nm exhibited a MR value of 29%, Fig. 49b and c. The MR value was observed to depend on the applied bias voltage, temperature, gap spacing of the electrodes, and crystallinity of the BTQBT film. The MR value was also observed to be affected by the gas adsorption onto the films. After left in dry air for 3 h, the MR value of the BTQBT-based device decreased from 6.5% (as-prepared device, 50 K) to 1.2% (after exposure to air), indicating that the spins were scattered by holes in the films generated through charge transfer from gas molecules.

6. Mechanisms of the OMAR effect in the molecular systems

The mechanisms of OMAR are still open for discussion;[388] most research on OMAR is based on the spin–orbit coupling and hyperfine interaction. For example, Sheng *et al.*[389] have explored the hyperfine interaction caused OMAR effect using both experimental data and the theoretical model

Published on 30 April 2013. Downloaded by University of Tennessee at Knoxville on 10/06/2016 20:55:54.

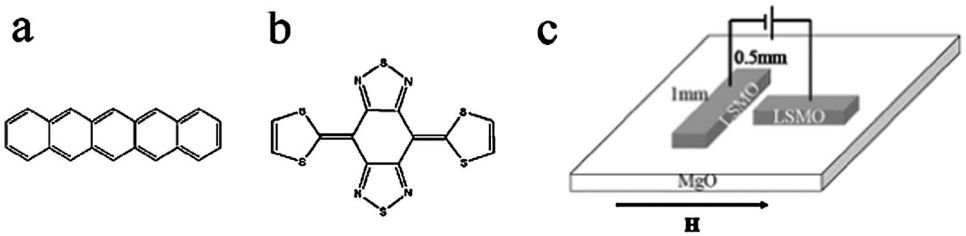

Fig. 48 Molecular structure of (a) pentacene and (b) BTQBT; and (c) schematic illustration of LSMO electrodes (1 mm × 0.5 mm × 100 nm) prepared on MgO. Reprinted with permission from American Institute of Physics.[387]

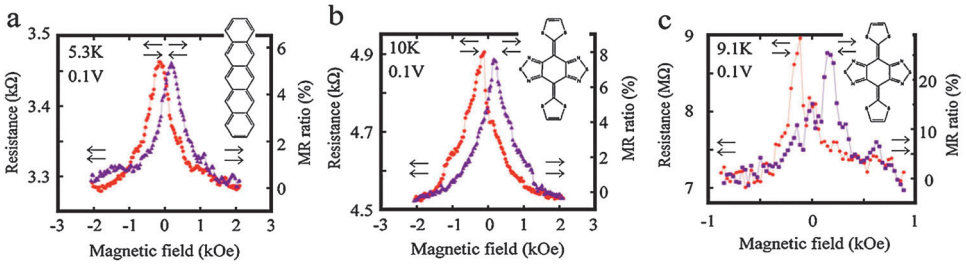

Fig. 49 MR of (a) pentacene-based device (5.3 K, 0.1 V, 200 nm gap), (b) BTQBT-based device (10 K, 0.1 V, 200 nm gap), and (c) BTQBT-based device (9.1 K, 0.1 V, 50 nm gap). Reprinted with permission from American Institute of Physics.[387]

(excitonic pair mechanism model) and the results show that the GMR data can be well fitted with the empirical law of OMAR as shown in eqn (21):[389]

$$\frac{\Delta I}{I} \propto \frac{H^2}{(|H| + H_0)^2} \quad \text{(for non-Lorentzian line shape)}$$

or

$$\frac{\Delta I}{I} \propto \frac{H^2}{(H^2 + H_0^2)} \quad \text{(for Lorentzian line shape)} \qquad (21)$$

where $\Delta I/I$ is the magnetoconductance ratio, I is the current, ΔI is the change in current, H is the magnetic field and H_0 is the characteristic magnetic field. H_0 is the half width at half maximum in the case of the Lorentzian and the half width at quarter maximum in the case of the non-Lorentzian line shape.[14] The selection of model type is dependent on the materials; for example, the PEDOT–polyfluorene–Ca system obeys non-Lorentzian line shape and the PEDOT–regioregular poly(3-hexylthiophene) (RRP3HT)–Ca system obeys Lorentzian line shape.[14] The common models to explain the OMAR effect in the organic systems are excitonic pair mechanism model, electron–hole (e–h) recombination model, bipolaron model, forward interference model and wavefunction shrinkage model. These are detailed as follows.

6.1 Excitonic pair mechanism model

The excitonic pair mechanism model is an example of the spin-dependent effect involving a negative polaron and a positive polaron.[389] In this model, electrons and holes are injected from the cathode and anode into the material and form negative and positive polarons, respectively. When the distance between them is larger than the Coulomb capture radius r_c ($r_c = e^2/4\pi\varepsilon_0\varepsilon_r k_B T$, defined as the distance at which the Coulomb attraction energy is equal to the thermal energy, $k_B T$[390]), the electrons and holes are considered as free charge carriers. However, when the separation distance becomes less than r_c, they will form bound polaron pairs and the pair may further become exciton. There are four kinds of excitons in the material; ^{1}PP is singlet spin pair and $^3PP_0$, $^3PP_+$, $^3PP_-$ are three kinds of triplet spin pairs, where the superscript (subscript) represents the multiplicity (spin injection). The multiplicity of PPs changes with time because of the spin dynamics induced by the hyperfine interaction, which is the basic idea of the excitonic pair mechanism model. The schematic energy level diagram for the simplest possible pair mechanism model is shown in Fig. 50. There are three different species in this diagram: (i) free charges with population C, (ii) polaron pairs PPs and (iii) singlet (S_e) and triplet (T_e) excitons with large exchange interaction J. The simplified rate equation (neglect the upward transitions, dashed arrows in Fig. 50) is obtained

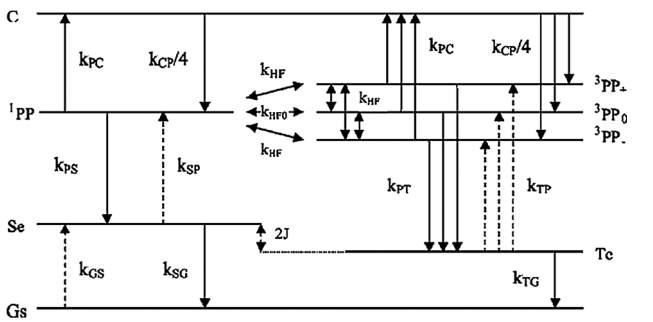

Fig. 50 Schematic energy level diagram of the simplest possible pair mechanism model. S_e and T_e are the singlet and triplet excitons, respectively. J represents the large exchange interaction and G_s is the ground state. Reprinted with permission from American Institute of Physics.[389]

 This journal is © The Royal Society of Chemistry 2013

Published on 30 April 2013. Downloaded by University of Tennessee at Knoxville on 10/06/2016 20:55:54.

as eqn (24) by calculation of various rate equations shown in eqn (22) and (23):[389]

$$G_c + k_{PC}\left(\sum{}^{i}\mathrm{PP}\right) - k_{CP}C = 0 \tag{22}$$

$$\frac{1}{4}k_{CP}C + k_{HF_0}\left({}^3\mathrm{PP}_0 - {}^1\mathrm{PP}\right) + k_{HF}\left({}^3\mathrm{PP}_+ - {}^1\mathrm{PP}\right) + k_{HF}\left({}^3\mathrm{PP}_- - {}^1\mathrm{PP}\right) - (k_{PC} + k_{PS})\,{}^1\mathrm{PP} = 0 \tag{23}$$

$$\frac{\Delta I}{I} = \eta_1 \frac{\frac{k_{PC}}{k_{PT}}(1-r)^2}{\left(4\frac{k_{PC}}{k_{PT}} + r + 3\right)\left[\frac{k_{PC}}{k_{PT}}(r+3) + 2(r+1)\right]} \tag{24}$$

where C represents free charges, G_c is the generation rate for C, k_{PC} is the transition rate constant from ^{i}PP to C, k_{CP} is the opposite transition process rate constant, k_{HF_0} and k_{HF} is the transition rate constant from ^{1}PP to $^3\mathrm{PP}_0$ and to $^3\mathrm{PP}_+$ or $^3\mathrm{PP}_-$, respectively (^{1}PP is isoenergetic to $^3\mathrm{PP}_0$), k_{PS} and k_{PT} are the transition rate constants from ^{1}PP to singlet excitons and $^3\mathrm{PP}_0$, $^3\mathrm{PP}_+$, $^3\mathrm{PP}_-$ to triplet excitons, respectively, $r \equiv k_{PS}/k_{PT}$, and η_1 is the fraction of the injected carriers which form the electron–hole pairs. Although, from eqn (24), the transition rate change caused by adding the magnetic field is known to cause the current change, $\Delta I/I$ is always positive in this model, it cannot explain the phenomenon that both positive and negative GMR effects are observed.

6.2 Electron–hole (e–h) recombination model

Prigodin *et al.*[391] have investigated the large MR mechanism to explain the anomalous MR in the thin films of OSC Alq_3 doped with the complex of 2,3,7,8,12,13,17,18-octaethyl-21*H*,23*H*-porphine platinum (PtOEP) and tris(2-phenylpyridine)iridium ($Ir(ppy)_3$) based on the charge transport being electron–hole (e–h) recombination in the chemical reaction with radicals as "chemically induced dynamic spin polarization". The process of e–h recombination includes formation of correlated e–h pairs and annihilation of e–h pairs with different spin interconversion of e–h pairs.[391] Of the parameters influencing the electrical current density, J, the e–h recombination rate (β) is suggested to be the most sensitive to changes in an applied magnetic field H. Assuming that the relative modulation of $\beta(H)$ and the respective modulation of $J(\beta)$ with the magnetic field are small, the MR can be described as eqn (25):[391]

$$\mathrm{MR} = \frac{J(0)}{J(H)} - 1 = c\left[1 - \frac{\beta(0)}{\beta(H)}\right] \tag{25a}$$

$$c = -\left(\frac{\beta}{J(\beta)}\right)\frac{\mathrm{d}J}{\mathrm{d}\beta} = -\left.\frac{\mathrm{d}\ln J}{\mathrm{d}\ln\beta}\right|_{H=0} \tag{25b}$$

where the factor c is dependent on β. For the space-charge-limited transport, Parmenter and Ruppel[392] have found the exact solution as described by eqn (26):

$$J = \left(\frac{3}{2}\right)\left[\frac{\pi e\varepsilon_0\varepsilon_r\mu_p\mu_n(\mu_p + \mu_n)}{\beta}\right]^{1/2}\left(\frac{V^2}{L^3}\right) \tag{26}$$

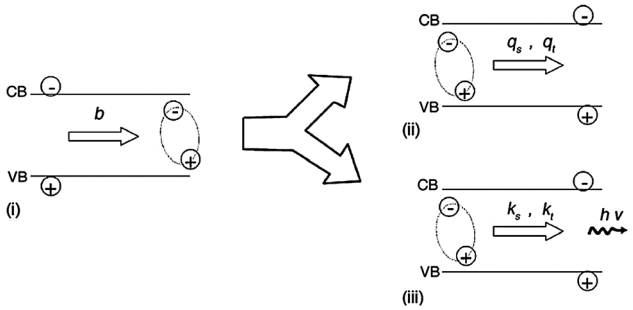

Fig. 51 Schematic illustration of the process of (i) formation of intermediate electron–hole pairs and, the subsequent processes of (ii) dissociation or (iii) recombination. Emission of a photon or a phonon of energy $h\nu$ resulted from recombination. Reprinted with permission from Elsevier.[391]

where, μ_n and μ_p represent the effective mobilities of the injected electrons and holes, respectively. V is the voltage drop across the semiconductor film of thickness L, ε_0 stands for the dielectric constant of vacuum and ε_r is the relative dielectric constant of the semiconductor.

The e–h recombination process was claimed to pass through an intermediate state, which represents a coupled state of electrons and holes; in the following, b is assumed to be the corresponding formation rate constant of the e–h pair forms.[391] The e–h pair may either dissociate or recombine. The rate constants of recombination for singlet and triplet e–h pairs are k_s and k_t, respectively, which depends on their corresponding spin state, while q_s and q_t represent the rate of dissociation for the singlet and the triplet state, respectively, Fig. 51. The β in eqn (25) and (26) can be described as eqn (27):

$$\beta = b\left[\left(\frac{1}{4}\right)\frac{k_s}{k_s + q_s} + \left(\frac{3}{4}\right)\frac{k_t}{k_t + q_t}\right] \tag{27}$$

The coefficients for each term in square-brackets of eqn (27) are the relative ratio between singlets and triplets for an uncorrelated distribution of spins for injected electrons and holes. All the four spin states are expected to stay equally occupied at any time, and the β is defined by eqn (28):[391]

$$\beta(0) = \frac{b(k_s + 3k_t)}{k_s + 3k_t + q_s + 3q_t} \tag{28}$$

For the strong magnetic fields, the β is expressed by eqn (29):[391]

$$\beta(\infty) = b\left[\left(\frac{1}{2}\right)\frac{k_s + k_t}{k_s + k_t + q_s + q_t} + \left(\frac{1}{2}\right)\frac{k_t}{k_t + q_t}\right] \tag{29}$$

substituting eqn (28) and (29) into eqn (25) and (26) and rearranging, the saturation magnetoresistance, MR_{sat}, is defined by eqn (30):

$$\mathrm{MR}_{sat} = -\left(\frac{1}{2}\right)\frac{(k_s + q_s - k_t - q_t)(k_s q_t - k_t q_s)}{(k_t + q_t)(k_s + 3k_t + q_s + 3q_t)(k_s + k_t + q_s + q_t)} \tag{30}$$

Published on 30 April 2013. Downloaded by University of Tennessee at Knoxville on 10/06/2016 20:55:54.

when $k_s = k_t = k$, eqn (30) becomes eqn (31):

$$MR_{sat} = \left(\frac{1}{2}\right)\frac{k(q_s - q_t)^2}{(k + q_t)(4k + q_s + 3q_t)(2k + q_s + q_t)} \quad (31)$$

The positive MR in eqn (31) illustrates that the recombination rates of the singlet and the triplet are equal and the dissociation rates are different. The splitting of the triplet channels by magnetic fields results in a slow e–h recombination.

With an assumption that the dissociation rate constant does not show strong spin dependence and the fastest process is the singlet recombination, eqn (31) is simplified to be:

$$MR_{sat} = -\left(\frac{1}{2}\right)\frac{q_t}{k_t + q_t} \quad (32)$$

eqn (32) shows a negative magnetoresistance.

6.3 Bipolaron model

The former two models are discussed based on the exciton pairs and polarons of electron–hole pairs, however, when exploring the mechanism of GMR, the bipolaron (two positive or two negative charges combined together) is another kind of mechanism being studied.[393] In the bipolaron model, the magnetic field reduces the rate of bipolaron formation from the e–e or h–h pairs, which can lead to an increase or decrease of the current.[388] This model is applied to explore the MR in disordered π-conjugated materials based on hopping of polarons and bipolaron formation in the presence of the random hyperfine fields (the hyperfine field is an important probe of the magnetism of the solids[394]) of the hydrogen nuclei and an external magnetic field. The basic idea of this model is that bipolarons only occur as spin singlets and two polarons having the same spin component along a common quantization axis, which have zero singlet probability, cannot form a bipolaron. In this model, the probability of bipolaron formation is presented by eqn (33):[395]

$$p_\beta = \frac{r_{e\to\alpha}}{r_{\beta\to e}} f(H) p \quad (33)$$

where $f(H) = [P_P P_{AP} + 1/(4b)]/[P_P P_{AP} + 1/(2b) + 1/b^2]$, $b \equiv r_{\alpha\to\beta}/r_{\alpha\to e}$ is the branching ratio, $P_{AP} r_{\alpha\to\beta}$ and $P_P r_{\alpha\to\beta}$ are the rates of a polaron hopping to the β site from an α site next to it, $r_{e\to\alpha}$ is the rate of a polaron hopping from the environment to α, $r_{\beta\to e}$ is the rate of a polaron hopping from β to the environment, p is a measure for the average number of polarons in the environment, $p = \frac{1}{4} - S_i \cdot S_j/\hbar^2$ is the singlet probability, H is the magnetic field, when $H = 0$, $P = 1/4$, and for large field $P_P = 0$ and $P_{AP} = 1/2$, $S_{i,j}$ are the classical spin vectors pointing along $H_{total,i,j}$, and $\hbar = h/2\pi$, where h is Planck's constant.

The relationship between $f(H)$ and the experimental result is reproduced by simulation of the model. In addition, this mechanism can explain both negative and positive MR by varying model parameters. In the bipolaron model, the positive MR (or negative magnetoconductance) is associated with the blocking of electron transport through bipolaron states; the negative MR (or positive magnetoconductance) is caused by the increase in polaron population at the expense of bipolarons with increasing H.

6.4 Forward interference model and wave-function shrinkage model

The forward interference model and wave-function shrinkage model are often used to describe the MR of highly disorderedly, localized systems in the VRH regime.[396] In the forward interference model, the effect of interference among various hopping paths was considered, where the hopping paths include sequence of scattering of tunneling electrons by the impurities located within a cigar-shaped domain of length R_h (hopping distance) and width $(R_h a_0)^{1/2}$ (a_0 is the localization length) between hopping sites. The anisotropy of the magnetic susceptibility is commonly described by comparing susceptibility values in three mutually perpendicular directions: K_1 = maximum susceptibility; K_2 = intermediate susceptibility; K_3 = minimum susceptibility, which can express the magnetic susceptibility ellipsoid. When $K_1 = K_2 = K_3$, the ellipsoid is spherical; when $K_1 \approx K_2$, but $K_2 > K_3$, the ellipsoid is oblate (flattened); when $K_1 > K_2$, the ellipsoid is prolate (cigar-shaped).[397] After averaging numerically the logarithm of the conductivity over many different possible paths in the presence of a magnetic field, a linear negative MR was obtained in the low magnetic field limit. Later on, a quadratic negative MR at small magnetic fields, which saturates at high magnetic fields, was observed.[380] Actually, the linear MR was often seen in the low magnetic field and the quadratic MR was only occasionally observed in some samples at a very weak magnetic field. Thus, the resistance ratio caused by interference effects, $r = R(H,T)/R(0,T)$, is expressed approximately by empirical equation(34) (which neglects the quadratic term in H):[398]

$$r_{forward} \approx 1/\{1 + C_{sat}[H/H_{sat}]/[1 + H/H_{sat}]\} \quad (34)$$

where the fitting C_{sat} is the saturation constant and the fitting H_{sat} is the effective saturation magnetic field. For the Mott VRH case, they are given by eqn (35):[396]

$$H_{sat} \approx 0.7\left(\frac{8}{3}\right)^{3/2}\left(\frac{1}{a_0^2}\right)\left(\frac{h}{e}\right)\left(\frac{T}{T_{Mott}}\right)^{3/8} \quad (35)$$

where h is Planck's constant, e is the electron charge and T_{Mott} is the Mott characteristic temperature. In the low-field limit, eqn (34) becomes eqn (36):

$$r_{forward} \approx 1 - C_{sat}[H/H_{sat}] \quad (36)$$

i.e., eqn (37):

$$\frac{\Delta R(H,T)}{R(0,T)} = \frac{R(H,T) - R(0,T)}{R(0,T)} \approx -C_{sat}[H/H_{sat}] \quad (37)$$

In the wave-function shrinkage model, the contraction of the electronic wave function at impurity centers in the magnetic field leads to a reduction in the hopping probability between two sites causing a positive MR. The r is described as eqn (38):[396]

$$r_{wave} = \exp\{\xi_C(0)[\xi_C(H)/\xi_C(0) - 1]\} \quad (38)$$

where $\xi_C(0) = (T_{Mott}/T)^{1/4}$ for the 3-D Mott VRH case, $\xi_C(H)/\xi_C(0)$ is the normalized hopping probability parameter as a function

 This journal is © The Royal Society of Chemistry 2013

Published on 30 April 2013. Downloaded by University of Tennessee at Knoxville on 10/06/2016 20:55:54.

of H/P_c for Mott. P_c is the fitting parameter given by eqn (39) for the Mott VRH case:

$$P_c = 6\hbar/[ea_0^2(T_{Mott}/T)^{1/4}] \quad (39)$$

where e is the electron charge, $\hbar = h/2\pi$, h is Planck's constant and T_{Mott} is the Mott characteristic temperature. In the low-field limit, eqn (38) is simplified to eqn (40):

$$r_{wave} \approx 1 + t_2\frac{H^2}{P_C^2}\left(\frac{T_{Mott}}{T}\right)^{1/4} \quad (40)$$

i.e., eqn (41):

$$\frac{\Delta R(H,T)}{R(0,T)} \approx t_2\frac{H^2}{P_C^2}\left(\frac{T_{Mott}}{T}\right)^{1/4} \quad (41)$$

where the numerical constant $t_2 \approx 5/2016$.

These two theoretical models are often used together to explain the MR transition from negative at a low field to positive at a high field. Then the total MR ratio should be written as eqn (42):

$$r_{total} = \exp\{\xi_C(0)[\xi_C(H)/\xi_C(0) - 1]\} + 1/\{1 + C_{sat}[H/H_{sat}]/[1 + H/H_{sat}]\} - 1 \quad (42)$$

The last term, -1, is to assure that the r_{total} is equal to 1 when $H = 0$. These two models can be used in both metallic systems[396] and non-metallic systems.[399]

7. Applications of GMR in the molecular systems

Recently, the GMR effect has been used in many technological fields and commercial products including read heads in hard disks and magnetic sensors.[35] Compared with the inorganic GMR devices, the GMR effect in molecular devices has attracted considerable attention in the last decade due to the fundamental advantages of these materials including low production cost, light weight, large area coverage, relatively easy processability, mechanical flexibility and compatibility with plastic substrates.[176,400] Molecular devices with the GMR effect have great potential to be used in the near future in magnetic read heads (measuring the magnetic fringe field created by the magnetized regions on the tracks (bit)), MRAM,[401] magnetic sensors[21] and may replace inorganic materials in these flexible and inexpensive niche applications.[402] However, there have been only few applications based on the non-metallic molecular devices so far due to the novelty of this field.

For example, a schematic structure of the memory device composed of a highly spin-polarized LSMO (bottom) and Co (top) sandwiched with an organic layer (Alq_3) is depicted in Fig. 52a.[401] The use of this structure in the memory device is particularly noteworthy. Fig. 52b shows the switching effect of this memory device. The top panel is for the voltage and the bottom panel is for the current of this device. In the memory process, the writing (W), erasing (E) and reading (R) voltages were set to 2, -2 and 1.25 V, respectively. The current reached a value of 20 mA (high conductance, "ON") according to the writing (W) voltage of 2 V and maintained during the subsequent reading (R) voltage of 1.25 V, then remained in the low conductance value, "OFF", for the new reading process after the erasing (E) voltage of -2 V. The experiment confirmed that this cycle could be repeated for up to 6000 s (about 600 cycles) without any degradation sign in the effect.

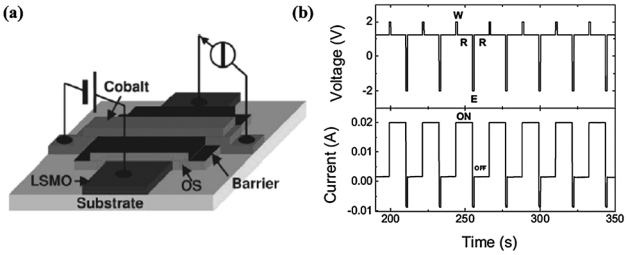

Fig. 52 (a) Scheme of the memory device and (b) the switching effect for this memory device. Reprint permission from John Wiley and Sons.[401]

Graphene nanoribbon-based spin transistor devices have also been proposed in the GMR spintronic applications.[403–405] Fig. 53 shows the schematic configuration of two terminal zigzag graphene nanoribbon (ZGNR) based-spin diodes.[406] An external magnetic field is employed to manipulate the magnetization of the left and the right ZGNR electrode (M_L and M_R). M_L and M_R can be set at 1 (magnetization along the $+y$ direction), 0 (nonmagnetic), or -1 (magnetization along the $-y$ direction). The current flow along the z or the $-z$ direction, which corresponds to a positive or negative applied bias voltage, respectively, is denoted as the + or − direction. This device functions as a bias-controlled bipolar spin diode, where only spin-down electrons are allowed to pass through the device when a positive bias is applied and only spin-up electrons transport through the device under a negative bias.

GMR was observed in organic spin valves, composed of π-conjugated polymer, poly(dioctyloxy)phenylvinylene (DOO-PPV),

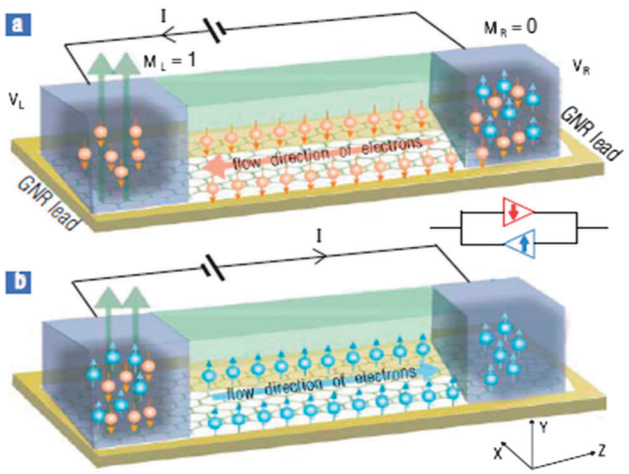

Fig. 53 Schematic of ZGNRs-based bipolar spin diodes of (a) under a positive bias where only spin-down electrons transport through devices and (b) under a negative bias where only spin-up electrons are allowed to transport from left to right. The inset represents the circuit diagram of this bias-controlled bipolar spin diode. Reprinted with permission from the American Physical Society.[406]

Published on 30 April 2013. Downloaded by University of Tennessee at Knoxville on 10/06/2016 20:55:54.

at T = 10 K and V = 10 mV, and the MR can reach almost 20% with a sharp GMR response which indicates the potential applications in the room temperature operation field.[407] An organic GMR of about 10% observed in the research of poly(dialkylfluorene) at a magnetic field of 10 mT at room temperature shows potential to be applied in MRAM and spin OLEDs fields.[408] Magnetic molecules, *i.e.*, polyoxometalate, $[PMo_{12}O_{40}(VO)_2]^{q-}$, which consist of a central mixed-valence core based on the $[PMo_{12}O_{40}]$ Keggin unit and capped by two vanadyl groups containing two localized spins, have promising potentials for quantum computing.[409]

8. Conclusion, challenges and perspectives

In this paper, the classifications of the MR effects, electrical conduction mechanisms in the materials without and with magnetic field, and the up-to-date knowledge of the GMR effect in the molecular systems including Alq3, rubrene, CNTs, graphene, conductive polymers and other systems have been reviewed. The mechanisms of OMAR effect including excitonic pair model, electron–hole recombination model, bipolaron model, forward interference model and wave-function shrinkage model are discussed as well. The possible applications of molecular GMR systems in memory devices, spin transistors, spin OLEDs and quantum computing have been described. A comprehensive summary of the GMR effect in the molecular systems with relevant literature references has been presented for the first time.

However, there are still challenges for wide potential applications of these molecular GMR systems, especially for the OMAR systems. The observed GMR is still controversial and the understanding of spin injection and transport in the OSC layer is still not clear due to the lack of comprehensive device characteristic study.[175] In addition, the temperature dependent GMR effect in the organic system is a crucial and puzzling problem.[11] Since the GMR in the organic system is often obtained at low temperatures (GMR decreases with increasing temperature),[121,302,410,411] the room temperature GMR signal is still too weak to be useful for the practical applications. Thus it is still difficult to achieve room temperature operation. To obtain the high value of GMR at room temperature is the challenge for the current researchers. The physical process of the spintronic devices is strongly controlled by the interface properties, thus a considerable improvement of the interfaces for the multilayer device to achieve the efficient spin injection is a better way to solve this problem. Meanwhile, the development of a new single molecular system to make the spin injection and transport easier is another trend for the future. Even though the molecular systems with suitable performance have been realized on the lab-scale, to find large-scale practical use remains the most challenging for the current researchers. Another potential candidate is the conductive polymer based nanocomposites, which have shown strong enough MR signals comparable to the metallic counterparts. The polymer nanocomposites with a larger signal and higher sensitivity especially at a low magnetic field need the knowledge of hosting conductive polymer materials and nanofillers including both the semiconductive oxides and FM metals with fairly high magnetization. Their synergistic interactions upon the electron transport within the hybrid systems are demanding for GMR design as well.

Acknowledgements

This work is financially supported by NSF – Nanomanufacturing under the EAGER program (CMMI 13-14486), Nanoscale Interdisciplinary Research Team and Materials Processing and Manufacturing (CMMI 10-30755) and Chemical and Biological Separations under the EAGER program (CBET 11-37441). H. Gu acknowledges the support from China Scholarship Council (CSC) program.

References

1 B. Hu and Y. Wu, *Nat. Mater.*, 2007, **6**, 985–991.
2 Z. Guo, S. Wei, D. Cocke and D. Zhang, in *Nanostructured Conductive Polymers*, ed. A. Eftekhari, John Wiley and Sons, 2010, pp. 503–529.
3 F. Muñoz-Rojas, J. Fernández-Rossier and J. J. Palacios, *Phys. Rev. Lett.*, 2009, **102**, 136810.
4 L. Bogani and W. Wernsdorfer, *Nat. Mater.*, 2008, **7**, 179–186.
5 D. V. Bulaev, B. r. Trauzettel and D. Loss, *Phys. Rev. B: Condens. Matter Mater. Phys.*, 2008, **77**, 235301.
6 V. Dediu, M. Murgia, F. C. Matacotta, C. Taliani and S. Barbanera, *Solid State Commun.*, 2002, **122**, 181–184.
7 Z. H. Xiong, D. Wu, Z. V. Vardeny and J. Shi, *Nature*, 2004, **427**, 821–824.
8 H. Gu, Y. Huang, X. Zhang, Q. Wang, J. Zhu, L. Shao, N. Haldolaarachchige, D. P. Young, S. Wei and Z. Guo, *Polymer*, 2012, **53**, 801–809.
9 J. Zhu, H. Gu, Z. Luo, N. Haldolaarachige, D. P. Young, S. Wei and Z. Guo, *Langmuir*, 2012, **28**, 10246–10255.
10 W. Wang, M. Yu, Y. Chen and J. Tang, *J. Appl. Phys.*, 2006, **99**, 08J108.
11 F. L. Bloom, M. Kemerink, W. Wagemans and B. Koopmans, *Phys. Rev. Lett.*, 2009, **103**, 066601.
12 T. D. Nguyen, Y. Sheng, J. Rybicki, G. Veeraraghavan and M. Wohlgenannt, *J. Mater. Chem.*, 2007, **17**, 1995–2001.
13 F. L. Bloom, W. Wagemans, M. Kemerink and B. Koopmans, *Phys. Rev. Lett.*, 2007, **99**, 257201.
14 Ö. Mermer, G. Veeraraghavan, T. L. Francis, Y. Sheng, D. T. Nguyen, M. Wohlgenannt, A. Köhler, M. K. Al-Suti and M. S. Khan, *Phys. Rev. B: Condens. Matter Mater. Phys.*, 2005, **72**, 205202.
15 Z. Guo, S. Park, H. T. Hahn, S. Wei, M. Moldovan, A. B. Karki and D. P. Young, *Appl. Phys. Lett.*, 2007, **90**, 053111.
16 P. A. Grünberg, *Rev. Mod. Phys.*, 2008, **80**, 1531–1540.
17 Z. Guo, H. T. Hahn, H. Lin, A. B. Karki and D. P. Young, *J. Appl. Phys.*, 2008, **104**, 014314.

 This journal is © The Royal Society of Chemistry 2013

Published on 30 April 2013. Downloaded by University of Tennessee at Knoxville on 10/06/2016 20:55:54.

18 W. J. Gallagher and S. S. P. Parkin, *IBM J. Res. Dev.*, 2006, **50**, 5–23.
19 G. W. Burr, B. N. Kurdi, J. C. Scott, C. H. Lam, K. Gopalakrishnan and R. S. Shenoy, *IBM J. Res. Dev.*, 2008, **52**, 449–464.
20 R. F. Freitas and W. W. Wilcke, *IBM J. Res. Dev.*, 2008, **52**, 439–447.
21 D. L. Graham, H. A. Ferreira and P. P. Freitas, *Trends Biotechnol.*, 2004, **22**, 455–462.
22 R. S. Gaster, D. A. Hall, C. H. Nielsen, S. J. Osterfeld, H. Yu, K. E. Mach, R. J. Wilson, B. Murmann, J. C. Liao and S. S. Gambhir, *Nat. Med.*, 2009, **15**, 1327–1332.
23 B. De Boer, J. Kahlman, T. Jansen, H. Duric and J. Veen, *Biosens. Bioelectron.*, 2007, **22**, 2366–2370.
24 Y. Li, B. Srinivasan, Y. Jing, X. Yao, M. A. Hugger, J.-P. Wang and C. Xing, *J. Am. Chem. Soc.*, 2010, **132**, 4388–4392.
25 I. Malajovich, J. J. Berry, N. Samarth and D. D. Awschalom, *Nature*, 2001, **411**, 770–772.
26 G. A. Prinz, *Science*, 1998, **282**, 1660–1663.
27 A. Brataas, G. E. W. Bauer and P. J. Kelly, *Phys. Rep.*, 2006, **427**, 157–255.
28 C. Binek and B. Doudin, *J. Phys.: Condens. Matter*, 2005, **17**, L39–L44.
29 F. Pulizzi, *Nat. Mater.*, 2012, **11**, 367.
30 M. N. Baibich, J. M. Broto, A. Fert, F. N. Van Dau, F. Petroff, P. Etienne, G. Creuzet, A. Friederich and J. Chazelas, *Phys. Rev. Lett.*, 1988, **61**, 2472–2475.
31 G. Binasch, P. Grünberg, F. Saurenbach and W. Zinn, *Phys. Rev. B: Condens. Matter Mater. Phys.*, 1989, **39**, 4828–4830.
32 S. A. Wolf, D. D. Awschalom, R. A. Buhrman, J. M. Daughton, S. von Molnár, M. L. Roukes, A. Y. Chtchelkanova and D. M. Treger, *Science*, 2001, **294**, 1488–1495.
33 R. E. Camley and R. L. Stamps, *J. Phys.: Condens. Matter*, 1993, **5**, 3727–3786.
34 A. N. Chantis, K. D. Belashchenko, E. Y. Tsymbal and I. V. Sus, *Mod. Phys. Lett. B*, 2008, **22**, 2529–2551.
35 M. T. Sarah, *J. Phys. D: Appl. Phys.*, 2008, **41**, 093001.
36 S. Karmakar, S. Kumar, R. Rinaldi and G. Maruccio, *J. Phys.: Conf. Ser.*, 2011, **292**, 012002.
37 R. Jansen, *Nat. Mater.*, 2012, **11**, 400–408.
38 J. G. Zhao, L. X. Yang, Y. Yu, F. Y. Li, R. C. Yu, Z. Fang, L. C. Chen and C. Q. Jin, *J. Appl. Phys.*, 2008, **103**, 103706.
39 A. Gerber, I. Kishon, I. Y. Korenblit, O. Riss, A. Segal, M. Karpovski and B. Raquet, *Phys. Rev. Lett.*, 2007, **99**, 027201.
40 G. Beck, C. Korte, J. Janek, F. Gruhl and M. Kreutzbruck, *J. Appl. Phys.*, 2004, **96**, 5619–5624.
41 G. Beck and J. Jürgen, *Physica B*, 2001, **308**, 1086–1089.
42 T. Fujita, H. Okada, K. Koyama, K. Watanabe, S. Maekawa and M. W. Chen, *Phys. Rev. Lett.*, 2008, **101**, 166601.
43 W. Shim, J. Ham, K. Lee, W. Y. Jeung, M. Johnson and W. Lee, *Nano Lett.*, 2008, **9**, 18–22.
44 N. Marcano, S. Sangiao, M. Plaza, L. Perez, A. F. Pacheco, R. Cordoba, M. C. Sanchez, L. Morellon, M. R. Ibarra and J. M. De Teresa, *Appl. Phys. Lett.*, 2010, **96**, 082110.
45 Y. Hwang, J. Choi, S. C. Hong, S. Cho, S. Han, K. Shin and M. Jung, *Phys. Rev. B: Condens. Matter Mater. Phys.*, 2009, **79**, 045309.
46 E. Cimpoiasu, V. Sandu, G. A. Levin, A. Simpson and D. Lashmore, *J. Appl. Phys.*, 2012, **111**, 123721.
47 W. Thomson, *Proc. R. Soc. London*, 1856, **8**, 546–550.
48 T. McGuire and R. Potter, *IEEE Trans. Magn.*, 1975, **11**, 1018–1038.
49 R. P. van Gorkom, J. Caro, T. M. Klapwijk and S. Radelaar, *Phys. Rev. B: Condens. Matter Mater. Phys.*, 2001, **63**, 134432.
50 T. G. S. M. Rijks, R. Coehoorn, M. J. M. Jong and W. J. M. Jonge, *Phys. Rev. B: Condens. Matter Mater. Phys.*, 1995, **51**, 283–291.
51 J. Velev, R. F. Sabirianov, S. S. Jaswal and E. Y. Tsymbal, *Phys. Rev. Lett.*, 2005, **94**, 127203.
52 R. I. Potter, *Phys. Rev. B: Solid State*, 1974, **10**, 4626–4636.
53 S. J. Papadakis, E. P. De Poortere, M. Shayegan and R. Winkler, *Phys. Rev. Lett.*, 2000, **84**, 5592–5595.
54 A. W. Rushforth, K. Výborný, C. S. King, K. W. Edmonds, R. P. Campion, C. T. Foxon, J. Wunderlich, A. C. Irvine, P. Vašek, V. Novák, K. Olejník, J. Sinova, T. Jungwirth and B. L. Gallagher, *Phys. Rev. Lett.*, 2007, **99**, 147207.
55 J. E. Wegrowe, D. Kelly, A. Franck, S. E. Gilbert and J. P. Ansermet, *Phys. Rev. Lett.*, 1999, **82**, 3681–3684.
56 K. D. D. Rathnayaka, D. G. Naugle, B. K. Cho and P. C. Canfield, *Phys. Rev. B: Condens. Matter Mater. Phys.*, 1996, **53**, 5688–5695.
57 L. Ding, J. Teng, Q. Zhan, C. Feng, M. Li, G. Han, L. Wang, G. Yu and S. Wang, *Appl. Phys. Lett.*, 2009, **94**, 162506.
58 S. F. Shi, K. I. Bolotin, F. Kuemmeth and D. C. Ralph, *Phys. Rev. B: Condens. Matter Mater. Phys.*, 2007, **76**, 184438.
59 S. Tumański, *Thin Film Magnetoresistive Sensors*, IoP, 2001.
60 S. Yuasa, T. Nagahama, A. Fukushima, Y. Suzuki and K. Ando, *Nat. Mater.*, 2004, **3**, 868–871.
61 L. Piraux, J. M. George, J. F. Despres, C. Leroy, E. Ferain, R. Legras, K. Ounadjela and A. Fert, *Appl. Phys. Lett.*, 1994, **65**, 2484–2486.
62 K. Inomata, K. Yusu and Y. Saito, *Phys. Rev. Lett.*, 1995, **74**, 1863–1866.
63 J. Zhang, M. Moldovan, D. P. Young and E. J. Podlaha, *J. Electrochem. Soc.*, 2005, **152**, C626–C630.
64 D. M. Davis, M. Moldovan, D. P. Young, M. Henk, X. Xie and E. J. Podlaha, *Electrochem. Solid-State Lett.*, 2006, **9**, C153–C155.
65 D. Davis, M. Zamanpour, M. Moldovan, D. Young and E. J. Podlaha, *J. Electrochem. Soc.*, 2010, **157**, D317–D322.
66 C. L. Chien, J. Q. Xiao and J. S. Jiang, *J. Appl. Phys.*, 1993, **73**, 5309–5314.
67 Z. Guo, S. Wei, S. Park, M. Moldovan, A. Karki, D. Young and H. T. Hahn, *Proc. SPIE*, 2007, **6526**, 65260U.
68 J. Q. Xiao, J. S. Jiang and C. L. Chien, *Phys. Rev. Lett.*, 1992, **68**, 3749–3752.

Published on 30 April 2013. Downloaded by University of Tennessee at Knoxville on 10/06/2016 20:55:54.

69 Z. Guo, M. Moldovan, D. P. Young, L. L. Henry and E. J. Podlaha, *Electrochem. Solid-State Lett.*, 2007, **10**, E31–E35.
70 D. Zhang, R. Chung, A. B. Karki, F. Li, D. P. Young and Z. Guo, *J. Phys. Chem. C*, 2009, **114**, 212–219.
71 Y. Sheng, T. D. Nguyen, G. Veeraraghavan, Ö. Mermer and M. Wohlgenannt, *Phys. Rev. B: Condens. Matter Mater. Phys.*, 2007, **75**, 035202.
72 C. D. Dimitrakopoulos and P. R. L. Malenfant, *Adv. Mater.*, 2002, **14**, 99–117.
73 H. Fukuzawa, H. Yuasa, S. Hashimoto, H. Iwasaki and Y. Tanaka, *Appl. Phys. Lett.*, 2005, **87**, 082507.
74 B. Dieny, V. S. Speriosu, S. Metin, S. S. P. Parkin, B. A. Gurney, P. Baumgart and D. R. Wilhoit, *J. Appl. Phys.*, 1991, **69**, 4774–4779.
75 C. Chappert, A. Fert and F. N. Van Dau, *Nat. Mater.*, 2007, **6**, 813–823.
76 R. E. Camley and J. Barnaś, *Phys. Rev. Lett.*, 1989, **63**, 664–667.
77 P. M. Levy, S. Zhang and A. Fert, *Phys. Rev. Lett.*, 1990, **65**, 1643–1646.
78 K. J. Dempsey, D. Ciudad and C. H. Marrows, *Philos. Trans. R. Soc., A*, 2011, **369**, 3150–3174.
79 L. Berger, *Phys. Rev. B: Condens. Matter Mater. Phys.*, 1996, **54**, 9353–9358.
80 I. Žutić, J. Fabian and S. Das Sarma, *Rev. Mod. Phys.*, 2004, **76**, 323–410.
81 B. L. Johnson and R. E. Camley, *Phys. Rev. B: Condens. Matter Mater. Phys.*, 1991, **44**, 9997–10002.
82 Y. Yang, J. G. Zhu, R. M. White and M. Asheghi, *J. Appl. Phys.*, 2006, **99**, 063703.
83 S. Sanvito, *Chem. Soc. Rev.*, 2011, **40**, 3336–3355.
84 B. Dieny, V. S. Speriosu, S. S. P. Parkin, B. A. Gurney, D. R. Wilhoit and D. Mauri, *Phys. Rev. B: Condens. Matter Mater. Phys.*, 1991, **43**, 1297–1300.
85 D. C. Worledge and T. H. Geballe, *J. Appl. Phys.*, 2000, **88**, 5277–5279.
86 A. Brataas, Y. Tserkovnyak, G. E. W. Bauer and B. I. Halperin, *Phys. Rev. B: Condens. Matter Mater. Phys.*, 2002, **66**, 060404.
87 R. L. White, *IEEE Trans. Magn.*, 1992, **28**, 2482–2487.
88 R. H. Yu, X. X. Zhang, J. Tejada, M. Knobel, P. Tiberto and P. Allia, *J. Appl. Phys.*, 1995, **78**, 392–397.
89 W. Wang, H. Sukegawa, R. Shan, S. Mitani and K. Inomata, *Appl. Phys. Lett.*, 2009, **95**, 182502.
90 C. Giebeler, D. J. Adelerhof, A. E. T. Kuiper, J. B. A. van Zon, D. Oelgeschläger and G. Schulz, *Sens. Actuators, A*, 2001, **91**, 16–20.
91 J. M. Daughton, *J. Magn. Magn. Mater.*, 1999, **192**, 334–342.
92 A. Moser, K. Takano, D. T. Margulies, M. Albrecht, Y. Sonobe, Y. Ikeda, S. H. Sun and E. E. Fullerton, *J. Phys. D: Appl. Phys.*, 2002, **35**, R157–R167.
93 M. J. Carey, S. Maat, S. Chandrashekariaih, J. A. Katine, W. Chen, B. York and J. R. Childress, *J. Appl. Phys.*, 2011, **109**, 093912.
94 M. Pannetier-Lecoeur, L. Parkkonen, N. Sergeeva-Chollet, H. Polovy, C. Fermon and C. Fowley, *Appl. Phys. Lett.*, 2011, **98**, 153705.
95 R. S. Gaster, L. Xu, S.-J. Han, R. J. Wilson, D. A. Hall, S. J. Osterfeld, H. Yu and S. X. Wang, *Nat. Nanostruct.*, 2011, **6**, 314–320.
96 D. A. Hall, R. S. Gaster, T. Lin, S. J. Osterfeld, S. Han, B. Murmann and S. X. Wang, *Biosens. Bioelectron.*, 2010, **25**, 2051–2057.
97 R. S. Gaster, D. A. Hall and S. X. Wang, *Nano lett.*, 2010, **11**, 2579–2583.
98 W.-J. Kim, B. K. Kim, A. Kim, C. Huh, C. S. Ah, K.-H. Kim, J. Hong, S. H. Park, S. Song, J. Song and G. Y. Sung, *Anal. Chem.*, 2010, **82**, 9686–9693.
99 L. Xu, H. Yu, M. S. Akhras, S.-J. Han, S. Osterfeld, R. L. White, N. Pourmand and S. X. Wang, *Biosens. Bioelectron.*, 2008, **24**, 99–103.
100 B. Srinivasan, Y. Li, Y. Jing, Y. Xu, X. Yao, C. Xing and J.-P. Wang, *Angew. Chem., Int. Ed.*, 2009, **48**, 2764–2767.
101 M. Koets, T. van der Wijk, J. T. W. M. van Eemeren, A. van Amerongen and M. W. J. Prins, *Biosens. Bioelectron.*, 2009, **24**, 1893–1898.
102 R. L. Edelstein, C. R. Tamanaha, P. E. Sheehan, M. M. Miller, D. R. Baselt, L. J. Whitman and R. J. Colton, *Biosens. Bioelectron.*, 2000, **14**, 805–813.
103 D. A. Hall, R. S. Gaster, S. J. Osterfeld, B. Murmann and S. X. Wang, *Biosens. Bioelectron.*, 2010, **25**, 2177–2181.
104 M. Mujika, S. Arana, E. Castaño, M. Tijero, R. Vilares, J. M. Ruano-López, A. Cruz, L. Sainz and J. Berganza, *Biosens. Bioelectron.*, 2009, **24**, 1253–1258.
105 M. D. Michelena, W. Oelschlägel, I. Arruego, R. P. Del Real, J. A. D. Mateos and J. M. Merayo, *J. Appl. Phys.*, 2008, **103**, 07E912.
106 I. Mönch, D. Makarov, R. Koseva, L. Baraban, D. Karnaushenko, C. Kaiser, K. F. Arndt and O. G. Schmidt, *ACS Nano*, 2011, **5**, 7436–7442.
107 I. Bakonyi and L. Péter, *Prog. Mater. Sci.*, 2010, **55**, 107–245.
108 M. M. Maqableh, X. Huang, S. Y. Sung, K. S. M. Reddy, G. Norby, R. H. Victora and B. J. H. Stadler, *Nano Lett.*, 2012, **12**, 4102–4109.
109 S. Yoon, Y. Jang, C. Nam, S. Lee, J. Kwon, K. Na, K. Lee and B. K. Cho, *J. Appl. Phys.*, 2012, **111**, 07E504.
110 D. Karnaushenko, D. Makarov, C. Yan, R. Streubel and O. G. Schmidt, *Adv. Mater.*, 2012, **24**, 4518–4522.
111 T. Ogasawara, H. Kuwatsuka, T. Hasama and H. Ishikawa, *Appl. Phys. Lett.*, 2012, **100**, 251112.
112 M. Julliere, *Phys. Lett. A*, 1975, **54**, 225–226.
113 T. Miyazaki and N. Tezuka, *J. Magn. Magn. Mater.*, 1995, **139**, L231–L234.
114 J. S. Moodera, L. R. Kinder, T. M. Wong and R. Meservey, *Phys. Rev. Lett.*, 1995, **74**, 3273–3276.
115 W. Butler, X. G. Zhang, T. Schulthess and J. MacLaren, *Phys. Rev. B: Condens. Matter Mater. Phys.*, 2001, **63**, 054416.

 This journal is © The Royal Society of Chemistry 2013

Published on 30 April 2013. Downloaded by University of Tennessee at Knoxville on 10/06/2016 20:55:54.

116 S. S. P. Parkin, C. Kaiser, A. Panchula, P. M. Rice, B. Hughes, M. Samant and S. H. Yang, *Nat. Mater.*, 2004, **3**, 862–867.
117 M. Bowen, V. Cros, F. Petroff, A. Fert, J. Costa-Kramer, J. Anguita, A. Cebollada, F. Briones, J. de Teresa and L. Morellon, *Appl. Phys. Lett.*, 2001, **79**, 1655–1657.
118 S. Yuasa, A. Fukushima, H. Kubota, Y. Suzuki and K. Ando, *Appl. Phys. Lett.*, 2006, **89**, 042505.
119 S. Ikeda, J. Hayakawa, Y. Ashizawa, Y. M. Lee, K. Miura, H. Hasegawa, M. Tsunoda, F. Matsukura and H. Ohno, *Appl. Phys. Lett.*, 2008, **93**, 082508.
120 H. Mehrez, J. Taylor, H. Guo, J. Wang and C. Roland, *Phys. Rev. Lett.*, 2000, **84**, 2682–2685.
121 T. S. Santos, J. S. Lee, P. Migdal, I. C. Lekshmi, B. Satpati and J. S. Moodera, *Phys. Rev. Lett.*, 2007, **98**, 016601.
122 S. Ikeda, K. Miura, H. Yamamoto, K. Mizunuma, H. Gan, M. Endo, S. Kanai, J. Hayakawa, F. Matsukura and H. Ohno, *Nat. Mater.*, 2010, **9**, 721–724.
123 D. Waldron, P. Haney, B. Larade, A. MacDonald and H. Guo, *Phys. Rev. Lett.*, 2006, **96**, 166804.
124 R. Meservey and P. M. Tedrow, *Phys. Rep.*, 1994, **238**, 173–243.
125 S. Yuasa and D. D. Djayaprawira, *J. Phys. D: Appl. Phys.*, 2007, **40**, R337–R354.
126 J. M. De Teresa, A. Barthélémy, A. Fert, J. P. Contour, F. Montaigne and P. Seneor, *Science*, 1999, **286**, 507–509.
127 S. Parkin, J. Xin, C. Kaiser, A. Panchula, K. Roche and M. Samant, *Proc. IEEE*, 2003, **91**, 661–680.
128 R. Keizer, S. Goennenwein, T. Klapwijk, G. Miao, G. Xiao and A. Gupta, *Nature*, 2006, **439**, 825–827.
129 D. Zhang, Z. Liu, S. Han, C. Li, B. Lei, M. P. Stewart, M. James and C. Zhou, *Nano Lett.*, 2004, **4**, 2151–2155.
130 J. H. Park, E. Vescovo, H. J. Kim, C. Kwon, R. Ramesh and T. Venkatesan, *Phys. Rev. Lett.*, 1998, **81**, 1953–1956.
131 R. A. De Groot, F. M. Mueller, P. G. Engen and K. H. J. Buschow, *Phys. Rev. Lett.*, 1983, **50**, 2024–2027.
132 J. H. Park, E. Vescovo, H. J. Kim, C. Kwon, R. Ramesh and T. Venkatesan, *Nature*, 1998, **392**, 794–796.
133 M. Bowen, M. Bibes, A. Barthélémy, J. P. Contour, A. Anane, Y. Lemaitre and A. Fert, *Appl. Phys. Lett.*, 2002, **82**, 233–235.
134 J. Wang, H. Meng and J.-P. Wang, *J. Appl. Phys.*, 2005, **97**, 10D509.
135 A. Ney, C. Pampuch, R. Koch and K. H. Ploog, *Nature*, 2003, **425**, 485–487.
136 K. Tsunekawa, D. D. Djayaprawira, M. Nagai, H. Maehara, S. Yamagata, N. Watanabe, S. Yuasa, Y. Suzuki and K. Ando, *Appl. Phys. Lett.*, 2005, **87**, 072503.
137 S. Parkin, K. Roche, M. Samant, P. Rice, R. Beyers, R. Scheuerlein, E. OSullivan, S. Brown, J. Bucchigano and D. Abraham, *J. Appl. Phys.*, 1999, **85**, 5828–5833.
138 A. P. Ramirez, *J. Phys.: Condens. Matter*, 1997, **9**, 8171–8199.
139 M. Uehara, S. Mori, C. H. Chen and S. W. Cheong, *Nature*, 1999, **399**, 560–563.
140 J. De Teresa, M. Ibarra, P. Algarabel, C. Ritter, C. Marquina, J. Blasco, J. Garcia, A. del Moral and Z. Arnold, *Nature*, 1997, **386**, 256–259.
141 E. L. Nagaev, *Phys. Rep.*, 2001, **346**, 387–531.
142 R. von Helmolt, J. Wecker, B. Holzapfel, L. Schultz and K. Samwer, *Phys. Rev. Lett.*, 1993, **71**, 2331–2333.
143 S. Jin, T. H. Tiefel, M. McCormack, R. A. Fastnacht, R. Ramesh and L. H. Chen, *Science*, 1994, **264**, 413–415.
144 K. Ahn, X. Wu, K. Liu and C. Chien, *Phys. Rev. B: Condens. Matter Mater. Phys.*, 1996, **54**, 15299–15302.
145 J. Fontcuberta, B. Martinez, A. Seffar, S. Pinol, J. Garcia-Munoz and X. Obradors, *Phys. Rev. Lett.*, 1996, **76**, 1122–1125.
146 C. Şen, G. Alvarez and E. Dagotto, *Phys. Rev. Lett.*, 2010, **105**, 097203.
147 J. Tao, D. Niebieskikwiat, M. Varela, W. Luo, M. Schofield, Y. Zhu, M. B. Salamon, J.-M. Zuo, S. T. Pantelides and S. J. Pennycook, *Phys. Rev. Lett.*, 2009, **103**, 097202.
148 H. Röder, J. Zang and A. R. Bishop, *Phys. Rev. Lett.*, 1996, **76**, 1356–1359.
149 A. J. Millis, B. I. Shraiman and R. Mueller, *Phys. Rev. Lett.*, 1996, **77**, 175–178.
150 E. J. Wildman, J. M. S. Skakle, N. Emery and A. C. McLaughlin, *J. Am. Chem. Soc.*, 2012, **134**, 8766–8769.
151 C. M. Varma, *Phys. Rev. B: Condens. Matter Mater. Phys.*, 1996, **54**, 7328–7333.
152 K. Jin, S. Zhao, C. Chen, J. Wang and B. Luo, *Appl. Phys. Lett.*, 2008, **92**, 112512.
153 R. N. Mahato, K. Sethupathi and V. Sankaranarayanan, *J. Appl. Phys.*, 2010, **107**, 09D714.
154 X. Zhou, B. A. Piot, M. Bonin, L. W. Engel, S. Das Sarma, G. Gervais, L. N. Pfeiffer and K. W. West, *Phys. Rev. Lett.*, 2010, **104**, 216801.
155 J. Laverdière, S. Jandl and P. Fournier, *Phys. Rev. B: Condens. Matter Mater. Phys.*, 2011, **84**, 104434.
156 H. Sakurai, T. Kolodiazhnyi, Y. Michiue, E. Takayama-Muromachi, Y. Tanabe and H. Kikuchi, *Angew. Chem., Int. Ed.*, 2012, **51**, 6653–6656.
157 A. Ramirez, R. Cava and J. Krajewski, *Nature*, 1997, **386**, 156–159.
158 V. Dediu, L. E. Hueso, I. Bergenti, A. Riminucci, F. Borgatti, P. Graziosi, C. Newby, F. Casoli, M. P. De Jong, C. Taliani and Y. Zhan, *Phys. Rev. B: Condens. Matter Mater. Phys.*, 2008, **78**, 115203.
159 B. A. Jones, M. J. Ahrens, M.-H. Yoon, A. Facchetti, T. J. Marks and M. R. Wasielewski, *Angew. Chem.*, 2004, **116**, 6523–6526.
160 P. Gao, D. Beckmann, H. N. Tsao, X. Feng, V. Enkelmann, M. Baumgarten, W. Pisula and K. Müllen, *Adv. Mater.*, 2009, **21**, 213–216.
161 M. Zhang, H. N. Tsao, W. Pisula, C. Yang, A. K. Mishra and K. Müllen, *J. Am. Chem. Soc.*, 2007, **129**, 3472–3473.
162 V. Y. Aristov, O. V. Molodtsova, Y. A. Ossipyan, B. P. Doyle, S. Nannarone and M. Knupfer, *Org. Electron.*, 2009, **10**, 8–11.

Published on 30 April 2013. Downloaded by University of Tennessee at Knoxville on 10/06/2016 20:55:54.

163 H. K. Seung, H. Pan, C. P. Grigoropoulos, C. K. Luscombe, J. M. J. Fréchet and D. Poulikakos, *Nanotechnology*, 2007, **18**, 345202.
164 V. P. Verma, S. Das, I. Lahiri and W. Choi, *Appl. Phys. Lett.*, 2010, **96**, 203108.
165 G. Giri, E. Verploegen, S. C. B. Mannsfeld, S. Atahan-Evrenk, D. H. Kim, S. Y. Lee, H. A. Becerril, A. Aspuru-Guzik, M. F. Toney and Z. Bao, *Nature*, 2011, **480**, 504–508.
166 M. Irimia-Vladu, N. S. Sariciftci and S. Bauer, *J. Mater. Chem.*, 2011, **21**, 1350–1361.
167 Y. Zhang, J. Ren, G. Hu and S. Xie, *Org. Electron.*, 2008, **9**, 687–691.
168 I. D. W. Samuel and G. A. Turnbull, *Chem. Rev.*, 2007, **107**, 1272–1295.
169 Z. G. Yu, M. A. Berding and S. Krishnamurthy, *Phys. Rev. B: Condens. Matter Mater. Phys.*, 2005, **71**, 060408.
170 S. J. Xie, K. H. Ahn, D. L. Smith, A. R. Bishop and A. Saxena, *Phys. Rev. B: Condens. Matter Mater. Phys.*, 2003, **67**, 125202.
171 Y. Zhang, Y.-W. Tan, H. L. Stormer and P. Kim, *Nature*, 2005, **438**, 201–204.
172 P. A. Bobbert, W. Wagemans, F. W. A. van Oost, B. Koopmans and M. Wohlgenannt, *Phys. Rev. Lett.*, 2009, **102**, 156604.
173 D. S. McClure, *J. Chem. Phys.*, 1952, **20**, 682.
174 V. A. Dediu, L. E. Hueso, I. Bergenti and C. Taliani, *Nat. Mater.*, 2009, **8**, 707–716.
175 G. Szulczewski, S. Sanvito and M. Coey, *Nat. Mater.*, 2009, **8**, 693–695.
176 I. Bergenti, V. Dediu, M. Prezioso and A. Riminucci, *Philos. Trans. R. Soc., A*, 2011, **369**, 3054–3068.
177 C. H. Marrows and B. J. Hickey, *Philos. Trans. R. Soc., A*, 2011, **369**, 3027–3036.
178 P. P. Ruden and D. L. Smith, *J. Appl. Phys.*, 2004, **95**, 4898–4904.
179 Y. Q. Zhan, M. P. de Jong, F. H. Li, V. Dediu, M. Fahlman and W. R. Salaneck, *Phys. Rev. B: Condens. Matter Mater. Phys.*, 2008, **78**, 045208.
180 S. T. Lee, X. Y. Hou, G. M. Mason and C. W. Tang, *Appl. Phys. Lett.*, 1998, **72**, 1593–1595.
181 Y. Liu, S. M. Watson, T. Lee, J. M. Gorham, H. E. Katz, J. A. Borchers, H. D. Fairbrother and D. H. Reich, *Phys. Rev. B*, 2009, **79**, 075312.
182 J. J. H. M. Schoonus, P. G. E. Lumens, W. Wagemans, J. T. Kohlhepp, P. A. Bobbert, H. J. M. Swagten and B. Koopmans, *Phys. Rev. Lett.*, 2009, **103**, 146601.
183 G. Szulczewski, H. Tokuc, K. Oguz and J. M. D. Coey, *Appl. Phys. Lett.*, 2009, **95**, 202506.
184 B. Kanchibotla, S. Pramanik, S. Bandyopadhyay and M. Cahay, *Phys. Rev. B: Condens. Matter Mater. Phys.*, 2008, **78**, 193306.
185 J. W. Yoo, H. W. Jang, V. N. Prigodin, C. Kao, C. B. Eom and A. J. Epstein, *Phys. Rev. B: Condens. Matter Mater. Phys.*, 2009, **80**, 205207.
186 J. C. Clark, G. G. Ihas, A. J. Rafanello, M. W. Meisel, M. Reghu, C. O. Yoon, Y. Cao and A. J. Heeger, *Synth. Met.*, 1995, **69**, 215–216.
187 Y. Long, Z. Chen, J. Shen, Z. Zhang, L. Zhang, K. Huang, M. Wan, A. Jin, C. Gu and J. L. Duvail, *Nanotechnology*, 2006, **17**, 5903–5911.
188 W. Wagemans, A. J. Schellekens, M. Kemper, F. L. Bloom, P. A. Bobbert and B. Koopmans, *Phys. Rev. Lett.*, 2011, **106**, 196802.
189 J. D. Bergeson, V. N. Prigodin, D. M. Lincoln and A. J. Epstein, *Phys. Rev. Lett.*, 2008, **100**, 067201.
190 F. L. Bloom, W. Wagemans and B. Koopmans, *J. Appl. Phys.*, 2008, **103**, 07F320.
191 Y. Z. Long, Z. H. Yin and Z. J. Chen, *J. Phys. Chem. C*, 2008, **112**, 11507–11512.
192 W. Wagemans, P. Janssen, E. H. M. van der Heijden, M. Kemerink and B. Koopmans, *Appl. Phys. Lett.*, 2010, **97**, 123301.
193 Y. Long, Z. Chen, X. Zhang, J. Zhang and Z. Liu, *Appl. Phys. Lett.*, 2004, **85**, 1796–1798.
194 W. Xu, G. J. Szulczewski, P. LeClair, I. Navarrete, R. Schad, G. Miao, H. Guo and A. Gupta, *Appl. Phys. Lett.*, 2007, **90**, 072506.
195 C. Barraud, P. Seneor, R. Mattana, S. Fusil, K. Bouzehouane, C. Deranlot, P. Graziosi, L. Hueso, I. Bergenti, V. Dediu, F. Petroff and A. Fert, *Nat. Phys.*, 2010, **6**, 615–620.
196 J.-W. Yoo, C.-Y. Chen, H. W. Jang, C. W. Bark, V. N. Prigodin, C. B. Eom and A. J. Epstein, *Nat. Mater.*, 2010, **9**, 638–642.
197 T. Francis, Ö. Mermer, G. Veeraraghavan and M. Wohlgenannt, *New J. Phys.*, 2004, **6**, 185.
198 T. K. Mitra, A. Chatterjee and S. Mukhopadhyay, *Phys. Rep.*, 1987, **153**, 91–207.
199 D. Bertho and C. Jouanin, *Phys. Rev. B: Condens. Matter Mater. Phys.*, 1987, **35**, 626–633.
200 Z. Shuai, D. Beljonne, R. J. Silbey and J. L. Brédas, *Phys. Rev. Lett.*, 2000, **84**, 131–134.
201 M. N. Bussac and L. Zuppiroli, *Phys. Rev. B: Condens. Matter Mater. Phys.*, 1993, **47**, 5493–5496.
202 I. G. Hill, A. Kahn, Z. G. Soos and J. R. A. Pascal, *Chem. Phys. Lett.*, 2000, **327**, 181–188.
203 R. Waser, *Nanoelectronics and Information Technology*, John Wiley & Sons, 2005.
204 C. Carbogno, J. r. Behler, A. Groß and K. Reuter, *Phys. Rev. Lett.*, 2008, **101**, 096104.
205 M. A. Baldo, D. F. O'Brien, M. E. Thompson and S. R. Forrest, *Phys. Rev. B: Condens. Matter Mater. Phys.*, 1999, **60**, 14422–14428.
206 V. Ern and R. E. Merrifield, *Phys. Rev. Lett.*, 1968, **21**, 609–611.
207 P. Desai, P. Shakya, T. Kreouzis and W. P. Gillin, *J. Appl. Phys.*, 2007, **102**, 073710.
208 P. Desai, P. Shakya, T. Kreouzis, W. P. Gillin, N. A. Morley and M. R. J. Gibbs, *Phys. Rev. B: Condens. Matter Mater. Phys.*, 2007, **75**, 094423.

 This journal is © The Royal Society of Chemistry 2013

Published on 30 April 2013. Downloaded by University of Tennessee at Knoxville on 10/06/2016 20:55:54.

209 S. Besner, A. Vallee, G. Bouchard and J. Prud'homme, *Macromolecules*, 1992, **25**, 6480–6488.
210 C. Jacoboni and L. Reggiani, *Rev. Mod. Phys.*, 1983, **55**, 645.
211 C. K. Chiang, C. R. Fincher, Jr., Y. W. Park, A. J. Heeger, H. Shirakawa, E. J. Louis, S. C. Gau and A. G. MacDiarmid, *Phys. Rev. Lett.*, 1977, **39**, 1098–1101.
212 Y. Cui, X. Duan, J. Hu and C. M. Lieber, *J. Phys. Chem. B*, 2000, **104**, 5213–5216.
213 P. G. Collins and P. Avouris, *Sci. Am.*, 2000, **283**, 62–69.
214 A. Cresti, N. Nemec, B. Biel, G. Niebler, F. Triozon, G. Cuniberti and S. Roche, *Nano Res.*, 2008, **1**, 361–394.
215 K. S. Novoselov, A. K. Geim, S. V. Morozov, D. Jiang, Y. Zhang, S. V. Dubonos, I. V. Grigorieva and A. A. Firsov, *Science*, 2004, **306**, 666–669.
216 A. K. Geim and K. S. Novoselov, *Science*, 2007, **6**, 183–191.
217 A. H. C. Neto, F. Guinea, N. M. R. Peres, K. S. Novoselov and A. K. Geim, *Rev. Mod. Phys.*, 2009, **81**, 109–162.
218 F. Sols, F. Guinea and A. H. C. Neto, *Phys. Rev. Lett.*, 2007, **99**, 166803.
219 B. Huang, Q. Yan, G. Zhou, J. Wu, B. L. Gu, W. Duan and F. Liu, *Appl. Phys. Lett.*, 2007, **91**, 253122.
220 D. Gunlycke, J. Li, J. W. Mintmire and C. T. White, *Appl. Phys. Lett.*, 2007, **91**, 112108.
221 B. Biel, X. Blase, F. o. Triozon and S. Roche, *Phys. Rev. Lett.*, 2009, **102**, 096803.
222 Q. Yan, B. Huang, J. Yu, F. Zheng, J. Zang, J. Wu, B.-L. Gu, F. Liu and W. Duan, *Nano Lett.*, 2007, **7**, 1469–1473.
223 T. B. Martins, R. H. Miwa, A. J. R. da Silva and A. Fazzio, *Phys. Rev. Lett.*, 2007, **98**, 196803.
224 F. Cervantes-Sodi, G. Csányi, S. Piscanec and A. C. Ferrari, *Phys. Rev. B: Condens. Matter Mater. Phys.*, 2008, **77**, 165427.
225 P. Avouris, *Acc. Chem. Res.*, 2002, **35**, 1026–1034.
226 M. S. Dresselhaus, A. Jorio, M. Hofmann, G. Dresselhaus and R. Saito, *Nano Lett.*, 2010, **10**, 751–758.
227 C. Joachim, J. K. Gimzewski and A. Aviram, *Nature*, 2000, **408**, 541–548.
228 J. Charlier, X. Blase and S. Roche, *Rev. Mod. Phys.*, 2007, **79**, 677–732.
229 T. W. Odom, J.-L. Huang, P. Kim and C. M. Lieber, *Nature*, 1998, **391**, 62–64.
230 G. T. Kim, E. S. Choi, D. C. Kim, D. S. Suh, Y. W. Park, K. Liu, G. Duesberg and S. Roth, *Phys. Rev. B: Condens. Matter Mater. Phys.*, 1998, **58**, 16064–16069.
231 Y. Oshima, T. Takenobu, K. Yanagi, Y. Miyata, H. Kataura, K. Hata, Y. Iwasa and H. Nojiri, *Phys. Rev. Lett.*, 2010, **104**, 016803.
232 X. Wang, J. Lu and B. Xing, *Environ. Sci. Technol.*, 2008, **42**, 3207–3212.
233 H. Khani, M. K. Rofouei, P. Arab, V. K. Gupta and Z. Vafaei, *J. Hazard. Mater.*, 2010, **183**, 402–409.
234 S. Frank, P. Poncharal, Z. L. Wang and W. A. de Heer, *Science*, 1998, **280**, 1744–1746.
235 T. Rueckes, K. Kim, E. Joselevich, G. Y. Tseng, C. Cheung and C. M. Lieber, *Science*, 2000, **289**, 94–97.
236 A. A. Farajian, K. Esfarjani and Y. Kawazoe, *Phys. Rev. Lett.*, 1999, **82**, 5084–5087.
237 G. Nan, X. Yang, L. Wang, Z. Shuai and Y. Zhao, *Phys. Rev. B: Condens. Matter Mater. Phys.*, 2009, **79**, 115203.
238 N. A. Minder, S. Ono, Z. Chen, A. Facchetti and A. F. Morpurgo, *Adv. Mater.*, 2012, **24**, 503–508.
239 O. Ostroverkhova, D. G. Cooke, S. Shcherbyna, R. F. Egerton, F. A. Hegmann, R. R. Tykwinski and J. E. Anthony, *Phys. Rev. B: Condens. Matter Mater. Phys.*, 2005, **71**, 035204.
240 K. Hannewald and P. A. Bobbert, *Phys. Rev. B: Condens. Matter Mater. Phys.*, 2004, **69**, 075212.
241 J. C. Blakesley, H. S. Clubb and N. C. Greenham, *Phys. Rev. B: Condens. Matter Mater. Phys.*, 2010, **81**, 045210.
242 S. V. Novikov and G. G. Malliaras, *Phys. Rev. B: Condens. Matter Mater. Phys.*, 2006, **73**, 033308.
243 J. C. Blakesley and D. Neher, *Phys. Rev. B: Condens. Matter Mater. Phys.*, 2011, **84**, 075210.
244 L. B. Schein and A. Tyutnev, *J. Phys. Chem. C*, 2008, **112**, 7295–7308.
245 H. Bässler, *Phys. Status Solidi B*, 1993, **175**, 15–56.
246 D. Dunlap, P. Parris and V. Kenkre, *Phys. Rev. Lett.*, 1996, **77**, 542–545.
247 I. Hulea, H. Brom, A. Houtepen, D. Vanmaekelbergh, J. Kelly and E. Meulenkamp, *Phys. Rev. Lett.*, 2004, **93**, 166601.
248 O. Tal, Y. Rosenwaks, Y. Preezant, N. Tessler, C. Chan and A. Kahn, *Phys. Rev. Lett.*, 2005, **95**, 256405.
249 A. Kaiser, *Rep. Prog. Phys.*, 2000, **64**, 1–49.
250 J. Zhu, S. Wei, L. Zhang, Y. Mao, J. Ryu, N. Haldolaarachchige, D. P. Young and Z. Guo, *J. Mater. Chem.*, 2011, **21**, 3952–3959.
251 L. Zhang and Z.-J. Tang, *Phys. Rev. B: Condens. Matter Mater. Phys.*, 2004, **70**, 174306.
252 M. Oestreich, J. Hubner, D. Hagele, P. Klar, W. Heimbrodt, W. Ruhle, D. Ashenford and B. Lunn, *Appl. Phys. Lett.*, 1999, **74**, 1251–1253.
253 A. Fert, *Rev. Mod. Phys.*, 2008, **80**, 1517–1530.
254 A. Fert, *Angew. Chem., Int. Ed.*, 2008, **47**, 5956–5967.
255 E. I. Rashba, *Phys. Rev. B: Condens. Matter Mater. Phys.*, 2000, **62**, R16267–R16270.
256 A. Fert and H. Jaffrès, *Phys. Rev. B: Condens. Matter Mater. Phys.*, 2001, **64**, 184420.
257 S. Zhang, *Phys. Rev. Lett.*, 2000, **85**, 393–396.
258 M. König, S. Wiedmann, C. Brüne, A. Roth, H. Buhmann, L. W. Molenkamp, X.-L. Qi and S.-C. Zhang, *Science*, 2007, **318**, 766–770.
259 H. R. Shea, R. Martel and P. Avouris, *Phys. Rev. Lett.*, 2000, **84**, 4441–4444.
260 J. H. Shim, K. V. Raman, Y. J. Park, T. S. Santos, G. X. Miao, B. Satpati and J. S. Moodera, *Phys. Rev. Lett.*, 2008, **100**, 226603.
261 F. Li, P. Graziosi, Q. Tang, Y. Zhan, X. Liu, V. Dediu and M. Fahlman, *Phys. Rev. B: Condens. Matter Mater. Phys.*, 2010, **81**, 205415.

Published on 30 April 2013. Downloaded by University of Tennessee at Knoxville on 10/06/2016 20:55:54.

262 C. Felser, G. H. Fecher and B. Balke, *Angew. Chem., Int. Ed.*, 2007, **46**, 668–699.
263 W. Pötz, J. Fabian and U. Hohenester, *Modern Aspects of Spin Physics*, Springer, 2006.
264 S. J. Pearton, C. R. Abernathy, D. P. Norton, A. F. Hebard, Y. D. Park, L. A. Boatner and J. D. Budai, *Mater. Sci. Eng., R*, 2003, **40**, 137–168.
265 D. D. Awschalom and M. E. Flatté, *Nat. Phys.*, 2007, **3**, 153–159.
266 V. F. Motsnyi, J. De Boeck, J. Das, W. Van Roy, G. Borghs, E. Goovaerts and V. I. Safarov, *Appl. Phys. Lett.*, 2002, **81**, 265–267.
267 M. Johnson and R. H. Silsbee, *Phys. Rev. B: Condens. Matter Mater. Phys.*, 1988, **37**, 5326–5335.
268 V. Osipov and A. Bratkovsky, *Appl. Phys. Lett.*, 2004, **84**, 2118–2120.
269 K. M. McCreary, A. G. Swartz, W. Han, J. Fabian and R. K. Kawakami, *Phys. Rev. Lett.*, 2012, **109**, 186604.
270 S. D. Sarma, *Am. Sci.*, 2001, 516–523.
271 N. F. Mott, *Proc. R. Soc. London, Ser. A*, 1936, **153**, 699–717.
272 I. Mertig, P. Zahn, M. Richter, H. Eschrig, R. Zeller and P. H. Dederichs, *J. Magn. Magn. Mater.*, 1995, **151**, 363–368.
273 P. Hohenberg and W. Kohn, *Phys. Rev.*, 1964, **136**, B864–B871.
274 W. Kohn and L. J. Sham, *Phys. Rev.*, 1965, **140**, A1133–A1138.
275 P. Zahn, I. Mertig, M. Richter and H. Eschrig, *Phys. Rev. Lett.*, 1995, **75**, 2996–2999.
276 S. Sanvito and N. A. Hill, *Phys. Rev. Lett.*, 2001, **87**, 267202.
277 M. L. Tiago, J. E. Northrup and S. G. Louie, *Phys. Rev. B: Condens. Matter Mater. Phys.*, 2003, **67**, 115212.
278 P. Sharma, A. Gupta, K. Rao, F. J. Owens, R. Sharma, R. Ahuja, J. M. O. Guillen, B. Johansson and G. Gehring, *Nat. Mater.*, 2003, **2**, 673–677.
279 B. Wang, J. Wang and H. Guo, *Phys. Rev. B: Condens. Matter Mater. Phys.*, 2009, **79**, 165417.
280 J. A. Fürst, M. Brandbyge, A.-P. Jauho and K. Stokbro, *Phys. Rev. B: Condens. Matter Mater. Phys.*, 2008, **78**, 195405.
281 L. E. Hueso, J. M. Pruneda, V. Ferrari, G. Burnell, J. P. Valdes-Herrera, B. D. Simons, P. B. Littlewood, E. Artacho, A. Fert and N. D. Mathur, *Nature*, 2007, **445**, 410–413.
282 K. Tarafder, B. Sanyal and P. M. Oppeneer, *Phys. Rev. B: Condens. Matter Mater. Phys.*, 2010, **82**, 060413.
283 C. Heiliger and M. D. Stiles, *Phys. Rev. Lett.*, 2008, **100**, 186805.
284 S. Tehrani, J. M. Slaughter, M. DeHerrera, B. N. Engel, N. D. Rizzo, J. Salter, M. Durlam, R. W. Dave, J. Janesky, B. Butcher, K. Smith and G. Grynkewich, *Proc. IEEE*, 2003, **91**, 703–714.
285 J. P. Velev, C.-G. Duan, J. D. Burton, A. Smogunov, M. K. Niranjan, E. Tosatti, S. S. Jaswal and E. Y. Tsymbal, *Nano Lett.*, 2008, **9**, 427–432.
286 S. Pramanik, S. Bandyopadhyay, K. Garre and M. Cahay, *Phys. Rev. B: Condens. Matter Mater. Phys.*, 2006, **74**, 235329.
287 J. S. Jiang, J. E. Pearson and S. D. Bader, *Phys. Rev. B: Condens. Matter Mater. Phys.*, 2008, **77**, 035303.
288 F. J. Wang, C. G. Yang, Z. V. Vardeny and X. G. Li, *Phys. Rev. B: Condens. Matter Mater. Phys.*, 2007, **75**, 245324.
289 G. Schmidt, D. Ferrand, L. W. Molenkamp, A. T. Filip and B. J. van Wees, *Phys. Rev. B: Condens. Matter Mater. Phys.*, 2000, **62**, R4790–R4793.
290 J. C. Charlier and J. P. Michenaud, *Phys. Rev. Lett.*, 1993, **70**, 1858–1861.
291 R. Saito, G. Dresselhaus and M. S. Dresselhaus, *J. Appl. Phys.*, 1993, **70**, 494–500.
292 H. Vinzelberg, J. Schumann, D. Elefant, R. B. Gangineni, J. Thomas and B. Büchner, *J. Appl. Phys.*, 2008, **103**, 093720.
293 Y. Q. Zhan, I. Bergenti, L. E. Hueso, V. Dediu, M. P. de Jong and Z. S. Li, *Phys. Rev. B: Condens. Matter Mater. Phys.*, 2007, **76**, 045406.
294 D. Sun, L. Yin, C. Sun, H. Guo, Z. Gai, X. G. Zhang, T. Z. Ward, Z. Cheng and J. Shen, *Phys. Rev. Lett.*, 2010, **104**, 236602.
295 S. Pramanik, C. G. Stefanita, S. Patibandla, S. Bandyopadhyay, K. Garre, N. Harth and M. Cahay, *Nat. Nanotechnol.*, 2007, **2**, 216–219.
296 R. J. Elliott, *Phys. Rev.*, 1954, **96**, 266–279.
297 M. W. Wu, J. H. Jiang and M. Q. Weng, *Phys. Rep.*, 2010, **493**, 61–236.
298 P. H. Song and K. W. Kim, *Phys. Rev. B: Condens. Matter Mater. Phys.*, 2002, **66**, 035207.
299 G. Salis, S. F. Alvarado, M. Tschudy, T. Brunschwiler and R. Allenspach, *Phys. Rev. B: Condens. Matter Mater. Phys.*, 2004, **70**, 085203.
300 V. Podzorov, E. Menard, A. Borissov, V. Kiryukhin, J. A. Rogers and M. E. Gershenson, *Phys. Rev. Lett.*, 2004, **93**, 086602.
301 K. V. Raman, S. M. Watson, J. H. Shim, J. A. Borchers, J. Chang and J. S. Moodera, *Phys. Rev. B: Condens. Matter Mater. Phys.*, 2009, **80**, 195212.
302 R. Lin, F. Wang, J. Rybicki, M. Wohlgenannt and K. A. Hutchinson, *Phys. Rev. B: Condens. Matter Mater. Phys.*, 2010, **81**, 195214.
303 H. Kusai, S. Miwa, M. Mizuguchi, T. Shinjo, Y. Suzuki and M. Shiraishi, *Chem. Phys. Lett.*, 2007, **448**, 106–110.
304 D. Hatanaka, S. Tanabe, H. Kusai, R. Nouchi, T. Nozaki, T. Shinjo, Y. Suzuki, H. Wang, K. Takanashi and M. Shiraishi, *Phys. Rev. B: Condens. Matter Mater. Phys.*, 2009, **79**, 235402.
305 S. Takahashi and S. Maekawa, *Phys. Rev. Lett.*, 1998, **80**, 1758–1761.
306 T. Kimura, J. Hamrle and Y. Otani, *Phys. Rev. B: Condens. Matter Mater. Phys.*, 2005, **72**, 014461.
307 E. L. Murphy and R. H. Good, Jr., *Phys. Rev.*, 1956, **102**, 1464–1473.
308 J. W. Yoo, H. W. Jang, V. N. Prigodin, C. Kao, C. B. Eom and A. J. Epstein, *Synth. Met.*, 2010, **160**, 216–222.
309 J. M. Garguilo, F. A. M. Koeck, R. J. Nemanich, X. C. Xiao, J. A. Carlisle and O. Auciello, *Phys. Rev. B: Condens. Matter Mater. Phys.*, 2005, **72**, 165404.

 This journal is © The Royal Society of Chemistry 2013

Published on 30 April 2013. Downloaded by University of Tennessee at Knoxville on 10/06/2016 20:55:54.

310 X. Lou, C. Adelmann, S. A. Crooker, E. S. Garlid, J. Zhang, K. S. M. Reddy, S. D. Flexner, C. J. Palmstrom and P. A. Crowell, *Nat. Phys.*, 2007, **3**, 197–202.
311 A. Vilan, A. Shanzer and D. Cahen, *Nature*, 2000, **404**, 166–168.
312 P. Pipinys and A. Kiveris, *J. Phys.: Condens. Matter*, 2005, **17**, 4147–4155.
313 C. Xu, G. Luo, Q. Liu, J. Zheng, Z. Zhang, S. Nagase, Z. Gao and J. Lu, *Nanoscale*, 2012, **4**, 3111–3117.
314 A. Avsar, T. Yang, S. Bae, J. Balakrishnan, F. Volmer, M. Jaiswal, Z. Yi, S. R. Ali, G. Güntherodt, B. H. Hong, B. Beschoten and B. Öyilmaz, *Nano Lett.*, 2011, **11**, 2363–2368.
315 T. G. Pedersen, C. Flindt, J. Pedersen, N. A. Mortensen, A.-P. Jauho and K. Pedersen, *Phys. Rev. Lett.*, 2008, **100**, 136804.
316 K. S. Novoselov, A. K. Geim, S. V. Morozov, D. Jiang, M. I. Katsnelson, I. V. Grigorieva, S. V. Dubonos and A. A. Firsov, *Nature*, 2005, **438**, 197–200.
317 S. Cho, Y.-F. Chen and M. S. Fuhrer, *Appl. Phys. Lett.*, 2007, **91**, 123105.
318 O. V. Yazyev and M. I. Katsnelson, *Phys. Rev. Lett.*, 2008, **100**, 047209.
319 D. Pesin and A. H. MacDonald, *Nat. Mater.*, 2012, **11**, 409–416.
320 Y.-W. Son, M. L. Cohen and S. G. Louie, *Nature*, 2006, **444**, 347–349.
321 W. H. Wang, K. Pi, Y. Li, Y. F. Chiang, P. Wei, J. Shi and R. K. Kawakami, *Phys. Rev. B: Condens. Matter Mater. Phys.*, 2008, **77**, 020402.
322 M. Shiraishi, M. Ohishi, R. Nouchi, N. Mitoma, T. Nozaki, T. Shinjo and Y. Suzuki, *Adv. Funct. Mater.*, 2009, **19**, 3711–3716.
323 N. Tombros, S. Tanabe, A. Veligura, C. Jozsa, M. Popinciuc, H. T. Jonkman and B. J. van Wees, *Phys. Rev. Lett.*, 2008, **101**, 046601.
324 W. Han, W. H. Wang, K. Pi, K. M. McCreary, W. Bao, Y. Li, F. Miao, C. N. Lau and R. K. Kawakami, *Phys. Rev. Lett.*, 2009, **102**, 137205.
325 K. Pi, W. Han, K. M. McCreary, A. G. Swartz, Y. Li and R. K. Kawakami, *Phys. Rev. Lett.*, 2010, **104**, 187201.
326 A. H. C. Neto and F. Guinea, *Phys. Rev. Lett.*, 2009, **103**, 026804.
327 C. Ertler, S. Konschuh, M. Gmitra and J. Fabian, *Phys. Rev. B: Condens. Matter Mater. Phys.*, 2009, **80**, 041405.
328 S. Krompiewski, *Nanotechnology*, 2012, **23**, 135203.
329 Y. T. Zhang, H. Jiang, Q. f. Sun and X. C. Xie, *Phys. Rev. B: Condens. Matter Mater. Phys.*, 2010, **81**, 165404.
330 J. Hubbard, *Proc. R. Soc. London, Ser. A*, 1963, **276**, 238–257.
331 Y. Meir and N. S. Wingreen, *Phys. Rev. Lett.*, 1992, **68**, 2512–2515.
332 J. K. Jain and S. A. Kivelson, *Phys. Rev. B: Condens. Matter Mater. Phys.*, 1988, **37**, 4276–4279.
333 W. W. Lui and M. Fukuma, *J. Appl. Phys.*, 1986, **60**, 1555–1559.
334 L. Li, R. Qin, H. Li, L. Yu, Q. Liu, G. Luo, Z. Gao and J. Lu, *ACS Nano*, 2011, **5**, 2601–2610.
335 J. Bai, R. Cheng, F. Xiu, L. Liao, M. Wang, A. Shailos, K. L. Wang, Y. Huang and X. Duan, *Nat. Nanotechnol.*, 2010, **5**, 655–659.
336 N. M. R. Peres, A. H. C. Neto and F. Guinea, *Phys. Rev. B: Condens. Matter Mater. Phys.*, 2006, **73**, 195411.
337 N. M. R. Peres, A. H. C. Neto and F. Guinea, *Phys. Rev. B: Condens. Matter Mater. Phys.*, 2006, **73**, 241403.
338 C. Ritter, S. S. Makler and A. Latgé, *Phys. Rev. B: Condens. Matter Mater. Phys.*, 2008, **77**, 195443.
339 A. Candini, S. Klyatskaya, M. Ruben, W. Wernsdorfer and M. Affronte, *Nano Lett.*, 2011, **11**, 2634–2639.
340 A. L. Friedman, J. L. Tedesco, P. M. Campbell, J. C. Culbertson, E. Aifer, F. K. Perkins, R. L. Myers-Ward, J. K. Hite, C. R. Eddy, G. G. Jernigan and D. K. Gaskill, *Nano Lett.*, 2010, **10**, 3962–3965.
341 J. Hu and T. F. Rosenbaum, *Nat. Mater.*, 2008, **7**, 697–700.
342 J. Sinova, D. Culcer, Q. Niu, N. A. Sinitsyn, T. Jungwirth and A. H. MacDonald, *Phys. Rev. Lett.*, 2004, **92**, 126603.
343 J. K. Jain, *Phys. Rev. Lett.*, 1989, **63**, 199–202.
344 J. Zhu, S. Wei, N. Haldolaarachchige, J. He, D. P. Young and Z. Guo, *Nanoscale*, 2012, **4**, 152–156.
345 E. U. Stützel, M. Burghard, K. Kern, F. Traversi, F. Nichele and R. Sordan, *Small*, 2010, **6**, 2821.
346 J. Zhu, Z. Luo, S. Wu, N. Haldolaarachchige, D. P. Young, S. Wei and Z. Guo, *J. Mater. Chem.*, 2012, **22**, 835–844.
347 J. S. Burgess, B. R. Matis, J. T. Robinson, F. A. Bulat, F. K. Perkins, B. H. Houston and J. W. Baldwin, *Carbon*, 2012, **49**, 4420–4426.
348 B. R. Matis, J. S. Burgess, F. A. Bulat, A. L. Friedman, B. H. Houston and J. W. Baldwin, *ACS Nano*, 2012, **6**, 17–22.
349 J. Zhou, Q. Wang, Q. Sun, X. S. Chen, Y. Kawazoe and P. Jena, *Nano Lett.*, 2009, **9**, 3867–3870.
350 D. Soriano, F. Muñoz-Rojas, J. Fernández-Rossier and J. J. Palacios, *Phys. Rev. B: Condens. Matter Mater. Phys.*, 2010, **81**, 165409.
351 B. R. Matis, F. A. Bulat, A. L. Friedman, B. H. Houston and J. W. Baldwin, *Phys. Rev. B: Condens. Matter Mater. Phys.*, 2012, **85**, 195437.
352 L. Moriconi and D. Niemeyer, *Phys. Rev. B: Condens. Matter Mater. Phys.*, 2011, **84**, 193401.
353 K. Tsukagoshi, B. W. Alphenaar and H. Ago, *Nature*, 1999, **401**, 572–574.
354 L. Balents and R. Egger, *Phys. Rev. Lett.*, 2000, **85**, 3464–3467.
355 S. Sahoo, T. Kontos, J. Furer, C. Hoffmann, M. Graber, A. Cottet and C. Schonenberger, *Nat. Phys.*, 2005, **1**, 99–102.
356 B. Nagabhirava, T. Bansal, G. U. Sumanasekera, B. W. Alphenaar and L. Liu, *Appl. Phys. Lett.*, 2006, **88**, 023503.
357 J.-R. Kim, H. M. So, J.-J. Kim and J. Kim, *Phys. Rev. B: Condens. Matter Mater. Phys.*, 2002, **66**, 233401.

Published on 30 April 2013. Downloaded by University of Tennessee at Knoxville on 10/06/2016 20:55:54.

358 A. Jensen, J. R. Hauptmann, J. Nygård and P. E. Lindelof, *Phys. Rev. B: Condens. Matter Mater. Phys.*, 2005, **72**, 035419.
359 O. Hod, E. Rabani and R. Baer, *J. Chem. Phys.*, 2005, **123**, 051103.
360 S. Athanasopoulos, S. W. Bailey, J. Ferrer, V. M. G. Suárez, C. J. Lambert, A. R. Rocha and S. Sanvito, *J. Phys.: Condens. Matter*, 2007, **19**, 042201.
361 Y. Ohno, K. Narumi, K. Maehashi, K. Inoue and K. Matsumoto, *J. Phys.: Conf. Ser.*, 2006, **38**, 57–60.
362 P. M. Tedrow and R. Meservey, *Phys. Rev. B: Solid State*, 1973, **7**, 318–326.
363 J. Z. Cai, L. Lu, W. J. Kong, H. W. Zhu, C. Zhang, B. Q. Wei, D. H. Wu and F. Liu, *Phys. Rev. Lett.*, 2006, **97**, 026402.
364 P. A. Lee and T. V. Ramakrishnan, *Rev. Mod. Phys.*, 1985, **57**, 287–337.
365 M. Urdampilleta, S. Klyatskaya, J. P. Cleuziou, M. Ruben and W. Wernsdorfer, *Nat. Mater.*, 2011, **10**, 502–506.
366 J.-O. Lee, J.-R. Kim, J.-J. Kim, J. Kim, N. Kim, J. W. Park, K.-H. Yoo and K.-H. Park, *Phys. Rev. B: Condens. Matter Mater. Phys.*, 2000, **61**, R16362–R16365.
367 B. Zhao, I. Mönch, H. Vinzelberg, T. Mühl and C. M. Schneider, *Appl. Phys. Lett.*, 2002, **80**, 3144–3146.
368 S. Krompiewski, R. Gutiérrez and G. Cuniberti, *Phys. Rev. B: Condens. Matter Mater. Phys.*, 2004, **69**, 155423.
369 S. Majumdar, R. Laiho, P. Laukkanen, I. J. Väyrynen, H. S. Majumdar and R. Österbacka, *Appl. Phys. Lett.*, 2006, **89**, 122114.
370 A. N. Aleshin, S. R. Williams and A. J. Heeger, *Synth. Met.*, 1998, **94**, 173–177.
371 F. Yan, G. Xue and F. Wan, *J. Mater. Chem.*, 2002, **12**, 2606–2608.
372 L. V. Hau, S. E. Harris, Z. Dutton and C. H. Behroozi, *Nature*, 1999, **397**, 594–598.
373 C. O. Yoon, M. Reghu, D. Moses, A. J. Heeger and Y. Cao, *Synth. Met.*, 1994, **63**, 47–52.
374 R. R. Rakhimov, O. K. Amponsah, L. A. Waller, V. G. Shevchenko, A. Y. Karmilov, I. A. Alexandrov and A. I. Aleksandrov, *J. Appl. Phys.*, 2009, **105**, 07E302.
375 K. Gupta, P. C. Jana, A. K. Meikap and T. K. Nath, *J. Appl. Phys.*, 2010, **107**, 073704.
376 D. J. Singh and M. H. Du, *Phys. Rev. Lett.*, 2008, **100**, 237003.
377 P. Raychaudhuri, K. Sheshadri, P. Taneja, S. Bandyopadhyay, P. Ayyub, A. K. Nigam, R. Pinto, S. Chaudhary and S. B. Roy, *Phys. Rev. B: Condens. Matter Mater. Phys.*, 1999, **59**, 13919–13926.
378 D. Jiles, *Introduction to magnetism and magnetic materials*, Chapman & Hall, 1998, 2nd edn, p. 157.
379 X. Zhang, S. Wei, N. Haldolaarachchige, H. A. Colorado, Z. Luo, D. P. Young and Z. Guo, *J. Phys. Chem. C*, 2012, **116**, 15731–15740.
380 U. Sivan, O. Entin-Wohlman and Y. Imry, *Phys. Rev. Lett.*, 1988, **60**, 1566–1569.
381 S. Schmaus, A. Bagrets, Y. Nahas, T. K. Yamada, A. Bork, M. Bowen, E. Beaurepaire, F. Evers and W. Wulfhekel, *Nat. Nanotechnol.*, 2011, **6**, 185–189.
382 M. M. Matsushita, H. Kawakami, T. Sugawara and M. Ogata, *Phys. Rev. B: Condens. Matter Mater. Phys.*, 2008, 77, 195208.
383 H. Komatsu, M. M. Matsushita, S. Yamamura, Y. Sugawara, K. Suzuki and T. Sugawara, *J. Am. Chem. Soc.*, 2010, **132**, 4528–4529.
384 J. Nishijo, A. Miyazaki, T. Enoki, R. Watanabe, Y. Kuwatani and M. Iyoda, *Inorg. Chem.*, 2005, **44**, 2493–2506.
385 T. Shirahata, M. Kibune, M. Maesato, T. Kawashima, G. Saito and T. Imakubo, *J. Mater. Chem.*, 2006, **16**, 3381–3390.
386 F. Beuneu and P. Monod, *Phys. Rev. B: Solid State*, 1976, **13**, 3424–3430.
387 T. Ikegami, I. Kawayama, M. Tonouchi, S. Nakao, Y. Yamashita and H. Tada, *Appl. Phys. Lett.*, 2008, **92**, 153304.
388 P. A. Bobbert, T. D. Nguyen, W. Wagemans, F. W. A. van Oost, B. Koopmans and M. Wohlgenannt, *Synth. Met.*, 2010, **160**, 223–229.
389 Y. Sheng, T. D. Nguyen, G. Veeraraghavan, Ö. Mermer, M. Wohlgenannt, S. Qiu and U. Scherf, *Phys. Rev. B: Condens. Matter Mater. Phys.*, 2006, **74**, 045213.
390 L. Onsager, *Phys. Rev.*, 1938, **54**, 554–557.
391 V. N. Prigodin, J. D. Bergeson, D. M. Lincoln and A. J. Epstein, *Synth. Met.*, 2006, **156**, 757–761.
392 R. H. Parmenter and W. Ruppel, *J. Appl. Phys.*, 1959, **30**, 1548–1558.
393 W. Wagemans, F. L. Bloom, P. A. Bobbert, M. Wohlgenannt and B. Koopmans, *J. Appl. Phys.*, 2008, **103**, 07F303.
394 P. Novák and V. Chlan, *Phys. Rev. B: Condens. Matter Mater. Phys.*, 2010, **81**, 174412.
395 P. A. Bobbert, T. D. Nguyen, F. W. A. van Oost, B. Koopmans and M. Wohlgenannt, *Phys. Rev. Lett.*, 2007, **99**, 216801.
396 T.-I. Su, C.-R. Wang, S.-T. Lin and R. Rosenbaum, *Phys. Rev. B: Condens. Matter Mater. Phys.*, 2002, **66**, 054438.
397 F. B. Robert, *Paleomagnetism: Magnetic domains to Geologic Terranes*, 2004, Electronic edition, p. 148.
398 R. Rosenbaum, A. Milner, S. Hannahs, T. Murphy, E. Palm and B. Brandt, *Physica B*, 2001, **294–295**, 340–342.
399 X. Zhang, J. Zhu, N. Haldolaarachchige, J. Ryu, D. P. Young, S. Wei and Z. Guo, *Polymer*, 2012, **53**, 2109–2120.
400 V. N. Prigodin, J. W. Yoo, H. W. Jang, C. Kao, C. B. Eom and A. J. Epstein, *J. Phys.: Conf. Ser.*, 2011, **292**, 012001.
401 L. E. Hueso, I. Bergenti, A. Riminucci, Y. Q. Zhan and V. Dediu, *Adv. Mater.*, 2007, **19**, 2639–2642.
402 J. Camarero and E. Coronado, *J. Mater. Chem.*, 2009, **19**, 1678–1684.
403 M. Koleini, M. Paulsson and M. Brandbyge, *Phys. Rev. Lett.*, 2007, **98**, 197202.

 This journal is © The Royal Society of Chemistry 2013

Published on 30 April 2013. Downloaded by University of Tennessee at Knoxville on 10/06/2016 20:55:54.

404 L. Liao, J. Bai, R. Cheng, Y.-C. Lin, S. Jiang, Y. Huang and X. Duan, *Nano Lett.*, 2010, **10**, 1917–1921.
405 J. A. Fürst, T. G. Pedersen, M. Brandbyge and A.-P. Jauho, *Phys. Rev. B: Condens. Matter Mater. Phys.*, 2009, **80**, 115117.
406 M. Zeng, L. Shen, M. Zhou, C. Zhang and Y. Feng, *Phys. Rev. B: Condens. Matter Mater. Phys.*, 2011, **83**, 115427.
407 T. D. Nguyen, G. Hukic-Markosian, F. Wang, L. Wojcik, X.-G. Li, E. Ehrenfreund and Z. V. Vardeny, *Synth. Met.*, 2011, **161**, 598–603.
408 M. Wohlgenannt, Z. V. Vardeny, J. Shi, T. L. Francis, X. M. Jiang, O. Mermer, G. Veeraraghavan, D. Wu and Z. H. Xiong, *IEE Proceedings, Part G: Circuits, Devices and Systems*, 2005, **152**, 385–392.
409 J. Lehmann, A. Gaita-Arino, E. Coronado and D. Loss, *Nat. Nanotechnol.*, 2007, **2**, 312–317.
410 F. Wang and Z. V. Vardeny, *J. Mater. Chem.*, 2009, **19**, 1685–1690.
411 S. J. Hurst, E. K. Payne, L. Qin and C. A. Mirkin, *Angew. Chem., Int. Ed.*, 2006, **45**, 2672–2692.